APPLIED COMPUTATIONAL ELECTROMAGNETICS SOCIETY JOURNAL

March 2023
Vol. 38 No. 3
ISSN 1054-4887

The ACES Journal is abstracted in INSPEC, in Engineering Index, DTIC, Science Citation Index Expanded, the Research Alert, and to Current Contents/Engineering, Computing & Technology.

The illustrations on the front cover have been obtained from the ARC research group at the Department of Electrical Engineering, Colorado School of Mines

Published, sold and distributed by: River Publishers, Alsbjergvej 10, 9260 Gistrup, Denmark

MARCH 2023 REVIEWERS

Hristos T. Anastassiu
Huseyin Aniktar
Mahendran C.
Sivaprakash S. C.
Chakravarthy
Rudy Cheung
Yogesh Kumar Coukiker
Thippesha D.
Nasr H. Gad
Zi He
Taha Imeci
Mikko Kokkonen
Ashok Kumar
Neng-Wu Liu
Matteo Bruno Lodi
Mihir Narayan Mohanty
Antonino Musolino
Sathishkumar N.
Anveshkumar Nella
Marco Passafiume
Mirjana Peric
Shi Pu
Gowri Manohari Ravishankar
Sayidmarie
Haoran Sun
Siyang Sun
Sathiyapriya Thangavel
Li Wu
Yinfeng Xia
Yiyang Yu
Yadong Zhang

THE APPLIED COMPUTATIONAL ELECTROMAGNETICS SOCIETY JOURNAL

Vol. 38 No. 3 March 2023

TABLE OF CONTENTS

Women's History Month Special Article: Interview with "Professor Cynthia Furse"

Sima Noghanian

CommScope Ruckus Networks
Sunnyvale, CA, USA
sima_noghanian@ieee.org

Abstract – In this article I had the pleasure of interviewing Professor Cynthia Furse. Professor Furse is not only an internationally well-known researcher in the field of computation and applied electromagnetics (EM), but also an innovator in modern teaching techniques, an entrepreneur, an academic leader, and a true mentor for many young professionals in the electromagnetics field.

Index Terms – women in applied computational electromagnetics, women in STEM.

I. INTRODUCTION

Cynthia Furse (Cindy) is a Professor in the Electrical and Computer Engineering Department at the University of Utah. Professor Furse is a Fellow of the IEEE and the National Academy of Inventors. She is the co-founder of LiveWire Innovation and she was the Associate Vice President for Research at the University of Utah for 10 years. She is well known for her innovative teaching methods in electromagnetics, through flipped classrooms and open-source textbooks. She was the recipient of the 2020 IEEE Chen To Tai Distinguished Educator Award: "For motivating, challenging, educating and inspiring the next generation of EM engineers through innovative teaching, hands-on experiences, current research, and lively participation." This is only one example from a long list of awards for excellence in education and mentoring. Professor Furse is also well known for her research in Finite Difference Time Domain (FDTD) and computational electromagnetics, implanted antennas, and fault detection of live wires. She is currently a member of the National Science Foundation Advisory Committee, a Member of the Editorial Board of the Proceedings of the IEEE, the Award Committee Chair of the IEEE Antennas and Propagation Society, and the Technical Co-Chair of the IEEE Antennas and Propagation Symposium and URSI Symposium 2023. She is truly an inspiration and role model for young women and engineers in this field. If you get the chance to meet her in person, you always see her smiling (Fig. 1). I encourage you to read through this interview, which is in the form of questions and answers, to find many invaluable lessons and advice from Professor Furse.

Fig. 1. Professor Cynthia (Cindy) Furse.

II. QUESTIONS AND ANSWERS (Q & A)

Q: Tell me about yourself.

A: I am an electrical and computer engineering professor at the University of Utah (Fig. 2). I was born in Maine and grew up in Utah. I love rural areas and I enjoy engineering. I got my undergraduate, master's, and Ph.D. degrees all at the University of Utah, where I currently teach. This is a little bit unusual, but it gives me a lot of perspective on the place where I am. My daughter also graduated in electrical engineering and earned her master's and MBA from the University of Utah. My brother also graduated in electrical engineering; he took some classes from me. My youngest brother did a computer science degree from the University of Utah. I have a lot of different perspectives on the place where I teach. I am also an entrepreneur: I started up a spin-off company from my research called "Livewire Innovation" [1].

Submitted On: January 29, 2023
Accepted On: January 29, 2023

https://doi.org/10.13052/2023.ACES.J.380301

Fig. 2. Professor Furse with her famous Smith Chart quilt in the background. She made this quilt and all of her graduate students and senior project students sign it when they are finished with their projects.

Q: When and how did you get interested in engineering?

A: When I was in high school, I thought I was going to be a writer. Later I was going to be a veterinarian. I did an internship at a veterinary clinic. It was awesome. I became very interested in engineering when I did an internship with a pediatrician, and she showed me MRI scans. I decided I wanted to help people like her. Then I thought the person who helped people was the engineer who developed the MRI. MRI was a new technology that got me interested in the fact that engineers make such a difference in the world, and that is how I got interested in engineering. I was in high school when I discovered my interest in engineering. I decided to go into the engineering field right after high school. Engineering is a great way to apply math. I think math is very beautiful and engineers can apply math and use it and build and make things that help people. At first, I started studying mechanical engineering. Later I switched over to electrical engineering when I found so many great applications and many ways that I could use math as an electrical engineer.

Q: When did you become interested in EM?

A: It was in my junior year in college when I took the electromagnetics class from Professor Magdy Iskander. He is one of our very famous electromagnetics professors. It was so exciting and very different from other electrical engineering topics. I love digital and analog, but when I saw electromagnetics and learned that the fields do not stay on a wire, it was like magic, yet it was so predictable by Maxwell's equations. After the EM course, I took computational electromagnetics and really enjoyed it. Magdy accepted me as an undergraduate researcher, and I wrote a paper on my undergraduate research [2]. Then I did my master's under his supervision (Fig. 3). It was a fantastic experience. I learned so much and enjoyed it tremendously. I did some early Method of Moment simulations for hyperthermia for the body and in particular, the head, for applications in brain tumor treatment. After my work on the MoM, I began working with Professor Om Gandhi on FDTD, which is a better choice for modeling heterogeneous media.

Fig. 3. Professor Furse (as a graduate student) performing an experiment in the lab with her supervisor, Professor Iskander.

Q: You mentioned the mentorship of Professor Iskander. Did you have other mentors? What is the role of mentors in students' success?

A: Professor Iskander was an excellent mentor and taught me so much about research and presenting it. I also had other mentors, including some of the other graduate students in my office in the department. They always had good advice for me. They were people whom I could associate with. Even in high school, my physics teacher was the first mentor to ask me if I had thought of engineering when I did not know much about engineering. I think mentors are important for all of us. Overall, I have had quite a lot of mentors in my career. Each mentor has some strength, and when you learn from the mentors you learn from their strengths. I think when I have a variety of mentors I learn from the best in the field. I think I have more mentors now than when I was a student.

Some mentors are more senior than me, and some are even junior. It is a matrix of mentors. You always need mentors. For example, when I was associate vice president for research, the vice president of research was a great mentor who showed me how to lead a large group of people. I'd never had that experience before. I also benefited from his mentoring in teaching.

One of my favorite mentors is Professor Balanis. When I was a young student, I walked up to him when he had won an award, and I told him I wanted to be just like

him. To date, he is still my mentor. I asked my students what is the most important I can do for them as their mentor. They said the most important thing for a mentor is honesty. If someone is not doing well, the mentor should honestly tell them and show them the ways that they can do it better. You can see how my students are giving me advice that I could use.

Q: You have a passion for teaching and always look for innovative methods of teaching. Please explain more about your teaching activities.

A: Sometimes people see teaching and research as separate tasks, but they are not separable. They are two important pieces of the puzzle that go together. One thing that motivates me to be innovative and creative in my teaching is that when I was taking my junior year in engineering it was difficult. Some concepts and topics were hard. Sometimes my classes were just so hard that I cried. Sometimes, I didn't feel I belonged. Now, I look for ways for my students to learn and understand engineering topics happily, efficiently, and easily. I am always looking for ways to improve my teaching (Fig. 4).

Fig. 4. Professor Furse teaching an undergraduate class.

There have only been a few ways that electromagnetics has been taught, yet there are some teachers who are more inspiring than others. I would like to be one of the inspiring teachers and look for ways that excite my students. For example, one of the strong innovations that I have been involved with is the flipped classroom. I adopted the flipped classroom before even it had a name. I was teaching and I had students who through their military assignments had to leave and had no option to take the class for a year. To help them I video-recorded my classes on CDs or DVDs and sent them to these students. I quickly realized that the video lectures were so helpful to those students, and gradually other students came and asked me if I could make them available to them too. I put them in the library and made them accessible to all students. Students who had already come to the class used them to review the material, and they mentioned to me that they could not possibly pick up all the details that I thought in class, and having access to the video lectures helped them to review the lecture.

Tablets were just becoming available, and I couldn't even get a tablet – I ordered a tablet, and it was back ordered for like two or three months. I made my first video lectures with my little camera on a tripod and a whiteboard. You see me in those early lectures walking back and forth to turn the camera. It was not fancy at all, but they became so successful. Soon I realized that I could buy more time for my students. I always felt like when I delivered a lecture and the students would think they understood it, just to learn when they started doing their homework and needed me, I was not there to guide them. They would randomly shop for equations and try to get the answer. I thought that I wanted to "be there" when they were working on the homework problems. I tried so many ways to get more time in my class, I tried to do my lecture faster, but it just didn't work. After recording those video lectures, I realized that I could use the video and move the lecture out of class time. Students could watch it in advance and then we could spend the class time actively working on the problems together. As soon as I did that it just magically made more time and therefore more interaction with the students. They learned more, did better and liked it more. So, it turned out that the frustration with the amount of time I had in the class is what led me to do this flip class, which was in 2007, more than 10 years before COVID started [3]. The pandemic, of course, was a complete disaster, but it led to a phoenix rising out of the ashes. Only a fraction of my colleagues were using flipped classes before, now almost all of them are using them. Now both the teachers and the students have an amazing set of new skills and can collaborate remotely via many different tools. We have learned to be able to communicate effectively with our students. Not only we can work remotely but also sometimes we are enjoying and preferring it. We've learned that if we have the hybrid version of classes where students can either come to class in person or they can join online, there is no reason to miss a class. The flip class is now becoming a "hybrid flipped class" or a "hy-flex class".

Now, anyone can pick the right location and the right timing for them to learn, and we stop thinking of the class as the people sitting down right now in the class and that is the only way you can learn. This can also enable us to invite anyone to join us from anywhere, and that opens a huge amount of flexibility that we haven't even scratched the surface of yet. I think there will be more collaborations and universal universities. Because our fundamental classes are similar among different universities, while the senior-level classes are mostly based on our specialties and there are only a few specialties in every department. If we could share our specialized

classes, I think we would all become stronger. I know that it requires changes in the policies related to admission and tuition but if we share our classes mutually it will be more efficient for both parties, and that creates tremendous opportunities for our students, and yet that would be a fair arrangement. We would be sharing and collaborating equally, so I hope we do start seeing more of this teaching collaboration than we ever had before.

Q: From medical implants to finding the faults in aircraft wiring, why is applied EM important, and how it can solve problems?

A: Since the waves are invisible and you cannot see the electromagnetics, sometimes people won't realize that they're there doing important things for them. There are three important areas that electromagnetics excels, and it is even more important now than it was before.

Sensing: An example is medical imaging such as MRI and microwave radar imaging. With electromagnetic waves that can travel through the body, we are now able to look for tumors or cancers. This is like using radar imaging and the use of electromagnetic waves that travel into the ground helping us to look for oil or buried landmines. We see that electromagnetics is important in all kinds of sensing. In my research, I used sensing to find faulty wires in aircraft while the plane was working. This is a vital application because you don't want the plane to crash and sometimes these problems only happen during the flight. By the time the airplane comes back to the ground, we may not be able to locate that fault.

Communication: We can attach data to waves. Modulating the data into electromagnetic waves to be able to communicate, and send video, sound, and other types of data over long distances is a very familiar way of using electromagnetics. Cell phones now are used for all sorts of communication. Can you imagine if we had to be dragging a wire from place to place with our cell phones?! Wireless communication is an important application of electromagnetics. That includes optics. Fiber optic cables are now used for carrying data and are an essential part of communication.

Treatment: Another important application is the treatment of diseases. One of the earliest applications that I worked on was hyperthermia. That is a method of producing heat in the body (like how we use microwave ovens to heat food). By heating the tumors, you target the cancerous cells and kill them while the rest of the body is intact.

We now have so many tools, more than when my career started. We have simulation tools to simulate a portion of the body like the brain or the spinal cord. You can buy chips and put together antennas, and you can directly print antennas onto the circuit board. We have more tools and powers to creatively come up with new devices.

Q: You are a successful researcher, a passionate teacher, an inventor, and active in academic administration and scientific societies and groups, yet you find time to spend with family and have many hobbies. How do you do it all, what is your secret to work–life balance?

A: I don't know if there is a secret and often feel as if there isn't a balance. I do a lot of different professional activities, but I value my family and the fun that I like to have so very much that I don't leave it out. I learned early to schedule time and to plan so that I could do things with my kids. I made sure we did something after dinner: playing or doing homework, or doing other activities. Sometimes I felt anxious because I knew that I had more of my work waiting but it was so important to me to spend time with my young children. And now I have grandchildren and I look for opportunities to play with them. I get to see them almost every weekend and that is just delightful; I look forward to the time I spend with them. There are so many other things that I could be doing, there is always another paper or grant to be written and I am behind on things. I am always behind on some things, but I just had to schedule and plan that time for critical and important things in my life. I don't think there is a secret, but "prioritization" is essential. Prioritization does not mean when I spend time with my family, I don't get my work done, and it does not mean I get my work done and I don't spend time with my family. It means that I recognize that these two priorities are both important and they are both going to need time. It does mean that I am behind on things, and I don't do as much as I might have done if I did not spend time with my family or go horseback riding on the weekends (Figs. 5 and 6). I have chosen the set of priorities that I apply and that is different for each person. We need to respect that some people want to spend more time in one place than the other, and during different periods of their life. That does not mean you are "balanced", what it means is that you made a choice, and you should choose how you want to spend your time. I think that is the secret: "choosing the priorities and planning how to spend the time".

There is a secret after that, which is when you are with your family, doing your hobbies, or walking quietly in the woods, you should not feel guilty or unhappy that you are not working hard. You need to relax, let your mind take a break and let it do some of its jobs on its own. We all get more creative when we are fresh when we can relax and step away from problems. We feel the frustrations especially when we work very hard on something, and it is not working. Often, for engineers, this is the case. So, I might be working so hard that I can't figure it out. After I've tried everything, I don't know what else to try next. If I step away and I spend the morning horseback riding, or I go for a walk with the dogs, or

I cook dinner with my husband, those are the times that my mind will sort out the problem and give me the next thing to try. If we don't give our minds that break, they can't do their job. If we deny ourselves the time to spend with family and friends and for ourselves to do our hobbies, or be with our pets, we are not going to be better at our work, we will be worse. Making time makes you better.

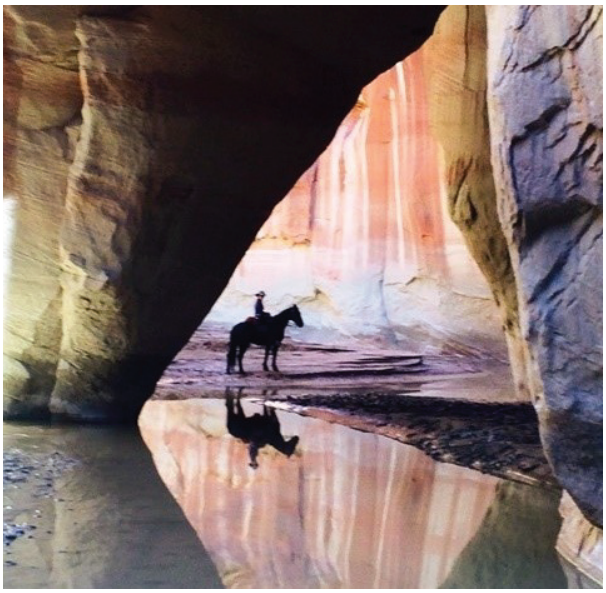

Fig. 5. Professor Furse, during one of her horseback ridings.

Q: As you are aware, the percentage of female students in this field has always been very low. What are the reasons for this and what steps can be taken to increase the percentage of female professionals in this field?

A: This is a funny question for me because I am here and did find a way and I do love it. I don't know why everyone wouldn't because it is so much fun and rewarding. Any type of science that you learn deeply has got to be exciting. We learned electromagnetics and it is exciting, fun, and fascinating. You think you may learn everything that you needed to know in the first two or three or four or ten years, but no, there are so many more things to learn. I think that many women would enjoy this now, so why might they choose something else? When you talk with a young woman who is exploring all the beautiful options before her – maybe someone in high school or maybe someone who is coming back for another career – you must look at the entire world of things that she could do and there are many options. Frankly, some options compete with engineering fields, such as medicine, law, sociology, and other excellent careers. For a young woman who is doing well in school has every opportunity in front of her, we are competing with these other opportunities. In high school, you cannot possibly have the perspective of what any of these fields feel like. I was unusually fortunate to be able to do a series of job shadows. My dad, a professor, made arrangements that I could do job shadows and see what it was like in different jobs. That made a huge difference. Creating more opportunities to spend time exploring all professions including engineering help all our students, men, and women, to recognize the things that they might find fascinating and the places where they might feel that they best fit in. When a young woman comes and does a job shadow, she also needs to see that our culture is welcoming and supportive. It must be appealing and there are times that I would have to say it is not. We need to fix that. I had a female graduate student who once told me "I don't want to be a professor because you work too hard." Then I realized that I had not been transparent and not told them about my great joys, such as spending time with my family or doing hobbies. That made me realize that I should not be hiding those anymore. Now, for example, I tell my students that I'm going horseback riding and I won't be in cell phone service for a while.

Fig. 6. Professor Furse, hiking with her husband.

When a young woman comes and looks at our profession when she does a day of a job shadow with us, she needs to see that all the managers treat everyone kindly, all the professors treat their students kindly, and

the students treat each other kindly. She needs to see that engineers are doing things that make a difference in the world. She needs to see that there are growth opportunities in every place for everyone, not just for her brother or her uncle, but for her too. She needs to see that she could move up to be a professor, a department chair, a vice president, or the president of the university. She needs to see an industry where not only she can work as an entry-level engineer but also, she can move up to become a manager. She needs to see that the individuals that a female engineer is managing will respect her and want to work with her. If she does not see that in the place where you are working, you need to change it. Some places need this change, and some places have made this change, and you know what? They are getting the best of everything. They are getting the best women and men engineers. They are getting the best diverse engineers. They are getting the best of everyone because they have made an environment that works for people. If your job environment is not like that, if you cannot bring your daughter and expect her to love it, you need to change it and make it better. Then you will be able to get the best of everything.

Tiffany Iskander, my Ph.D. student (Magdy's daughter), and I did a study on the number of women in engineering [4]. We found that sometimes the reason is cultural. In the United States, students get guidance from high school counselors. In some cases, we found that many counselors didn't realize how fantastic the engineering profession could be for a woman. Consequently, they often did not encourage bright female students to consider pre-engineering classes such as math, physics, and chemistry. They were much more likely to encourage a young male student to consider engineering. In some cases, they specifically felt that engineering was not a good career for women because there were so few women in it. We as engineers do need to reach out broadly around us and be generous with our time and energy to talk to our neighbors, our nieces or nephews, our friend's kids, and anybody who wants to come and talk to us.

Q: Do you have a memorable moment in your teaching or research that you like to share?

A: Let me share one related to your previous question on work–life balance. When I came up with the idea that turned into a company [1], I was working on finding faults in aircraft wires. I was in a group that had done a statistical evaluation of the wires. The goal was to decide when the wires must be replaced. Would it matter how many times the airplane had been used? Would it matter if it was hot or cold or wet? Would it matter if the wires went by the engine where it is hotter than it is in the regular aircraft? They were doing statistical analysis and they could not find evidence that would tell them when the wire had reached the end of its useful life. The data was showing some very peculiar results and one of the things was that most of the faults were within a foot or two of the connectors, and not along the entire length of the wire. Statistically, you would expect that if the wire was aging these types of faults would be uniformly distributed along the length of the wire. Since the faults were close to the connector it became pretty apparent that was due to mechanical stress. It might have been a maintainer disconnecting the wire for repair, drilling, or something else that happened nearby. It was happening due to an unpredictable human interaction with the wires. Therefore, the types of faults could not be statistically related. They almost always happened in flight. When they were not being used they would not show a fault. During the flight, when the wires started vibrating, going up in the air, getting wet or cold or warm, they failed. Because airplanes have been built for durability there are typically three copies of every critical system so if one fails there are two spares, that is why our planes are successful. When an airplane had a problem up in the air, they needed to locate it and fix it later. This was a clear problem in the aircraft industry, and I developed what is known as a reflectometer. We could use time domain reflectometry (TDR) to locate a fault on a wire, but the trouble was we could only use TDR on dead wires on the ground. We even built a frequency domain reflectometers system in a little box and took it to the North Island Lake Navy base, and we could not find the faults unless the wires were not active. This was because you can only find an open circuit when the wire is open, and can only find a short circuit when the wire is short-circuited. I kept saying we need to be able to find these on "live" wires. It was months after that and I tried so many ways I knew, trying all kinds of filters. Then during that time once my kids and I was visiting my parents.

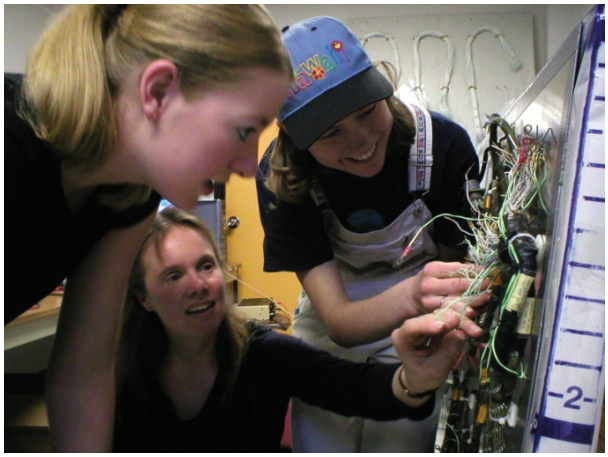

Fig. 7. Professor Furse and her students working on their research on live wire fault detection.

I was taking a shower and I watched the water randomly dripping down the shower glass door. Then I thought to myself: "Oh my gosh, I need a random signal, I need a pseudorandom signal, I need a CDMA (code division multiple access) type system, I need a spread spectrum system!" It was one of those times when I had left my work and was just relaxing and my mind did its job. It was what I needed. That idea led to the development of spread spectrum time domain reflectometry (SSTDR). It is a system that uses a pseudo-noise code and enables testing of the energized wires' impedance changes and can find faults in those wires. It is the idea behind my spin-off company, and a part of my research work today (Fig. 7). That moment of inspiration led me to the invention. It did not happen when I was working at my desk but when I was out playing.

Q. Do you have any advice for students and young professionals who are interested in the field of applied EM?

A: Just jump in and get involved. If you are a student interested in research, work with a faculty. Do a senior design project related to research through an undergraduate research experience, volunteer in a lab, and follow the professor through the day doing a job shadow. Get a good summer internship or get involved in a research experience for undergraduates (REU) through the National Science Foundation (NSF) [5]. Don't be satisfied with just the classes. Classes are important but get involved in the excitement of your field, get involved as early as you can.

To young professionals, those who have already graduated and are working their first or maybe their second job: this is a very exciting time. You have learned a lot in school, but oh my goodness, there are a lot of things to learn at your first job. You are becoming a true professional. At that point be infinitely curious. Find out what you must know. Find out about the other exciting things that are going on at your company, or other companies. Join IEEE and find out what's going on at companies around you. Talk to the people that you graduated with and find out what they are doing. Just be infinitely curious.

To senior professionals too: do the same thing, just be infinitely curious. Always look for interesting stuff in the world around you (Fig. 8). It does not have to be something that you'll use today. It might be just fascinating and you might use it sometime in the future. You cannot innovate in a field by only knowing and using the old techniques. You need ideas from other fields. That was how my innovation happened. It came out of communication theory. It was an old method in communication theory, but it was new for wire testing. You need to learn not only the topics that you use at this very moment but just be curious about the cool things around you so that you can apply them in creative ways.

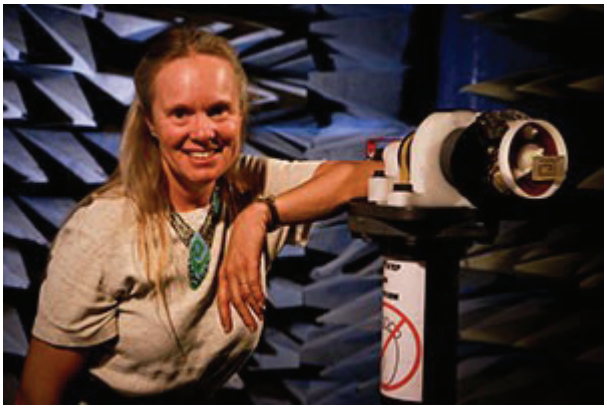

Fig. 8. Professor Furse in an anechoic chamber measuring an antenna.

Q: Do you have any additional comments?

A: Electromagnetics is the coolest thing in the world. The electromagnetic community that I have experienced has been so welcoming and embracing, creative and fun. I think it is an excellent community for new people who want to come in and join and it is a great place for women.

REFERENCES

[1] "Livewire Team." LiveWireInnovation.com. [Online]. Available: https://www.livewireinnovation.com/team/.

[2] C. M. Furse and M. F. Iskander, "Three-dimensional electromagnetic power deposition in tumors using interstitial antenna arrays," *IEEE Trans. on Biomed. Eng.*, vol. 36, October, pp. 977-986, 1989.

[3] C. M. Furse, "cfurse." YouTube.com. [Online]. Available: https://www.youtube.com/user/cfurse

[4] E. T. Iskander, P. Gore, Jr., C. Furse, and A. Bergerson, "Gender differences in expressed interests in engineering-related fields: ACT 30-year data analysis, identified trends and suggested avenues to reverse trends," *J. Career Assess.*, vol. 21, no. 4, pp. 599-613, Feb. 8, 2013.

[5] "For Students." nsf.gov. [Online]. Available: https://www.nsf.gov/crssprgm/reu/index.jsp.

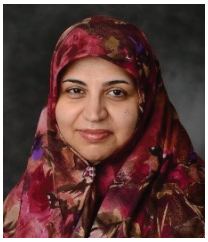

Sima Noghanian is the chair of ACES Communication and Membership Committee and serves as an Associate Editor of *ACES Journal*. She received a B.Sc. degree in Electrical Engineering from the Sharif University of Technology, Tehran, Iran, and an M.Sc. and Ph.D. degrees, both in Electrical Engineering, from the University of Manitoba, Winnipeg, Canada. She received a Postdoctoral Fellowship from the Natural Sciences and Engineering Research Council of Canada in 2002, which she took at the University of Waterloo. She was a researcher at YottaYotta Corporation, Edmonton, Canada. She was an Assistant Professor at the Sharif University of Technology, Iran, from 2002 to 2003. From 2003 to 2008, she was an Assistant Professor in the Department of Electrical and Computer Engineering, at the University of Manitoba, Canada. She was an Assistant/Associate Professor and the Director of the Applied Electromagnetic and Antenna Engineering Laboratory in the Department of Electrical Engineering, University of North Dakota, USA from 2008 to 2018. She also served as the Electrical Engineering Department Chair from 2014 to 2016 at the University of North Dakota. From 2018 to 2019 she was a visiting professor with the Department of Electrical and Computer Engineering, at San Diego State University, USA. She was an Electromagnetic Application Engineer with Phoenix Analysis and Design Technologies Inc. (PADT) (2019-2020), and a Principal Antenna Design Engineering at Wafer LLC (2020-2021). She is currently a Principal Antenna Design Engineer at CommScope. Her research interests include MIMO antennas for wireless communications, wearable and implanted antennas, 3D-printed antennas, wireless power transfer, microwave imaging, and wireless channel modeling.

Research on the Electromagnetic Emission Along the Contact Line of Electrified Trains Passing Through Neutral Sections

Liu Guang-hui, Wang Yapeng, and Li Zhenghui

School of Electrical Engineering
Zhengzhou Railway Vocational and Technical College, Zhengzhou, Henan, 451460, China
liuguanghui@zzrvtc.edu.cn

Abstract – To study the electromagnetic emission along a contact line when an electrified high-speed train passes through a neutral section, this paper models the transmission line of the traction network, provides a calculation method and boundary conditions for the parameters of the model, solves for the current distribution along the contact line, and calculates the electromagnetic emission of the contact line considering the antenna effect. Thus, the electromagnetic emission characteristics along the electrified railway are determined. Moreover, the actual electromagnetic emissions of a train passing through a neutral section are measured with a field test method and compared with the calculation results to verify the effectiveness of the model.

Index Terms – electrified high-speed railway, electromagnetic emission, electromagnetic environment test, transmission line theory.

I. INTRODUCTION

With the rapid development of transportation, science and technology, many cities in China have begun to build comprehensive transportation systems. Electrified high-speed railways (HSRs) in airports will become one of the future trends of integrated transportation. However, due to the existence of offline arcs, electrified high-speed trains generate high-frequency and broadband electromagnetic interference during operation [1–3]. Due to the mechanical vibration of the pantograph, an offline arc will be generated, which will generate high-frequency current components and radiation to the outside world. Especially when a train passes through the neutral section, it will inevitably produce an offline arc and a large number of electromagnetic emissions [4–5]. At present, many studies have been carried out on the mechanism behind the offline arc between a pantograph and a catenary [6–7], with a large number of simulation models having been developed [8–9].

In fact, the electromagnetic emissions of electrified railways include not only the offline arc of the pantograph and catenary but also that of the contact line. As early as 2001, researchers found that electromagnetic emission of the traction network is the result of the offline arc, the electromagnetic emission efficiency of the overhead line in the traction network is much higher than the offline arc of the pantograph and catenary [10]; however, this discovery has not attracted much attention. In this paper, by modeling the catenary of an electrified high-speed train, the current distribution and electromagnetic emission of the catenary are calculated to support the electromagnetic compatibility in electrified railways.

II. NEUTRAL SECTION ARRANGEMENT

As shown in Fig. 1, the public grid supplies energy for the overhead contact system (OCS), which is three-phase, despite the OCS adopting a single phase [11–12]. The external power source uses a traction substation to step down the voltage and convert three-phase AC to single-phase AC. To balance the load of the A, B and C phases of the public power system, it is generally required to implement an A and B (or A and C or B and C) phase alternating power supply. In this implementation, A and B must be separated from each other because their phases are different. Therefore, phase separation devices must be installed at the outlet of a traction substation and between two traction substations (feeding section ends).

As shown in Fig. 2, and as determined by the different running speeds of locomotives, insulated overlap or neutral insulators can be used as neutral sections [13–14]. Insulated overlaps rely on air for insulation, while

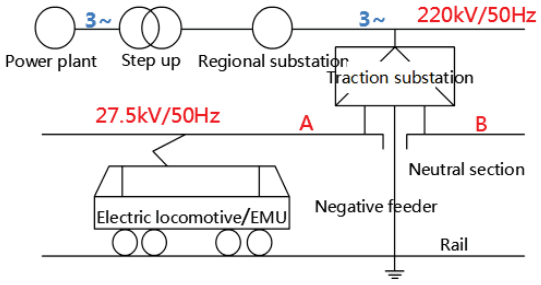

Fig. 1. Diagram of catenary power supply.

Submitted On: November 3, 2022
Accepted On: March 31, 2023

https://doi.org/10.13052/2023.ACES.J.380302

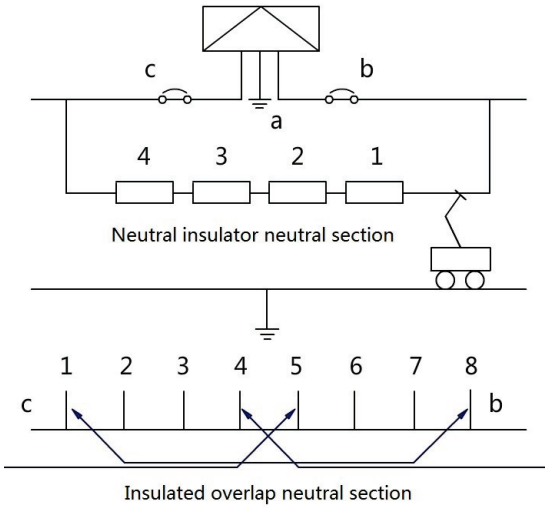

Fig. 2. Classification of neutral section.

neutral insulators rely on solid- and gas-based insulation. No matter the type of neutral section, pantograph arcing will be generated when the train passes through it.

III. TRACTION NETWORK ELECTROMAGNETIC EMISSION MODEL

When electrified trains run normally, the pantograph of the train contacts a contact wire, and the traction network supplies power through this contact line. Due to the mechanical vibration of the train during its normal driving, the pantograph and contact line will be briefly separated, and an offline gap will appear between the two lines, resulting in arc discharges between the contact wire and pantograph, as shown in Fig. 3.

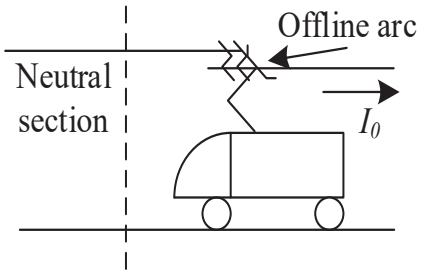

Fig. 3. Overhead contact wire model.

Many studies show that offline arcs produce conduction current excitation on a line, such that the contact line produces an external electromagnetic emission. This contact wire-destructive earth transmission line model is shown in Fig. 4. This model for the overhead line can effectively calculate the electromagnetic emission on the contact line.

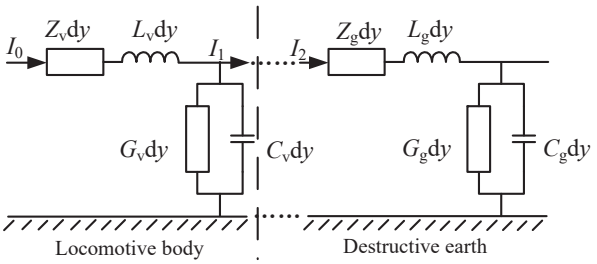

Fig. 4. Overhead line model equivalent circuit.

The model is divided into two circuits, the contact line-locomotive body circuit and the contact line-damaged earth circuit, as shown in Fig. 4. Because the contact line is a good conductor, its small impedance can be ignored, and only the locomotive body and damaged earth impedances are considered. In the model, Z_v and Z_g are the unit length impedances of the car body and damaged earth, L_v and L_g are the unit length inductances of the car body and damaged earth, C_v and C_g are the unit length capacitances of the car body and damaged earth, G_v and G_g are the unit length conductances of the car body and damaged earth, and I_0 is the initial current. Among these values, the wire impedance is [15]:

$$Z_l = \frac{1}{2r}\sqrt{\frac{\mu_l f}{\pi\sigma_l}}, \tag{1}$$

where r is the contact wire radius, σ_l is the conductor conductivity, μ_l is the conductor magnetic permeability, and f is the frequency. The locomotive body impedance is [15]:

$$Z_v = \frac{1}{4\pi r}\sqrt{\frac{\mu_v}{\pi\sigma_v f}}, \tag{2}$$

where σ_v is the locomotive body conductivity, μ_v is the car body magnetic permeability. The damaged earth impedance is [16]:

$$Z_g = \frac{j\omega\mu_0}{2\pi}\ln\frac{1+\gamma_g h}{\gamma_g h}, \tag{3}$$

where μ_0 is the vacuum permeability, h is the height between the contact line and the ground, ω=2πf, f is the frequency, and γ_g is the earth propagation coefficient, which can be written as [16]:

$$\gamma_g = \sqrt{j\omega\mu_0(\sigma_g + j\omega\varepsilon_g)}. \tag{4}$$

The system's inductance L and capacitance C can be expressed as [16]:

$$L = \frac{\mu_0}{2\pi}\ln\frac{2h}{r}, \tag{5}$$

$$C = \frac{2\pi\varepsilon_0}{\ln(2h/r)}, \tag{6}$$

where r is the radius of the wire. It is possible to obtain the contact line-car body circuit inductance L_v and capacitance C_v, and the contact line-damaged earth circuit inductance L_g and capacitance C_g. Since

there is no conducting current between the contact line and the damaged earth, G can be ignored.

The telegraph equation for the transmission line model shown in Fig. 4 can be written as [17]:

$$\frac{dU(y)}{dy} + ZI(y) = 0, \tag{7}$$

$$\frac{dI(y)}{dy} + YU(y) = 0, \tag{8}$$

and in the formulae:

$$Z = (Z_l + Z_g + L), \tag{9}$$

$$Y = \frac{1}{j\omega C}, \tag{10}$$

where the boundary condition of the model at the initial position is I_0, and the terminal is the other end of the power supply zone (the traction transformer), which can be set as an open circuit with boundary condition written as:

$$I_{a1}(y = 0) = I_0, \tag{11}$$

$$I_{a1}(y = l_v) = I_{a2}(y = l_v), \tag{12}$$

$$I_{a2}(y = l_a) = 0, \tag{13}$$

where l_v is the car body length of the contact line-car body circuit, and l_a is the entire model length (the length of the power supply zone). A general solution is obtained from equation (7) and equation (8), equations (11)–(13) are boundary conditions, so the current distribution on the contact line can be solved as follows:

$$\begin{bmatrix} 1 & -1 & 0 & 0 \\ e^{-\gamma_1 l_v} & -e^{\gamma_1 l_v} & -e^{\gamma_2 l_v} & e^{\gamma_2 l_v} \\ Z_{01}e^{-\gamma_1 l_v} & Z_{01}e^{\gamma_1 l_v} & -Z_{02}e^{-\gamma_2 l_v} & -Z_{02}e^{\gamma_2 l_v} \\ 0 & 0 & e^{-\gamma_2 l_a} & -e^{\gamma_2 l_a} \end{bmatrix} \begin{bmatrix} I_{a1}^+ \\ I_{a1}^- \\ I_{a2}^+ \\ I_{a2}^- \end{bmatrix} = \begin{bmatrix} I_0 \\ 0 \\ 0 \\ 0 \end{bmatrix}, \tag{14}$$

where γ_0 is the propagation coefficient, and Z_0 is the characteristic impedance, which can be written as [17]:

$$\gamma_0 = \sqrt{ZY}, \tag{15}$$

$$Z_0 = \sqrt{Z/Y}, \tag{16}$$

where the reflux conductors below the overhead line are different, and their corresponding impedances Z and conductors Y vary. To find the initial current I_0, a modified Habedank model [18] is used with a mathematical expression as follows:

$$\begin{cases} \frac{dg_C}{dt} = \frac{1}{\tau_0 g_H{}^n}\left(\frac{i^2}{u^2 g_C} - g_C\right) \\ \frac{dg_M}{dt} = \frac{1}{\tau_0 g_H{}^n}\left(\frac{i^2}{k g^\beta d_{max}} - g_M\right) \\ g_H = \frac{1}{g_C} + \frac{1}{g_M} \end{cases}, \tag{17}$$

where, i is the arc current, g_C is the Cassie arc model instantaneous conductance, g_M is the Mayr arc model instantaneous conductance, g_H is the instantaneous conductance of the Habedank arc model, n is a constant, τ_0 is the initial time constant, u is the Habedank arc model voltage gradient, β and k represent the power factor and dielectric coefficient of dissipation power, respectively, and d_{max} represents the maximum distance between the pantograph and contact wire.

According to the current distribution along the contact line, the electromagnetic emission can be calculated using the antenna effect. This calculation of electromagnetic emission is shown in Fig. 5. Because the calculation frequency is less than 30 MHz, the magnetic field strength is calculated directly [16]:

$$\mathrm{d}H = \frac{I(y)\mathrm{d}y}{4\pi r^2} e^{-j\frac{2\pi r}{\lambda}} \left(1 + j\frac{2\pi r}{\lambda}\right) \sin\theta. \tag{18}$$

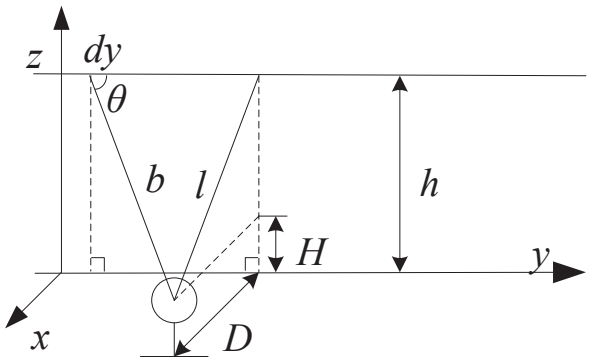

Fig. 5. Model for electromagnetic emission.

The equation's geometric relationship is shown in Fig. 5. Since the calculation frequency is less than 30 MHz and the distance r from the antenna to the contact line is much less than the calculated wavelength λ, equation (18) can be reduced according to near-field conditions $r \ll \lambda$:

$$\mathrm{d}H = \frac{I(y)\mathrm{d}y \sin\theta}{4\pi r^2}, \tag{19}$$

where:

$$r = \sqrt{D^2 + l^2 + y^2}, \tag{20}$$

$$\sin\theta = \frac{l}{b}. \tag{21}$$

Subsequently, dH is integrated in segments of the entire power supply zone, the contact line-locomotive body circuit is integrated, and the contact line-damaged earth circuit is integrated to obtain the total electromagnetic emission value:

$$\begin{aligned} H &= \int_0^{l_v} \mathrm{d}H + \int_{l_v}^{l_a} \mathrm{d}H \\ &= \frac{l}{4\pi r^2}\left[\int_0^{l_v} \frac{I(y)}{\sqrt{D^2 + l^2 + y^2}}\mathrm{d}y \right. \\ &\quad \left. + \int_{l_v}^{l_a} \frac{I(y)}{\sqrt{D^2 + l^2 + y^2}}\mathrm{d}y\right], \end{aligned} \tag{22}$$

Table 1: Used parameters

Symbol	Parameter	Symbol	Parameter
r	0.00645 m	μ_0	$4\pi\times10^{-7}$ H/m
σ_l	5.8×10^{7} S/m	ε_0	8.85×10^{-12} F/m
σ_v	2×10^{7} S/m	σ_g	0.0001 S/m
μ_l	$4\pi\times10^{-7}$ H/m	h_g	6.4 m
μ_v	1.75×10^{-7} H/m	h_v	2.4 m
D	10 m		

where $I(y)$ is the current distribution on the feeding section as calculated by equation (14). The specific calculated parameters are shown in Table 1.

IV. TRACTION NETWORK ELECTROMAGNETIC TRANSMISSION TEST

According to GB/T24338.2 [19], an EMI R&S test receiver is used from 9 kHz to 3 GHz to test the magnetic field intensity. An R&S ring antenna HFH2-Z2 is used to receive the magnetic field from 8.3 kHz to 30 MHz, and a high-frequency cable is used between them. The test position is on the field side of an electrified railway track, and electromagnetic emission values are recorded when the train is coming and without any trains (background). The test parameters are set in strict accordance with GB/T24338.2. The test instrument, test antenna, test site and test layout are shown in Fig. 6.

In Fig. 6 (d), TP represents a test point, which is the position of a receiving antenna. Test point TP_1 is used to record the electromagnetic field value when the train passes through the neutral section. Test points TP_2 and TP_3 verify the distribution of these electromagnetic emissions along the railway. Variables d_1 and d_2 are the distances between the test point and neutral section, with d_1 being 600 m and d_2 being 800 m. The test data are shown in Table 2. The values represent electromagnetic emission data tested when the vehicle passed through the neutral section, and the background values represent data tested when no locomotive passed through.

During experimentation, an electromagnetic environment test instrument is installed at a vertical distance of 10 m from the electrified railway. First, an EMI receiver is installed and connected to a 220 V power source. Second, a HFH2-Z2 ring antenna is installed with the ring plane parallel to the electrified railway. Finally, a receiver is connected to the ring antenna with a high-frequency shielding cable. These test parameters were set according to GB/T 24338-2. When no electrified trains pass, a background electromagnetic environment test is conducted, and these test data are background data. When an electrified train is coming, interference and electromagnetic tests are conducted. The

(a) EMI R&S receiver

(b) Ring antenna

(c) Test field

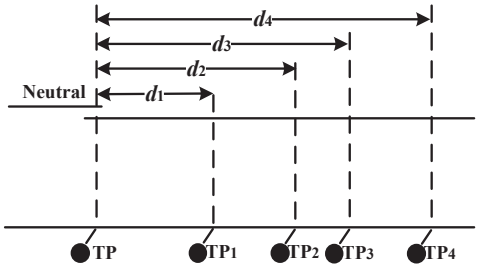

(d) Arrangement for testing

Fig. 6. Test diagram.

data obtained from these tests characterize the electromagnetic emission profiles of electrified railways when a train passes through a neutral section.

As Table 2 shows, the very stable background data are generally maintained at approximately 26 dBμA/m. The signal when a train passes through the neutral section is larger than the background signal by 40 dB to 55 dB. Since the TP is located in the neutral section, its electromagnetic emission value is the maximum

Table 2: Test data

Test Point	Background (dBμA/m)	Train Incoming (dBμA/m)
TP	27.23	81.97
TP_1	25.56	78.15
TP_2	25.12	68.67
TP_3	26.92	64.45
TP_4	26.54	54.13

and reaches 81.97 dBμA/m. The TP_1, TP_2, TP_3 and TP_4 are located along the electrified railways at 400 m, 600 m, 800 m and 1000 m away from the neutral section, respectively. Their electromagnetic emission values are smaller than that of TP, at 78.15 dBμA/m, 68.67 dBμA/m, 64.45 dBμA/m and 54.13 dBμA/m.

V. COMPARISON OF RESULTS

As Fig. 3 shows, when a train is traveling from a feeding section to the neutral section, the current distribution on the contact line can be obtained by equation (14), as shown in Fig. 7. The current distribution of the overhead line-locomotive body circuit is depicted on the left side of the dotted line. The current distribution of the overhead line-damaged earth circuit is on the right side of the dotted line. Because the locomotive body conductivity is close to that of metal, it is a good conductor.

Given the locomotive body length, the medium frequency current in the contact line is an undamped oscillation. Moreover, the current oscillation is just cyclic, and the shock amplitude appears as two peaks, which are both 2.73 mA. This shock amplitude change is the same as that of the 1 MHz sine wave amplitude oscillation.

Due to much lossy grounding impedance, the current distribution on the model decayed significantly with axial distance by approximately 0.3 mA per 100 m. Around 1500 m from the neutral section, the current distribution on the wire attenuates to 1% of the peak value, which leads to the inference that strong electromagnetic emission appears on the overhead line at the beginning of the model.

After the current distribution on the contact line is obtained, the electromagnetic emission on the line can be obtained by equation (22). This is compared to the measured data, as shown in Fig. 8.

In Fig. 8, the blue curve shows the calculation of electromagnetic emission using the above transmission line model. The red star is the electromagnetic emission value recorded by TP_2, the green star is the electromagnetic emission value recorded by TP_3, and the black curve is the maximum value of the background data. As Fig. 8 shows, when an electric locomotive passes through the neutral section, the electromagnetic emission on the contact wire attenuates by approximately 10 dB every 200 m.

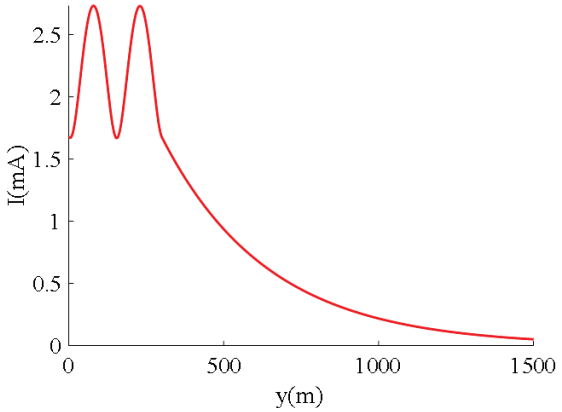

Fig. 7. Contact line current distribution curve.

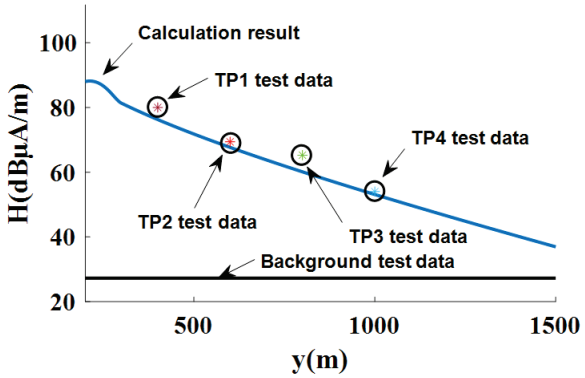

Fig. 8. Electromagnetic emission curve of the contact wire.

The calculation results agree with the measured values, which verifies the effectiveness of the model. If the distance between the neutral section and the measuring point is less than nearly 1500 m, the electromagnetic emission along the electrified railway gradually decays, from 88.16 dBμA/m to 36.95 dBμA/m. The closer to the neutral section, the greater the electromagnetic emission value is. The electromagnetic emission data measured at 600 m and 800 m from the neutral section agree with the calculation results, with differences within 3 dB. The calculation results and electromagnetic emission data are both greater than the background data, with the maximum data being 60.93 dB above the background test value. At 1500 m from the neutral section, its calculation results are 9.72 dB higher than the background data.

VI. CONCLUSION

Combined with GB/T24338.2, a model for electromagnetic emission on a contact wire is established to calculate the current distribution on the contact line, and

the antenna effect model is established for calculating the electromagnetic emission on the contact line. The electromagnetic emission characteristics on the contact wire are presented, and the electromagnetic emission mechanism is analyzed. The electromagnetic emission on the contact line changes linearly for damaged ground, which imparts an obvious attenuation of approximately 10 dB per 200 meters, and its value is approximately 88 dBμA/m at the first end.

As the distance from the neutral section increases, the electromagnetic emission value along the railway decreases to 36.95 dBμA/m at 1500 m. The electromagnetic emission data tested at 600 m and 800 m from neutral agreed with the calculation results. The model discrepancies are less than 3 dB, and the models provide values greater than the background data, proving the effectiveness of this transmission line modeling method. Using the model to research electromagnetic emissions along electrified railways, the calculation results are accurate and match the measured data. This study gives the electromagnetic emission value for a feeding section when a train passes a neutral section, to provide theoretical support for the electromagnetic compatibility of electrified high-speed railways.

ACKNOWLEDGEMENTS

This work was supported by the National Natural Science Foundation of China under Grant 62003313.

REFERENCES

[1] Y. Xiaojia, Z. Feng, and Q. Riqiang, "Radiation characteristics of pantograph-catenary arc and its influence on airport glide beacon," *Acta Aeronautica et Astronautica Sinica*, vol. 39, no. 1 pp. 253-260, 2018.

[2] Y. Jiabin, Z. Feng, and L. Jun, "Electromagnetic interference measurement and analysis of high-speed electric multiple units speed sensor," *Journal of Electronic Measurement and Instrumentation*, vol. 29, no. 3, pp. 433-438, 2015.

[3] Z. Feng, T. Yutao, and G. Chenxuan, "Mechanism and suppression of electromagnetic interference of pantograph-catenary arc to speed sensor of CRH380BL electric multiple unit," *China Railway Science*, vol. 37, no. 6, pp. 69-74, 2016.

[4] H. Lu, F. Zhu, and Q. Liu, "Suppression of cable overvoltage in a high-speed electric multiple units system," *IEEE Transactions on Electromagnetic Compatibility*, vol. 61, no. 2, pp. 361-371, 2019.

[5] L. Hede, Z. Feng, and L. Xin, "Shielding effectiveness of reinforced concrete toward electric arcs in pantograph-catenary systems of metro," *Chinese Journal of Radio Science*, vol. 31, no. 6, pp. 1209-1215, 2016.

[6] S. Midya, D. Bormann, and A. Larsson, "Understanding pantograph arcing in electrified railways - influence of various parameters," 2008 *IEEE International Symposium on Electromagnetic Compatibility*, Detroit, MI, USA, pp. 1-6, 2008.

[7] S. Midya, D. Bormann, and T. Schutte, "Pantograph arcing in electrified railways—mechanism and influence of various parameters—part II: with AC traction power supply," *IEEE Transactions on Power Delivery*, vol. 24, no. 4, pp. 1940-1950, 2009.

[8] Y. Wang, Z. Liu, and X. Mu, "An extended Habedank's equation-based EMTP model of pantograph arcing considering pantograph-catenary interactions and train speeds," *IEEE Transactions on Power Delivery*, vol. 31, no. 3, pp. 1186-1194, 2016.

[9] J. L. Guardado, S. G. Maximov, and E. Melgoza, "An improved arc model before current zero based on the combined Mayr and Cassie arc models," *IEEE Transactions on Power Delivery*, vol. 20, no. 1, pp. 138-142, 2005.

[10] B. Tellini, M. Macucci, and R. Giannetti, "Conducted and radiated interference measurements in the line-pantograph system," *IEEE Transactions on Instrumentation and Measurement*, vol. 50, no. 6, pp. 1661-1664, 2001.

[11] Y. Wang, Z. Liu, and X. Mu, "Research on electromagnetic transient process in articulated split-phase insulator of high-speed railway considering viaduct's electrical coupling," *International Transactions on Electrical Energy Systems*, vol. 27, no. 4, 2017.

[12] K. Huang, Z. Liu, and Y. Wang, "Analysis of optimal body grounding technology in case of electric multiple unit passing neutral section device," *Proceedings of the CSU-EPSA*, vol. 28, no. 5, pp. 1-8, 2016.

[13] L. Xin, "Pantograph arcing electromagnetic radiation model of high-speed train passing electric phase separation and its typical application analysis," Ph.D. dissertation, Southwest Jiaotong University, Chengdu, China, 2019.

[14] W. Ying, L. Zhigang, and M. Xiuqing, "Study on pantograph-catenary system temperature field of high-speed railway under off-line arc conditions," *Computer Simulation*, vol. 32, no. 7, pp. 154-159, 2015.

[15] L. Hongmin, Y. Zhiyong, and L. Wanyu, *Engineering Electromagnetic Compatibility*, Xi'an, China: Xidian University Press, pp. 160-162, 2010.

[16] F. M. Tesche, M. V. Ianoz, and T. Karlsson, *EMC Analysis Methods and Computational Models*, New York, NY, USA: Wiley, 1997.

[17] C. R. Paul, *Analysis of Multiconductor Transmission lines*, 2nd ed., New York, NY, USA: Wiley, 2009.
[18] W. Ying, "Studies on the heat distribution and current conduction of pantograph-catenary electric contact and their influence laws," Ph.D. dissertation, Southwest Jiaotong University, Chengdu, China, 2015.
[19] *Railway applications - Electromagnetic compatibility - Part 2: Emission of the whole railway system to the outside world*, GB/T 24338-2, Ministry of Railways, PRC, China Standards Press, Beijing, 2018.

Liu Guang-hui was born in Henan, China, in 1989. He received the B.E. degree in Electric Engineering from Xuchang University, Xuchang, China, in 2013, and the M.S. degree in Electric Engineering from Southwest Jiaotong University, Chengdu, China, in 2016. His research interests include railway power supply and EMC.

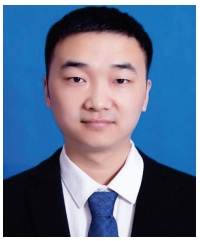

Wang Yapeng was born in Henan, China, in 1994. He received the master's degree in Electrical Engineering from East China Jiaotong University, Nanchang, China, in 2019. His current research focus is on traction power supply systems.

Li Zhenghui was born in Henan, China, in 1993. He received the B.Eng. and M.Eng. degrees in the field of fault diagnosis from Luoyang Institute of Science and Technology, China, and Hangzhou Dianzi University, China, in 2015 and 2018, respectively. His current research interests include machine learning, fault diagnosis and pattern recognition.

Scanning of the Near-field Focused Beam by Changing Frequency

Muhammad Sohail[1], Rasime Uyguroğlu[1], and Abdullah Y. Öztoprak[2]

[1]Department of Electrical and Electronic Engineering
Eastern Mediterranean University, Famagusta, 99628, Northern Cyprus
muhammad.sohail@emu.edu.tr, rasime.uyguroglu@emu.edu.tr

[2]Department of Electrical and Electronic Engineering
Cyprus International University, Nicosia, 99258, Northern Cyprus
aoztoprak@ciu.edu.tr

Abstract – A new antenna array system is introduced which enables the movement of a near-field focused beam by change of frequency. The shift in the beam is achieved by using multi-wavelength transmission lines between successive elements of the array. At the designed frequency the beam is focused at the focal point. Due to the differences in the transmission line lengths feeding the antenna elements, a progressive phase change occurs between these elements. These phase differences between the elements cause a shift in the beam position. An 8×8 patch antenna array system was designed at 2.4 GHz on a microstrip to implement the proposed system. Two substrates were used: one for the patch antenna array and the other one for the feed network and transmission lines. A full-wave simulation model was used to analyze this design and demonstrate the movement of the beam. For this design, the focused beam is moved 310 mm by changing the frequency from 2.2025 GHz to 2.5750 GHz.

Index Terms – beam shifting, focused beam, hyperthermia, near-field focusing, patch antenna array.

I. INTRODUCTION

Focusing the radiated waves from antennas at the near field has received considerable attention recently and there have been many publications on the subject [1–4]. Near-field focusing provides high power density at certain limited regions (spots), making them preferable for some applications. The applications of near-field focusing range from Radio Frequency Identification (RFID) systems [5, 6], non-contact microwave industrial inspection [7], gate access control systems [8], wireless power transfer [9, 10] to biomedical applications such as imaging, hyperthermia, and treatment/diagnosis of diseases [11–14].

In some focused field applications, it is necessary to shift the beam to different positions to apply high power at different regions, such as in hyperthermia applications [15, 16] where it is necessary to heat tissues at different locations on the human body. The shift in the focused beam in medical applications is usually carried out by moving the whole antenna system which can be very bulky, and the required accuracy may not be achieved. A new and simple method is introduced in this paper for shifting the beam without any mechanical movement.

The novel technique introduced here moves the focused field by changing the frequency. The method is very simple and does not require any phase shifters. The antenna array will focus the radiated field at a predetermined focal point and this focused field will be shifted as a function of frequency. The proposed system will have a sound mechanism for shifting the focused beam to the desired point, as well as having greater accuracy compared to systems handled using human interaction.

The proposed antenna system is composed of an array antenna fed by a power divider network. The array antenna is designed to focus the beam at a point in space. Multiple wavelength transmission lines at the designed frequencies are then added to the feed lines between successive elements leading to an antenna. This does not add an extra phase to the elements at the designed frequency, but phases at the elements change when the frequency changes, resulting in a shift in the beam position.

The design of a near-field focusing antenna array is explained in Section II, after which the principle of the movement of the beam with frequency is demonstrated by using a 16×16 array of isotropic elements at 2.4 GHz. In Section III, an 8×8 frequency scanning antenna array and feed network including the additional transmission lines have been designed on FR-4 at 2.4 GHz, and the performance of the antenna system has been analyzed using CST Microwave Simulation software.

Submitted On: July 8, 2022
Accepted On: February 15, 2023

https://doi.org/10.13052/2023.ACES.J.380303

II. METHODOLOGY

A. The method

The principle of focusing the near field at a point and the method of the movement of the focused beam is illustrated below.

A rectangular antenna array is used to explain the methodology. Figure 1 shows such an antenna lying in the x-y plane. F $(0,\ 0,\ z_f)$ is the focal point on the z-axis in the near-field and z_f is the distance from the array antenna to the focal point. As the fields are to be focused at the focal point F, the phase of the fields from each of the antenna elements should be equal at this point.

For achieving this phase equality, a set of phases are calculated to be fed to each element using quadratic phase distribution [11]. The formula for quadratic phase distribution is given by equation (1):

$$\phi_{n,m} = k \times \left(\sqrt{\left((x_n)^2 + (y_m)^2 + (z_f)^2 \right)} - z_f \right), \quad (1)$$

where $x_n,\ y_m$ are the position of $(n,m)^{th}$ element in the array and $(0,\ 0,\ z_f)$ is the focal point. k is the wave number in rad/m**.** The calculated phases are fed to respective elements and as a result of having the same phases at the focal point, constructive interference occurs forming a focused spot. The required quadratic phases at the antenna elements can be obtained by additional transmission lines. The lengths of the additional transmission lines are different for each element and are calculated by using equation (2). Given that the total electrical distance from the reference point to the focal point should be equal for all elements for phase equality,

$$w_{n,m} + \overline{PF_{n,m}} = w_0 + \overline{OF}, \quad (2)$$

where,

$$\overline{PF_{n,m}} = \sqrt{{x_n}^2 + {y_m}^2 + {z_f}^2}, \quad (3)$$

$$\overline{OF} = z_f. \quad (4)$$

Figure 2 is used to show the parameters of equation (2-4). This figure consists of a plane that includes an x_n = constant line array and the focal point. Parameter $w_{n,m}$ is the length of the transmission line for $(n,m)^{th}$ element, w_0 is the length of the transmission line corresponding to the element at the origin and $\overline{OF}$ is the distance of the focal point from the origin, P is the position of the $(n,m)^{th}$ and $\overline{PF_{n,m}}$ is the distance between the $(n,m)^{th}$ element of the array and the focal point.

The focused beam above is static and cannot be shifted unless a new set of phases are fed, or the antenna aperture is shifted physically. Moving the focused beam by physically changing the position of the antenna array system is less efficient, inaccurate, and time consuming.

In this study, the shift in the beam position is achieved by adding multiple wavelength transmission lines at the designed frequency to successive y-direction elements. (There will therefore be an additional λ_0 transmission line leading to $m = 2$ elements as compared to $m = 1$ elements, and there will be a $2\lambda_0$ transmission line leading to $m = 3$ elements compared to $m = 1$ elements, etc., where λ_0 is the wavelength at the design frequency).

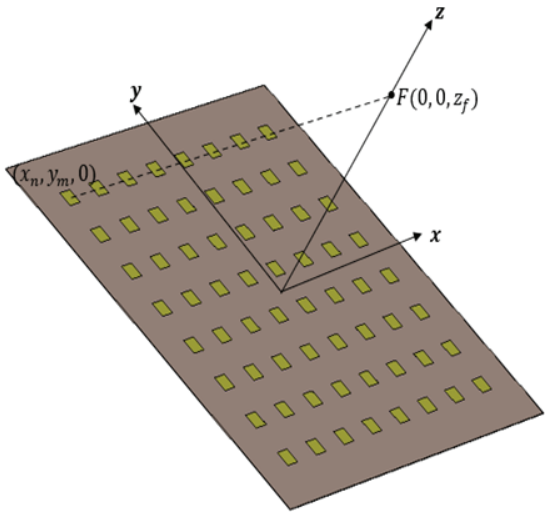

Fig. 1. Near-field focused patch antenna array.

Adding extra transmission line lengths at the design frequency does not add an extra phase to the elements of the array at this frequency. However, when the frequency is changed, the lengths of the transmission lines in terms of the wavelength are no longer equal to multiple wavelengths. This will cause a progressive phase change between the elements resulting in a shift in the beam position.

B. Movement of the beam by frequency change

In Section II A. above, it has been explained that the movement of the beam can be achieved by adding multiple wavelength transmission lines leading to the elements of an antenna array. A uniform 16×16 array antenna is used for this purpose. The elements of this antenna array are point radiators and they have equal amplitude. The design frequency is 2.4 GHz while the separation between the elements is 87.5 mm (0.7λ) in x and y-directions. λ is the free space wavelength. The focal point is F $(0,\ 0,\ z_f)$, with $z_f = 1250$ mm. The elements are fed through transmission lines having lengths $w_{n,m}$ calculated by using equation (2) and given in Table 1. In addition to $w_{n,m}$ long transmission lines, the successive elements of the array in the y-direction are fed with additional transmission lines of multiple wavelengths**,** as explained in Section II A. The total length of the additional transmission lines therefore becomes,

$$w'_{n,m} = \quad w_{n,m} + (m-1)\lambda_0. \quad (5)$$

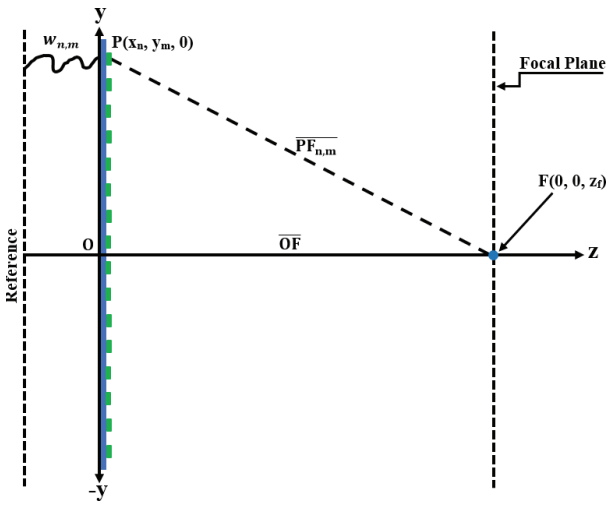

Fig. 2. The geometry of the focusing antenna array.

As the multiple wavelengths transmission lines above are added in the y-direction, the motion of the beam will be in the y-direction.

The transmission line lengths, $w_{n,m}$ for the 16×16 array, are given in Table 1. Only a sub-array of 8×8 is given due to the symmetry and large size of the array. The transmission line lengths are given in terms of wavelength at 2.4 GHz. The physical lengths of these additional lines will be dependent on the type and medium that they are constructed in.

Table 1: Transmission line lengths, $w_{n,m}$ for 8×8 sub-array

$w_{n,m}$	8	7	6	5	4	3	2	1
8	1.30 λ_0	0.99 λ_0	0.72 λ_0	0.49 λ_0	0.30 λ_0	0.16 λ_0	0.06 λ_0	0.01 λ_0
7	1.36 λ_0	1.04 λ_0	0.77 λ_0	0.54 λ_0	0.35 λ_0	0.20 λ_0	0.11 λ_0	0.06 λ_0
6	1.48 λ_0	1.16 λ_0	0.88 λ_0	0.65 λ_0	0.45 λ_0	0.31 λ_0	0.21 λ_0	0.16 λ_0
5	1.65 λ_0	1.32 λ_0	1.04 λ_0	0.81 λ_0	0.62 λ_0	0.47 λ_0	0.37 λ_0	0.32 λ
4	1.90 λ_0	1.57 λ_0	1.29 λ_0	1.05 λ_0	0.85 λ_0	0.69 λ_0	0.59 λ_0	0.54 λ_0
3	2.23 λ	1.90 λ_0	1.60 λ_0	1.36 λ_0	1.15 λ_0	1.00 λ_0	0.90 λ_0	0.84 λ_0
2	2.68 λ_0	2.33 λ_0	2.03 λ_0	1.76 λ_0	1.56 λ_0	1.40 λ_0	1.29 λ_0	1.23 λ_0
1	3.26 λ_0	2.90 λ_0	2.58 λ_0	2.31 λ_0	2.09 λ_0	1.92 λ_0	1.81 λ_0	1.75 λ_0

When the array is fed at 2.4 GHz the beam focuses at the focal point and when the frequency is changed, the phases at the radiators will change and the beam will move along the y-axis. The electric field intensity is calculated at each point along an observation line in the y-direction passing through the focal point. The field calculation is carried out by summing the electric field intensity from each of the array elements at the observation point by using equation (6) below:

$$E = A \sum_{n=1}^{16} \sum_{m=1}^{16} \frac{e^{-jkr}}{r}, \tag{6}$$

where A is a constant,

$$r = \sqrt{x_n^2 + (y_m - y)^2 + z_f^2}, \tag{7}$$

and y is the distance along the y-direction at the line of observation.

The radiation patterns calculated by equation (6) are shown in Fig. 3 for different frequencies along the y-axis passing through the focal point. It can be observed that the peak of the beam at the design frequency 2.4 GHz is at y=0, as expected. Figure 3 also shows that when the frequency is increased the beam moves in the positive y-direction, and as the frequency is decreased the beam moves in the negative y-direction.

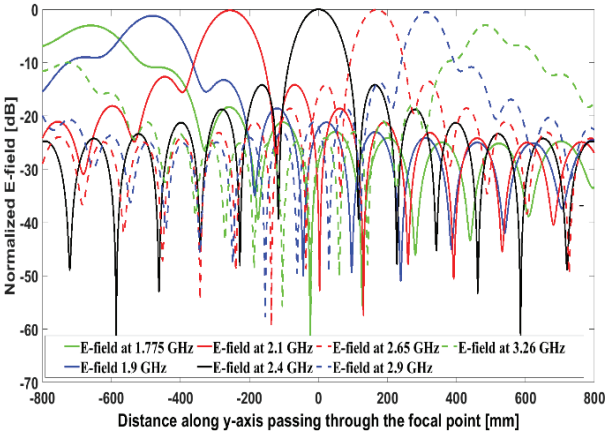

Fig. 3. Normalized E-field for 16×16 antenna array at different frequencies.

As the beam shifts away from the focal point, the beam deteriorates with lower gain, wider beamwidth, and higher sidelobes. The peak value drops by 3 dB for 3.260 GHz at positive 490 mm and the peak value drops by 3 dB for 1.775 GHz at negative 660 mm in the y-direction. The beam can therefore be scanned along a total distance of 1150 mm for this particular design.

III. DESIGN AND ANALYSIS OF SCANNING FOCUSED PATCH ANTENNA ARRAY

A. The design

A microstrip patch antenna array has been designed and analyzed to show the feasibility of the frequency scanning of the focused antenna array. As the design of a

16×16 or larger array having varied additional transmission line lengths would be very complex, an 8×8 element array has been chosen for the implementation. Two substrates have been used for implementing the system on the microstrip. The long transmission lines necessitated the use of two substrates. Having the feed network isolated from the patch array has the advantage of reducing the serious radiation from the power dividers. The two substrates use a common ground plane [17] as shown in Fig. 4 (c).

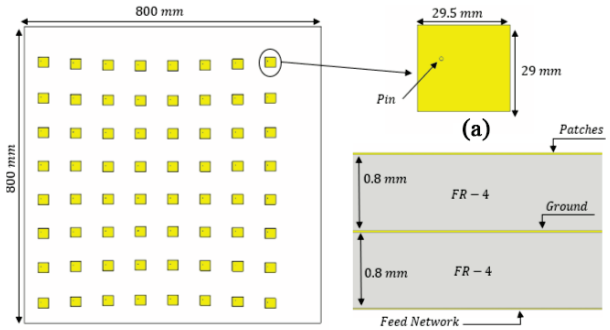

Fig. 4. Antenna array design (a) front view, (b) single element patch, and (c) side view.

Figure 4 (a) shows the front view of the patch antenna array. The separation between the elements of the patch antenna array is 87.5 mm and the total size of the microstrip antenna array is 800 x 800 mm. The feed network [18] and transmission lines of the above design are shown in Fig. 5.

The substrates are FR-4 with $\varepsilon_r = 4.3$, each having a thickness of 0.8 mm. The focal point of the array is 1250 mm from the origin of the array. The pin- fed rectangular patch antenna elements [19] are used as they are suitable for this antenna system which has two substrates. The position of the pin is (-6, 2.5) mm with reference to the center of the patch element. The feed network and the patches are connected through conducting pins as shown in Fig. 4 (b).The lower end of each pin is connected to the feedline while the upper end is connected to the patch, passing through both substrates and the ground plane. A section of 2.5 mm diameter around each pin is removed from the ground plane to avoid creating a short circuit. The pin position for patch antennas is calculated such that they are matched at the design frequency [20]. The length and width of the patch antenna elements are 29 mm and 29.5 mm respectively. These dimensions are obtained as in [11].

The phase delays required for each patch antenna element for focusing at the focal point at 2.4 GHz are obtained by using the transmission line lengths $w_{n,m}$ as shown in Table 2.

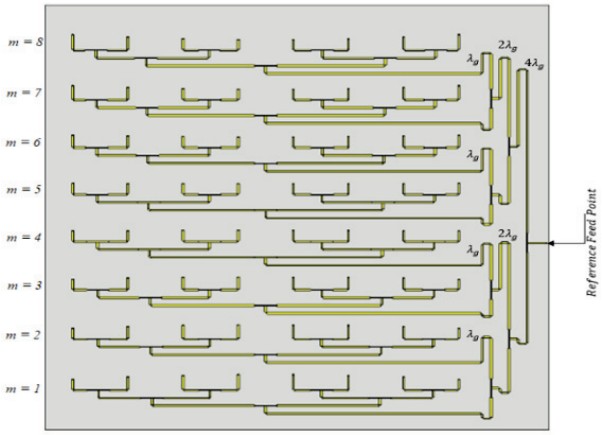

Fig. 5. Feed network and transmission lines of the antenna system.

Table 2: Transmission line lengths, $w_{n,m}$ in mm for 8×8 array

$w_{n,m}$	8	7	6	5	4	3	2	1
8	77.3	58.7	46.2	39.9	39.9	46.2	58.7	77.3
7	57.0	38.8	26.5	20.3	20.3	26.5	38.8	57.0
6	44.1	26.0	13.8	07.7	07.7	13.8	26.0	44.1
5	37.7	19.7	07.6	01.5	01.5	07.6	19.7	37.7
4	37.7	19.7	07.6	01.5	01.5	07.6	19.7	37.7
3	44.1	26.0	13.8	07.7	07.7	13.8	26.0	44.1
2	57.0	38.8	26.5	20.3	20.3	26.5	38.8	57.0
1	77.3	58.7	46.2	39.9	39.9	46.2	58.7	77.3

Additional one wavelength (approximately 67 mm) microstrip transmission lines are added between successive elements in the y-direction. The characteristic impedance of the transmission line is 50 Ω and the width of these lines is 3.05 mm. Equal power dividers are used to obtain equal power at each antenna array element. These power dividers are designed as in [11].

B. The analysis

The above design was analyzed by using CST Microwave Simulation software. Figure 6 shows the S_{11} of this 8×8 rectangular patch antenna array system. The magnitude of the reflection coefficient is in the order of −30 dB at the center frequency of 2.4 GHz and is less than −15 dB over the frequency range of interest. It can be observed that minimum reflections occurs at a frequency 1% below the center frequency which may have been caused by rounding up the transmission line lengths.

Figure 7 illustrates the normalized electric field along the x and y directions at the center frequency. As expected, at the design frequency both plots have maximum magnitudes at the focal point. The side lobe levels are below −10 dB in both x and y-directions. The half

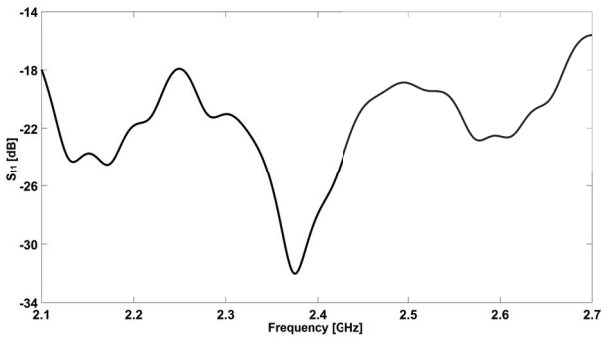

Fig. 6. S_{11} of the system.

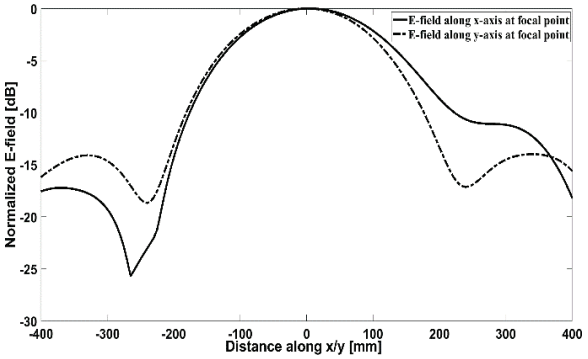

Fig. 7. Normalized E-field along x and y at the focal point.

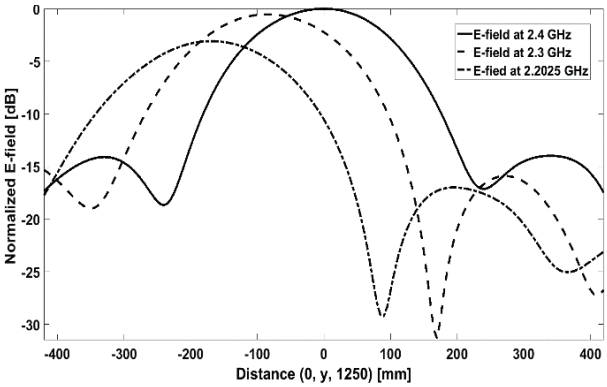

Fig. 8. Normalized E-field at the focal point for 2.2025 GHz, 2.3 GHz, and 2.4 GHz.

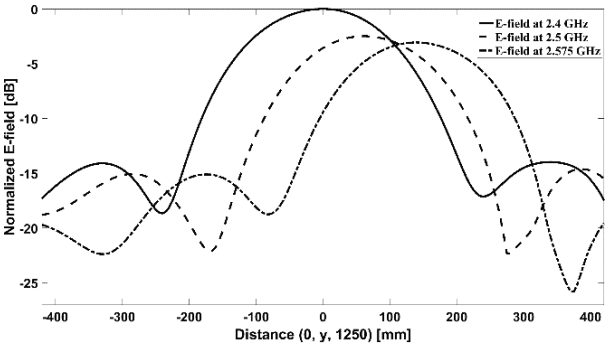

Fig. 9. Normalized E-field at the focal point for 2.4 GHz, 2.5 GHz, and 2.575 GHz.

power beamwidth of the focused beam at the center frequency is approximately 200 mm in both directions.

Figure 8 shows the shift in the focused beam along the y-axis in the negative direction as the frequency is decreased from 2.4 GHz to 2.2025 GHz. The peak magnitude of the focused field decreases as it moves away from the focal point. The distance between the peak values of frequencies 2.4 GHz and 2.2025 GHz, where the magnitude of the focused fields reduces by 3 dB, is 170 mm. The amount of shift in the focused beam depends on the distance of the focal point from the array, the separation between the array elements, and the change in the frequency. The shift due to the change in frequency is linear for small frequency changes but becomes nonlinear as the distance is increased from the focal point. For this design, the shift is approximately 74 mm per 0.1 GHz.

Figure 9 shows the shift in the focused beam along the y-axis in the positive direction as the frequency is increased from 2.4 GHz to 2.575 GHz. The peak magnitude of the focused field decreases as it moves away from the focal point. The distance between the peak values at 2.4 GHz and at the frequency 2.575 GHz, where the magnitude of the focused fields reduces by 3 dB, is 140 mm.

The above results show that the total shift of the focused fields along the y-axis is approximately 310 mm, therefore validating the principle that the focused beam can be shifted by a considerable distance by changing the frequency.

The shifting distance of the beam can be larger for larger-size arrays, as shown in Section II B. Although there have been many publications on near-field focusing and electronic beam scanning in the far field [21–23], no specific paper was found on the electronic scanning of fields in the near field. Although it was not possible to compare the focused scanned beams with any published paper, the results of the beam at the focal point compare well with [3].

IV. CONCLUSION

This paper presented a new antenna system for shifting the focused beam by change of frequency. The movement of the focused beam was achieved by using additional one wavelength transmission lines between successive elements of the array. After establishing the principle of the movement of the focused beam, a 16×16 element antenna array with point radiators was used to demonstrate this principle.

The antenna array was designed for 2.4 GHz and had a focal length of 1250 mm. It was shown that the beam of this antenna system could be shifted by 1150 mm in the focal plane by changing the frequency from 1.775 GHz to 3.26 GHz. As the design of a 16×16 array with varied additional transmission line lengths would be very complex, an 8×8 element array was used for the implementation of the frequency scanning antenna system. This antenna system was implemented on two microstrip substrates having patch antennas on one substrate and a feed network on the other.

The additional transmission lines were incorporated into the feed network design. A full-wave simulation study was carried out using CST simulation software. The simulation results show that the S_{11} of this antenna system is satisfactory, being less than -15 dB over the frequency range of interest. The focused beam moved by 310 mm by changing the frequency from 2.2025 GHz to 2.575 GHz. The study demonstrated that by changing the frequency, the focused beam can be shifted a considerable distance by using the system introduced in this paper.

REFERENCES

[1] S. M. Mikki and Y. M. M. Antar, "A theory of antenna electromagnetic near field—Part I," *IEEE Transactions on Antennas and Propagation*, vol. 59, no. 12, pp. 4691-4705, 2011.

[2] S. M. Mikki and Y. M. M. Antar, "A theory of antenna electromagnetic near field—Part II," *IEEE Transactions on Antennas and Propagation*, vol. 59, no. 12, pp. 4706-4724, 2011.

[3] P. Nepa, A. Buffi, A. Michel, and G. Manara, "Technologies for near-field focused microwave antennas," *International Journal of Antennas and Propagation,* pp. 1-17, 2017.

[4] H. Zhang, N. Shlezinger, F. Guidi, D. Dardari, M. F. Imani, and Y. C. Eldar, "Beam focusing for near-field multiuser MIMO communications," *IEEE Transactions on Wireless Communications*, vol. 21, no. 9, pp. 7476-7490, 2022.

[5] S. H. Zainud-Deen, H. A. Malhat, and K. H. Awadalla, "Dielectric resonator antenna phased array for fixed RFID reader in near field region," *Japan-Egypt Conference on Electronics, Communications and Computers*, Alexandria, Egypt, pp. 102-107, 2012.

[6] A. Buffi, A. A. Serra, P. Nepa, H. T. Chou, and G. Manara, "A focused planar microstrip array for 2.4 GHz RFID readers," *IEEE Transactions on Antennas and Propagation*, vol. 58, no. 5, pp. 1536-1544, 2010.

[7] M. Bogosanovic and A. G. Williamson, "Microstrip antenna array with a beam focused in the near-field zone for application in noncontact microwave industrial inspection," *IEEE Transactions on Instrumentation and Measurement*, vol. 56, no. 6, pp. 2186-2195, 2007.

[8] A. Buffi, A. Serra, P. Nepa, G. Manara, and M. Luise, "Near field focused microstrip arrays for gate access control systems," *Antennas and Propagation Society International Symposium*, *APSURSI'09. IEEE*, North Charleston, SC, USA, pp. 1-4, 2009.

[9] H. Zhang, N. Shlezinger, F. Guidi, D. Dardari, M. F. Imani, and Y. C. Eldar, "Near-field wireless power transfer with dynamic metasurface antennas," *IEEE 23rd International Workshop on Signal Processing Advances in Wireless Communication (SPAWC),* Oulu, Finland, pp. 1-5, 2022.

[10] V. R. Gowda, O. Yurduseven, G. Lipworth, T. Zupan, M. S. Reynolds, and D. R. Smith, "Wireless power transfer in the radiative near field," *IEEE Antennas and Wireless Propagation Letters*, vol. 15, pp. 1865-1868, 2016.

[11] F. Tofigh, J. Nourinia, M. Azarmanesh, and K. M. Khazaei, "Near-field focused array microstrip planar antenna for medical applications," *IEEE Antennas and Wireless Propagation Letters*, vol. 13, pp. 951-954, 2014.

[12] F. Samadi, "Characteristic improvement of near field focused array microstrip planar antenna in ISM band," *Microwave and Optical Technology Letters*, vol. 57, no. 7, pp. 1590-1593, 2015.

[13] P. Nepa and A. Buffi, "Near-field-focused microwave antennas; near-field shaping and implementation," *IEEE Antenna and Propagation Magazine*, vol. 59, no. 3, pp. 42-53, 2017.

[14] R. S. Mpanda, L. Qi, Q. Liang, L. Xu, J. Shi, and L. Zhao, "Design and evaluation of typical antennas for monitoring vital signs," *Applied Computational Electromagnetics Society (ACES) Journal*, vol. 34, no. 3, pp. 497-505, 2019.

[15] G. G. Bellizi, T. Drizdal, G. C. V. Rhoon, L. Crocco, T. Isernia, and M. M. Pauides, "The potential of constrained SAR focusing for hyperthermia treatment planning: analysis for the head & neck region," *Physics in Medicine and Biology*, vol. 64, pp. 1-10, 2019.

[16] R. Gaffoglio, M. Righero, G. Giordanengo, M. Zucchi, and G. Vecchi, "Fast optimization of temperature focusing in hyperthermia treatment of subsuperficial tumors," *IEEE Journal of Electromagnetics, RF and Microwaves in Medicine and Biology*, vol. 5, no. 3, pp. 286-293, 2021.

[17] N. M. Bahar and S. H. Sedighy, "Low-cost and low-profile phased array antenna for satellite reception using optimized tracking algorithm," *Iranian*

Journal of Science and Technology, Transactions of Electrical Engineering, vol. 44, pp. 1559-1569, 2020.

[18] A. T. Alreshaid, O. Hammi, M. S. Sharawi, and K. Sarabandi, "A compact millimeter-wave slot antenna array for 5G standards," *IEEE 4th Asia-Pacific Conference on Antennas and Propagation (APCAP)*, Bali, Indonesia, pp. 84-85, 2015.

[19] G. Breed, "The fundamentals of patch antenna design and performance," *High Frequency Electronics Magazine*, pp. 48-51, 2019.

[20] R. Rachmansyah, A. Irianto, and A. B. Mutiara, "Designing and manufacturing microstrip antenna for wireless communication at 2.4 GHz," *International Journal of Computer and Electrical Engineering*, vol. 3, no. 5, pp. 670-675, 2011.

[21] R. L. Haupt, "Phased array beam steering through serial control of the phase shifters," *Applied Computational Electromagnetics Society (ACES) Journal*, vol. 32, no. 12, pp. 1140-1143, 2017.

[22] B. Ku, P. Schmalenberg, O. Inac, O. D. Gurbuz, J. S. Lee, K. Shiozaki, and G. M. Rebeiz, "A 77–81-GHz 16-element phased-array receiver with ±50◦ beam scanning for advanced automotive radars," *IEEE Transactions on Microwave Theory and Techniques*, vol. 62, no. 11, pp. 2823-2832, 2014.

[23] P. Nayeri, F. Yang, and A. Z. Elsherbeni, "Beam-scanning reflectarray antennas: a technical overview and state of the art," *IEEE Antennas and Propagation Magazine*, vol. 57, no. 4, pp. 32-47, 2015.

Muhammad Sohail received his B.S. degree in Electrical Engineering from City University, Pakistan, in 2013 and his M.S. degree in Electrical and Electronic Engineering from Eastern Mediterranean University in 2016. He is currently a Ph.D. student in the Department of Electrical and Electronic Engineering at Eastern Mediterranean University. His current research interests include planar antennas, arrays, and near field focusing of planar arrays.

Rasime Uyguroğlu received her B.S., M.Sc., and Ph.D. degrees in Electromagnetics and Antennas from the Electrical and Electronic Engineering Department, Eastern Mediterranean University. She is currently an Associate Professor at the same university and also serves as the Department Chair. Her research interests include computational methods in electromagnetics, Beam Forming Networks, Rotman Lenses, Microwave Antennas, and implant antennas. Dr. Uyguroğlu is a member of the IEEE.

Abdullah Y. Öztoprak received his Ph.D. degree in Electrical and Electronic Engineering from University College London, University of London, United Kingdom, in 1977. He was appointed at Eastern Mediterranean University (EMU) as Assistant Professor, Associate Professor, and Professor in 1986, 1988, and 1997 respectively. At EMU he served as Chairman of the Department of Electrical and Electronic Engineering (1989-1992), as Vice-Rector for Academic Affairs (1992-2003), and as Rector (2009-2014). Prof. Öztoprak's research interests include Beam Forming Networks, Rotman Lenses, Microwave Antennas, Split-step Finite-Difference Time-Domain Methods, and Unconditionally Stable Finite-Difference Time-Domain Methods.

An Omnidirectional Antenna with Multi-taper Conformal Structure

Zhaoneng Jiang[1, 2], Yongxin Sha[1], Xiaofeng Xuan[1], and Liying Nie[1]

[1]School of Electronic Science and Applied Physics
Hefei University of Technology, Hefei, 230009, China

[2]National Mobile Communications Research Laboratory
Southeast University, Jiangsu, 210096, China
jiangzhaoneng@hfut.edu.cn

Abstract – In this paper, a wideband quadrangular pyramid conformal printed dipole antenna is designed, manufactured, and tested. The proposed antenna comprises four dipoles pointing in different directions and four pairs of parasitic patches. Each dipole and pair of parasitic patches are placed on one side of the pyramid. The simulated impedance bandwidth exceeds 26% (S11 $\leq$ -10 dB), with the conformal taper varied from 0° to 20°. Omnidirectional radiation characteristics can be realized within the working bandwidth. The prototype of the proposed antenna with 10° taper is fabricated and measured. Moreover, the results show that the operating frequency band is 2.28-3.58 GHz in the S-band. The size of the fabricated antenna is 35 $\times$ 35 mm^2. The conclusion is that the simulation and test results of the 10° taper antennas are highly consistent.

Index Terms – conformal, multi-taper, omnidirectional.

I. INTRODUCTION

To achieve communication, detection, navigation, and other functions, various antenna types are required for a single piece of equipment. The advantage of reducing the influence on the aerodynamic performance of mobile carriers was shown by the conformal antenna due to it fitting closely to the surface of the equipment. They have therefore been widely used in military and civilian applications such as unmanned aerial vehicles [1], missile heads, borehole radar [2], global satellite navigation systems (GSNS) [3], wearable devices [4], vehicle-borne devices [5, 6], and other wireless communication terminal devices that need a conformal configuration [7]. A conformal antenna with strong adhesion and integrated design has since become one of the research hotspots in the field of antennae.

Omnidirectional radiation antennae are widely used in short-range detection, scanning, and so on because of their wide beamwidth and radiation coverage. Compared with directional antennae, which can only receive radiation signals in a specified direction, omnidirectional antennae do not have strict requirements on the azimuth of the transmitted signal. This dramatically improves the efficiency of short-distance signal transmission. The combination of traditional omnidirectional antenna and conformal antenna design significantly expands the application of such antennae in the area of detection. A bipolar omnidirectional antenna conformal to the capsule surface for endoscopy systems is presented in [8]. However, the proposed antenna has a high specificity for application due to the capsule shape of the conformal carrier and the low gains effect. A characteristic mode analysis (CMA)-based omnidirectional microstrip antenna conformal to different radians is presented in [9]. The designed broadband circularly polarized (BCP) antenna unit can achieve 35.6% impedance bandwidth and 22% circularly polarized bandwidth under different bending radii along the x- and y-axes. However, the omnidirectional radiation characteristics of the antenna mainly depend on the radian of the carrier and the number of antenna units. In order to obtain low gain variation in the horizontal plane, a conformal array antenna requires more elements, which complicates the antenna feeding network. To simplify the design complexity of the conformal omnidirectional antenna and widen the impedance bandwidth of the antenna, a multiband antenna based on inkjet-printing is proposed in [10]. The operating bandwidth of the antenna can cover Global Positioning Systems (GPS), Wireless Local Area Networks (WLAN), Bluetooth, and other bands. The relative bandwidth can reach 54.4%, 14%, 23.5%, and 17.2%, respectively. At the same time, due to the conformality of the inkjet-printed antenna, the experimental results show that the impedance bandwidth of the antenna is basically unchanged, and the omnidirectional radiation gain is above -1.2 dBi with cylinder radii of 78 mm and 59 mm. To obtain higher radiation gain, an omnidirectional conformal antenna based on dipole form is

Submitted On: January 13, 2023
Accepted On: April 12, 2023

https://doi.org/10.13052/2023.ACES.J.380304

proposed in [11]. The antenna can achieve a maximum circular polarized radiation gain of 5.2 dBi within the relative impedance bandwidth of 55.8%. Besides, the radiation performance of the antenna is studied, which is conformal to the cylindrical section with a horizontal downward oblique angle of 0°-30°, respectively.

In order to further simplify the antenna structure based on the design of the document [11] and reduce the antenna design size, the antenna can be adapted to different conformal tapers. A conformal dipole antenna with omnidirectional radiation characteristics is presented in this paper. The experimental simulation results show that the antenna can achieve omnidirectional radiation characteristics in the full bandwidth when the pyramid taper varies from 0° to 20°. The radiation gain is higher than 1dB in the working bandwidth.

The main innovation of this paper is to design an omnidirectional radiation antenna based on bent arm dipoles. By introducing a parasitic patch, the bandwidth of the omnidirectional antenna is extended, and the conformal of the antenna on the surface of the pyramid is realized.

This paper is organized as follows. The design and analysis of the antenna are presented in Section II. Experimental results are described in Section III. Finally, the conclusion is given in Section IV.

II. ANTENNA DESIGN AND ANALYSIS

A. Planar omnidirectional antenna design

A multi-view of the proposed omnidirectional antenna is presented in Fig. 1, which comprises four dipoles. A circular low-cost FR4 substrate material (εr = 4.4) with a height of 0.508 mm is used to print this antenna.

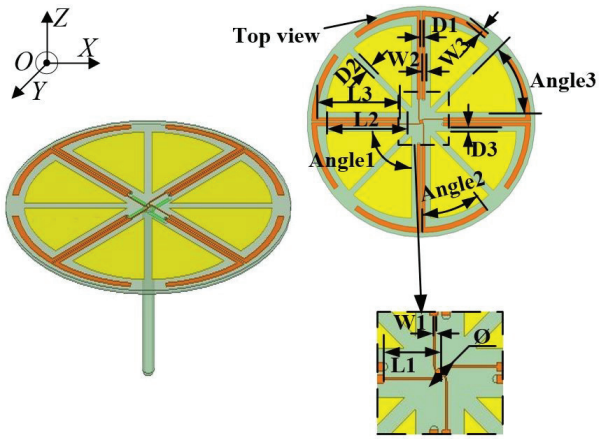

Fig. 1. The structure of the planar antenna.

The dimensions of the microstrip patch antenna in Fig. 1 are optimized by high frequency structure simulator (HFSS) software, and the parameters are shown in Table 1. It can be seen from Fig. 1 that the structure of the antenna is relatively simple, of low cost, and easily applied in practical engineering terms.

Table 1: Dimensions of the proposed antenna element (unit: mm)

Symbol	Value	Symbol	Value
L1	7	*D2*	2
L2	30	*H*	0.508
L3	*33*	*Ø*	*1.2*
W1	*0.25*	*D1*	*0.5*
W2	*1*	*Angle 1*	*90°*
W3	*1.6*	*Angle 2*	*37.5°*
D3	*2.58*	*Angle 3*	*30°*

The result of the impedance matching is shown in Fig. 2 (b). The inner conductor of the antenna is connected to a microstrip line extending in four directions on the upper surface. The outer is connected to the corresponding microstrip lines on the lower surface and then, through metalized vias, connects the ground line to the upper surface, forming a dipole form with the original microstrip structure. The four microstrip dipoles on the substrate in different directions enable the antenna to obtain specific omnidirectional radiation characteristics.

Figure 3 shows the equivalent circuit of the dipole unit, in which Cf and Lf represent the feeding capacitance and inductance, respectively, and their influence is negligible for the input impedance. When the dipole antenna works in the base model state, the electric dipole can be replaced by a series resonant circuit (resistance Rd, capacitance Cd, and inductance Ld), and the equivalent capacitance of the parasitic patch circuit is Cpp, and the inductance is Lpp.

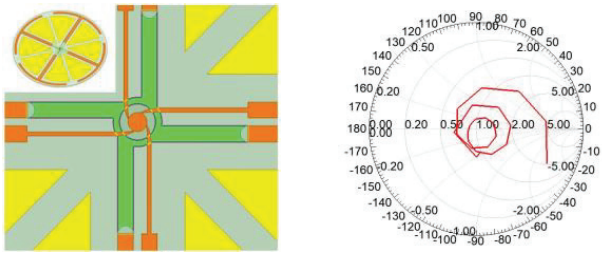

(a) (b)

Fig. 2. (a) The impedance matching circuit; (b) the Smith circle of the matching circuit.

To match impedance, an impedance matching circuit is shown in Figs. 2 (a) to connect the 50Ω SubMiniature

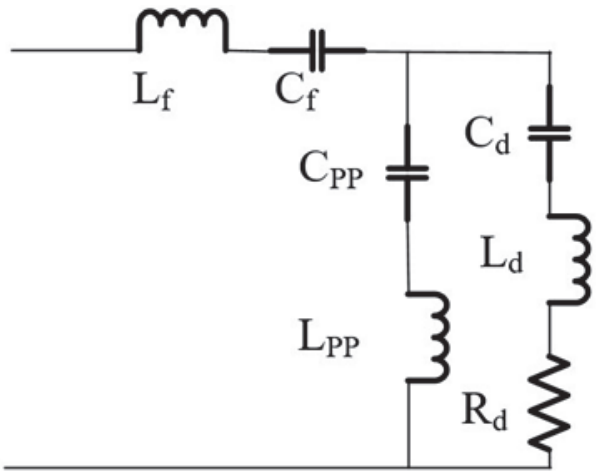

Fig. 3. The equivalent circuit of the dipole unit.

version A (SMA) and radiation patches. The impedance matching circuit of the antenna mainly uses four λ/4 lines to realize impedance transformation, and its formula is as follows:

$$Z_{in} = Z_0 = \frac{Z_1^2}{Z_A}, \tag{1}$$

where Z_{in} is the input impedance, Z_0 is the characteristic impedance of the transmission line, and Z_A is the impedance of the microstrip antenna.

In order to obtain the optimal size for the λ/4 line, the length and width of the λ/4 line are simulated and compared, and the results are shown in Fig. 4. Considering the antenna bandwidth and matching depth, the length of the λ/4 line is 7 mm and the width is 0.25 mm.

Through characteristic mode analysis (CMA) of the planar microstrip structure to accelerate the antenna design cycle. The generalized eigenmode equation is as follows:

$$XJ_n = \lambda_n R_n J_n, \tag{2}$$

where X is the imaginary part of the impedance matrix, J_n is the eigenvector, R_n is the weighted matrix, and λ_n is the solution of the generalized eigenvalue equation $XJ_n = \lambda_n RJ_n$. When $\lambda_n = 0$, the energy stored by the electric field and the magnetic field are equal, and the antenna is in a resonance state. When $\lambda_n < 0$, the energy is concentrated in the electric field, and the corresponding mode of the antenna is the capacitive mode. When $\lambda_n > 0$, the energy is focused on the magnetic field, and the corresponding mode of the antenna is the perceptual mode.

The physical meaning of the characteristic angle in the characteristic mode is the phase difference between the characteristic current and the tangential component

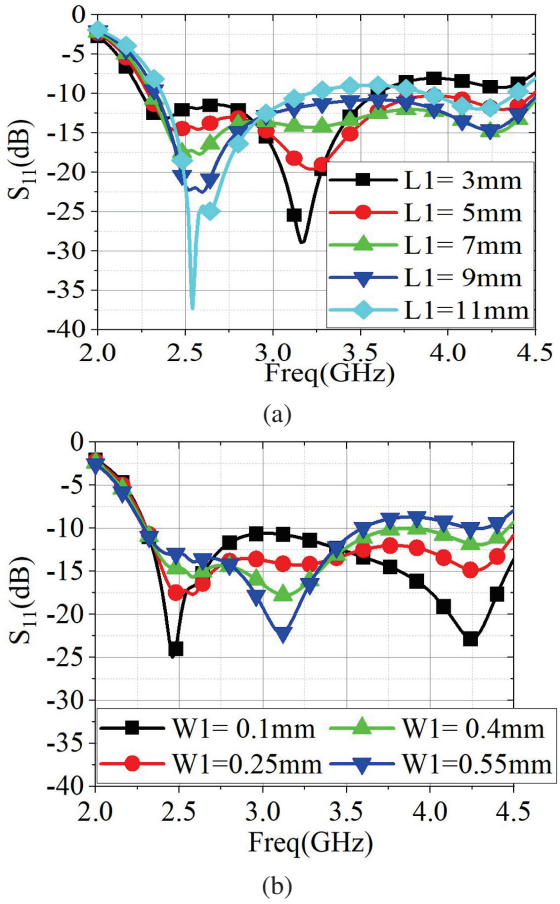

Fig. 4. (a) Simulated effects of varying the λ/4 line length; (b) simulated effects of varying the λ/4 line width.

of the characteristic electric field. The formula is as follows:

$$\beta_n = 180^\circ - \arctan \lambda_n. \tag{3}$$

Since the range of the eigenvalues is (-∞,+∞), the range of the characteristic angle is [90°≤β_n≤270°]. Similarly, the characteristic angle values can be interpreted as follows:

When the eigenvalue is $\lambda_n > 0$, then the range of the eigenvalue angle is $90^\circ < \beta_n < 180^\circ$. The mode is called the inductive mode and stores magnetic energy. When the eigenvalue is $\lambda_n = 0$, then the characteristic angle is $\beta_n = 180^\circ$. The mode is called the resonance mode and the energy radiates outward. When the eigenvalue is $\lambda_n < 0$, the range of the characteristic angle is $180^\circ < \beta_n < 270^\circ$, and the mode is called the capacitive mode, which stores power. When the characteristic angle is 90° or 270°, the mode mainly stores energy and does not radiate outward; that is, it is in an internal resonance state. The phase relationship between modes can be viewed when designing the antenna, so the eigenvalue

parameters are a good guide for the design of circularly polarized or dual-polarized antenna.

The expression for modal significance (MS) is as follows:

$$MS = \left| \frac{1}{1 + j\lambda_n} \right|. \quad (4)$$

The modal significance of the proposed antenna is shown in Fig. 5 (a) and the characteristic angle is shown in Fig. 5 (b). The modal significance of mode 5 exceeds 0.707. Therefore, the omnidirectional property is under the excitation of mode 5. The surface current distribution and the far-field radiation under the excitation of mode 5 are shown in Fig. 6. In order to excite the omnidirectional radiation characteristics and obtain the far-field radiation as shown in Fig. 5 (b), the antenna is excited by an inductive coupling excitation structure (ICE) in the center position.

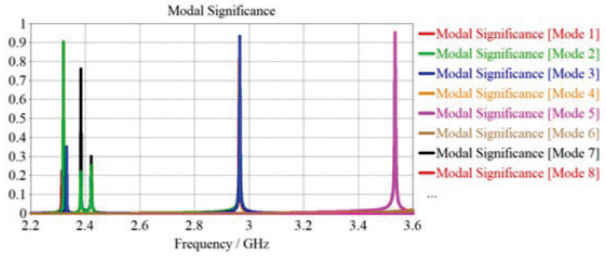

(a)

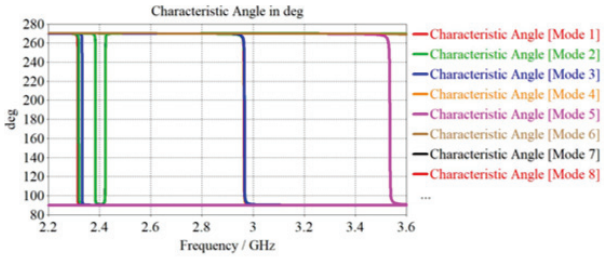

(b)

Fig. 5. Characteristic mode analysis: (a) modal significance; (b) characteristic angle.

Broadband technology is one of the key technologies in the design of microstrip antennas. In [12], a defect-based microstrip antenna design for multi-band applications was proposed, which achieves broadband design by introducing parasitic patches. In [13], the effects of separation and gaps in microstrip patches were verified through antenna design. In this design, the antenna bandwidth was successfully expanded by slotting the fan-shaped parasitic patch. Figure 7 is a comparison of the effects on S11 parameters of the planar omnidirectional antenna with and without the parasitic patches. It can be seen that the introduction of the parasitic patches makes the antenna introduce new resonance points to broaden the reflection coefficient bandwidth of the antenna. The bandwidth of the antenna is increased from 37.6% to 68.6% after the parasitic patch is introduced. In addition, the arm width of the dipole has some influence on the operating frequency band of the antenna. Figure 8 shows the reflection coefficients of a microstrip dipole at different arm widths. It should be noted that, in general, the measured data will deteriorate compared with the simulated data. Therefore, after comparing the reflectivity of dipoles with different arm widths, the 1.6 mm arm widths with higher reflectivity values are selected as the optimal solution for the antenna.

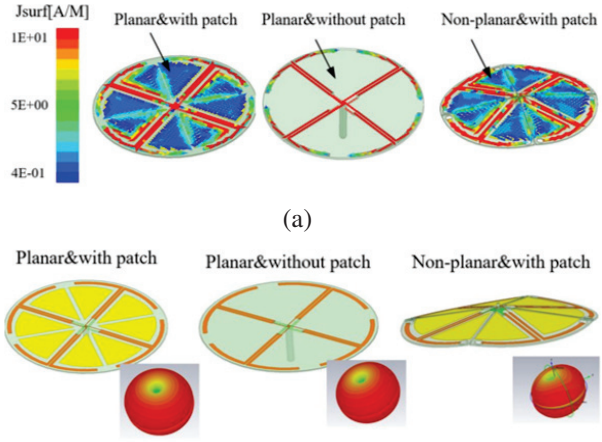

(a)

(b)

Fig. 6. The results of characteristic mode analysis: (a) the surface current distribution; (b) the far-field radiation.

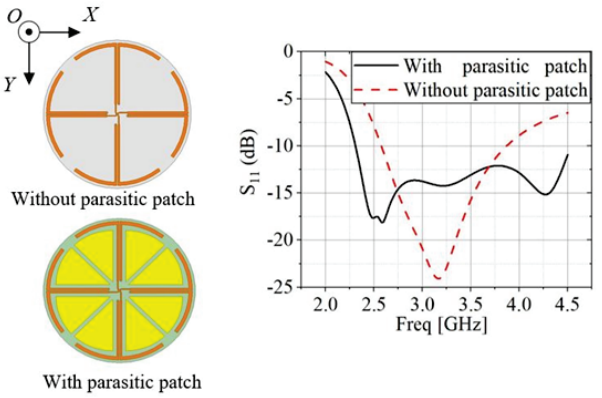

Fig. 7. The effect of parasitic patches on the reflection coefficient of the antenna.

B. Conformal omnidirectional antenna design

The conformal omnidirectional antenna with different pyramid angles will be introduced here. The

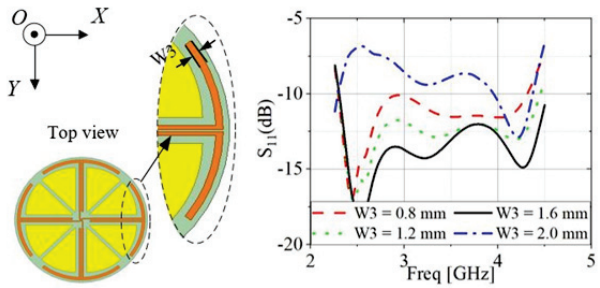

Fig. 8. Simulated effects of varying the arm width of the dipole.

structural diagram of the omnidirectional antenna is shown in Fig. 9. A tube-like structure was used as a carrier for the antenna. This cylinder needs to be hollow in the middle so as to facilitate the soldering of the antenna bottom. It also needs to be perforated in the substrate at a certain height to facilitate the use of a nylon column to fix the conformal antenna. Accordingly, stereolithography appearance (SLA), a 3D printing technology, is used to design the conformal substrate, and epoxy resin with a relative permittivity of 3.5 is selected as the printing material. Polypropylene material with a dielectric constant of 2.2 is used as the fixing bolt in the conformal antenna, which can reduce any interference to the antenna.

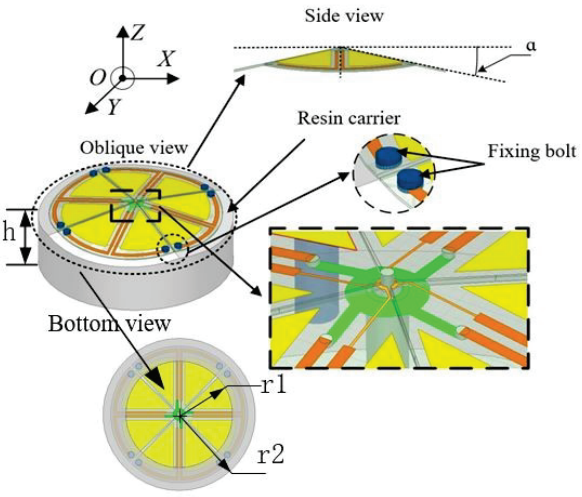

Fig. 9. The structure of the conformal antenna. (h = 18mm, r1 = 28mm, r2 = 35mm).

The simulation results of the reflection coefficient of the omnidirectional antenna under different pyramid angles (α) are shown in Fig. 10 (a). With the pyramid angle increasing from 0° to 15°, the relative bandwidth of the antenna changes from 66% (2.3-4.6 GHz) to 46.7% (2.3-3.7 GHz). When the antenna is conformal to a pyramid with a pyramid angle of 20°, the antenna can achieve a bandwidth of around 26%. The simulation gain and efficiency of the omnidirectional antenna in the working bandwidth are shown in Fig. 10 (b). The maximum simulation gain of the antenna can reach 1dBi, and the gain of the antenna in the whole working bandwidth is more than 0dBi. The simulation efficiency of the antenna with different pyramid angles can reach more than 80% of the effective bandwidth. Figure 11 shows the simulated radiation patterns in E-plane and H-plane at 2 GHz, 2.5 GHz, 3 GHz and 3.5 GHz, respectively. Considering that the working bandwidth of the proposed antenna with the 20° taper is only 26% (2.3-3 GHz), the omnidirectional antenna with a taper of 20° is not simulated and analyzed at 3.5 GHz in Fig. 11. It is clearly seen that the H-plane is omnidirectional from 2 GHz to 3.5 GHz at

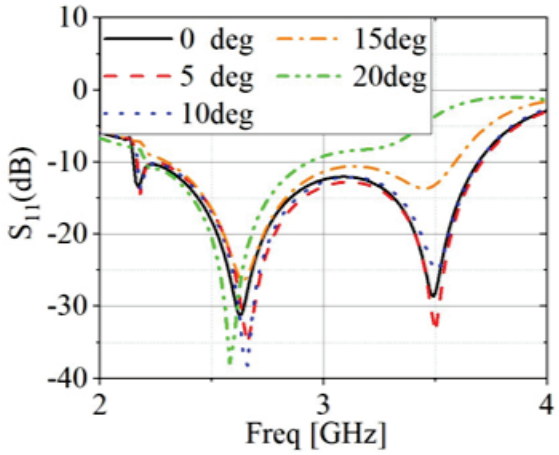

(a)

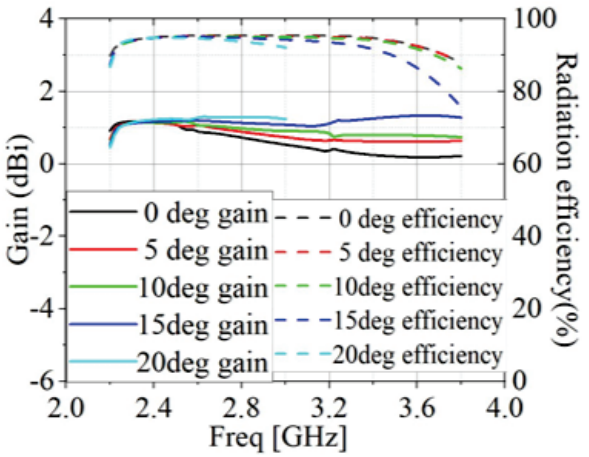

(b)

Fig. 10. The simulated results of the proposed antenna with different pyramid angles: (a) S11 (dB); (b) gain (dBi) and radiation efficiency.

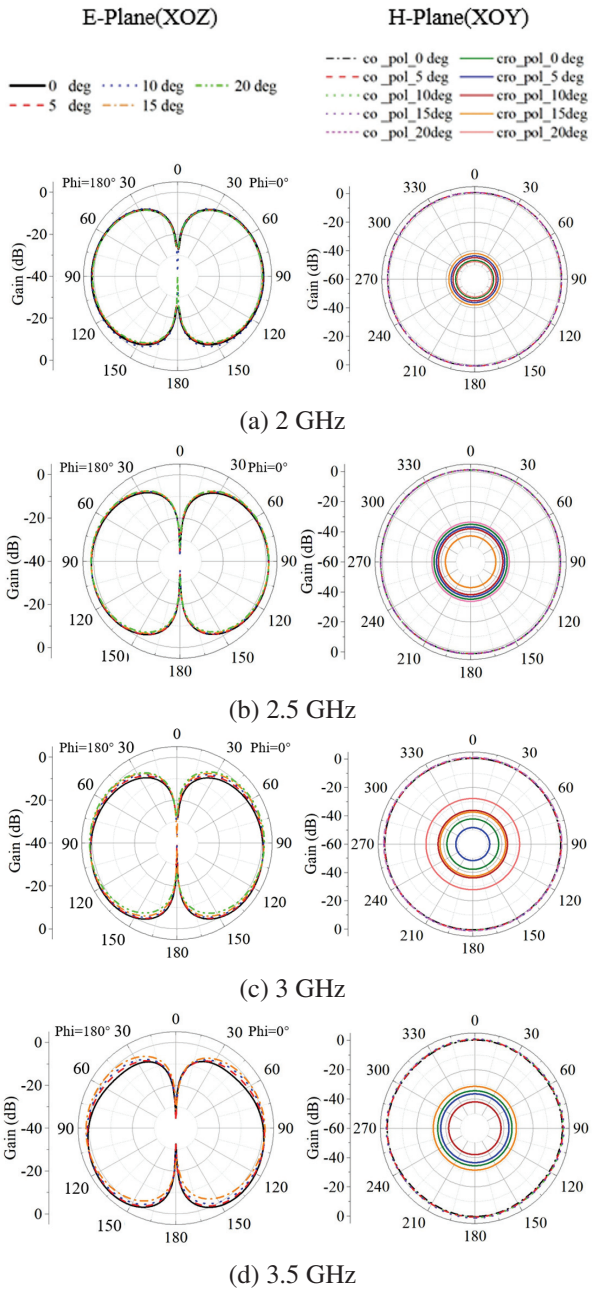

(a) 2 GHz

(b) 2.5 GHz

(c) 3 GHz

(d) 3.5 GHz

Fig. 11. The effect of parasitic patch on radiation patterns of the antenna.

different taper angles. The cross-polarization level in the horizontal plane is less than −41 dB, respectively. Moreover, in the operating bandwidth, the simulated gain variations for the four taper angles are no more than 1.5 dBi, respectively.

III. EXPERIMENTAL RESULTS

The simulated and measured results of the proposed antenna will be introduced in this section. To verify the feasibility of the proposed conformal omnidirectional antenna, a prototype with $\alpha = 10^{\circ}$ is manufactured. The photographs of the fabricated antenna and measured environment are displayed in Fig. 12.

The simulated and measured reflection coefficient is shown in Fig. 13. The measured relative bandwidth of the antenna is 44.36% (2.28 GHz-3.58 GHz), which is slightly narrower than the simulated one (51.2%) due to the errors caused by fabrication and assembly tolerances. Additionally, the simulated and measured gain is shown in Fig. 14. The result shows that the simulation and test results of the gain are highly consistent. To fix the SMA to the bottom of the antenna, a fixing glue is applied to the welding point on the antenna bottom.

The simulated and measured radiation patterns of the prototype at 2, 2.5, 3, and 3.5 GHz are shown in Fig. 15. It is observed that the antenna can achieve omnidirectional radiation characteristics with the maximum gain variation of 2.2 dBi in the operating frequency range. The main polarization radiation peak gain of the antenna achieves 1 dBi and the cross-polarized gain in the bandwidth is lower than −28 dB.

Table 2 is a chart comparing the proposed work with previous works. Antennae proposed in [3, 5, 6] can achieve omnidirectional radiation characteristics, but antennae with conformal structure and omnidirectional radiation characteristics have difficulty achieving wide operating bandwidth. To expand bandwidth, an antenna conformal to a hemispherical structure is proposed in [11]. However, this antenna cannot achieve omnidirectional radiation and, moreover, the structure of the antenna is complex with significant processing

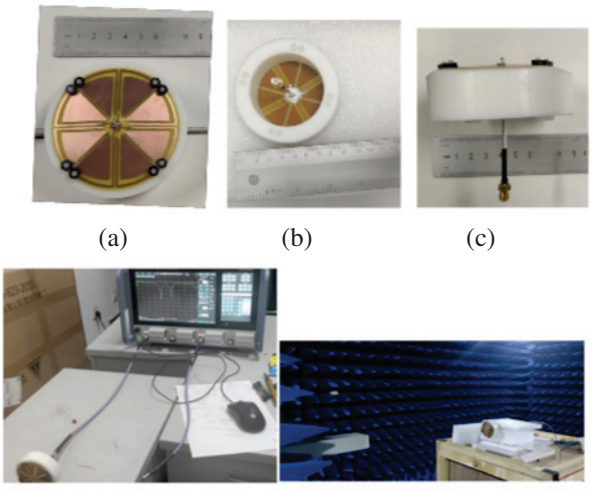

(a) (b) (c)

(d)

Fig. 12. The photos of the proposed antenna: (a) top view; (b) bottom view; (c) side view; (d) measured environment.

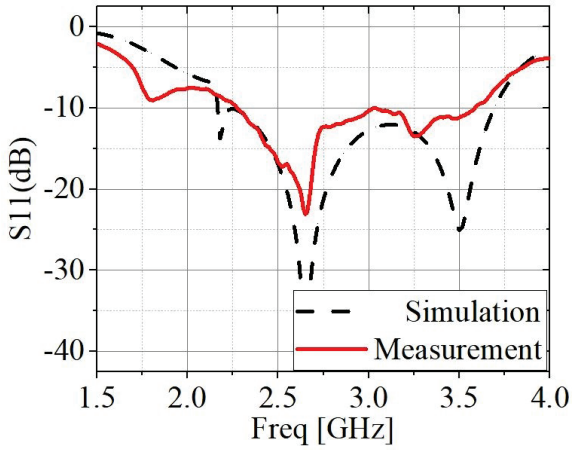

Fig. 13. Simulated and measured results of S11.

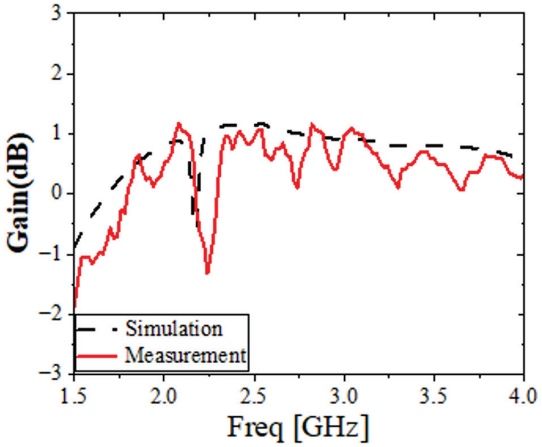

Fig. 14. Simulated and measured gain of the proposed antenna.

Table 2: Comparison between the proposed and previously reported antennae

Ref.	Size(λ^3)	Radiation Structure	Radiation Direction	BW	Gain (dBi)
[3]	0.143× 0.092× 0.016	conformal	omnidirectional	6.3%	0.5
[5]	0.8× 0.53× 0.042	planar	omnidirectional	1.5%	1.4
[6]	-	conformal	omnidirectional	28%	−2.6
[10]	0.58× 0.58× 0.00092	conformal	omnidirectional	-	2.1
[11]	0.52× 0.52× 0.15	conformal	unidirectional	55.8%	5.8
Prop	0.53× 0.53× 0.1	conformal	omnidirectional	44.4%	1

*BW(%):Bandwidth

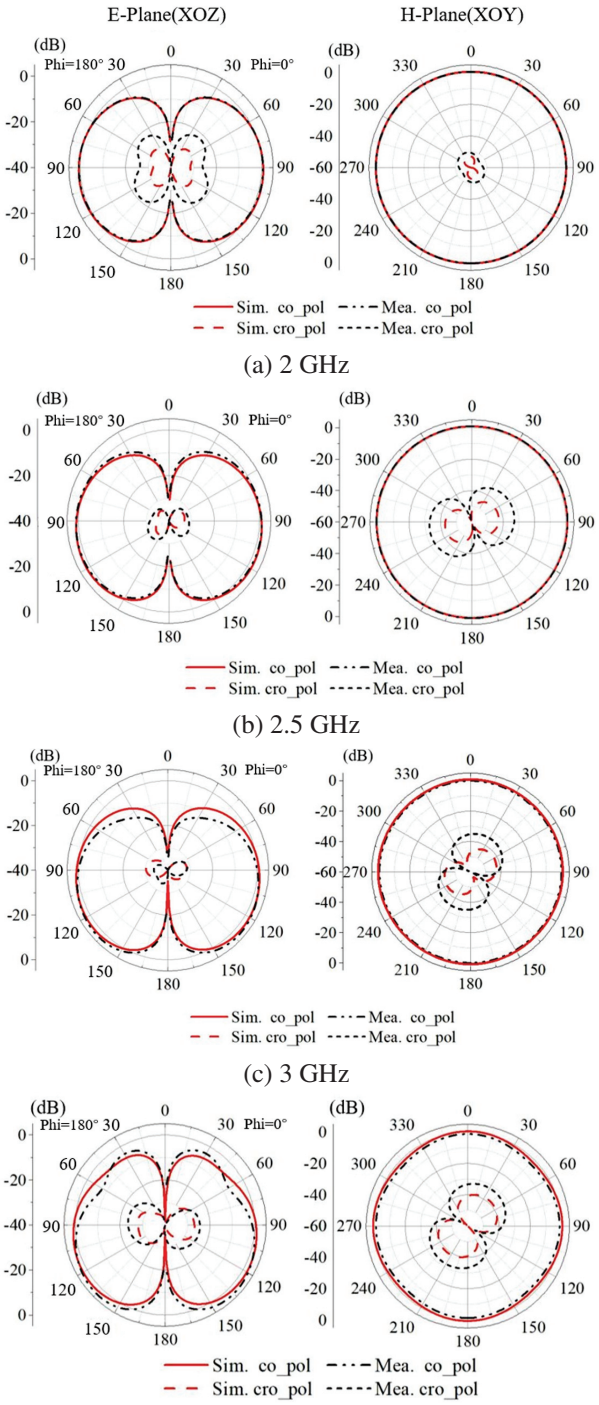

(a) 2 GHz

(b) 2.5 GHz

(c) 3 GHz

(d) 3.5 GHz

Fig. 15. Simulated and measured results of radiation patterns.

and fabrication requirements. Based on a conformal structure, a wideband quadrangular pyramid conformal printed dipole antenna has been designed with the aim of achieving good omnidirectional radiation characteristics in the working frequency band.

IV. CONCLUSION

In this paper, an omnidirectional antenna with a wideband was designed and fabricated. Omnidirectional radiation was realized by exciting four microstrip dipoles with different radiation directions. The dipole units effectively improved the resonance effect of the antenna by introducing parasitic patches. Based on the planar omnidirectional antenna, the radiation characteristics of the omnidirectional antenna at different pyramid angles from 0° to 20° were explored. The measurement results of the prototype with a pyramid angle of 10° were consistent with the simulation ones. High efficiency and small gain variation were obtained in the S-band of 44.36% from 2.28-3.58 Ghz. The proposed antenna is therefore considered to be a good candidate for high-efficiency omnidirectional communications applications.

ACKNOWLEDGMENT

We would like to thank the following for their support: the open research fund of National Mobile Communications Research Laboratory, Southeast University (No. 2023D05, Enterprise entrusted project (W2021JSKF0153, W2020JSFW0112), HeFei University of Technology teacher program (JZ2019HGTB0093), An-hui Natural Science Foundation (2208085MF161), and the Fundamental Research Funds for the Central Universities (JZ2021HGTA0144).

REFERENCES

[1] K. A. Yinusa, "A dual-band conformal antenna for GNSS applications in small cylindrical structures," *IEEE Antennas Wirel. Propag. Lett*., vol. 17, no. 6, pp. 1056-1059, Apr. 2018.

[2] H. Y. Liang, H. C. Yang, and J. Zhang, "A cylindrical conformal directional monopole antenna for borehole radar application," *IEEE Antennas Wirel. Propag. Lett*., vol. 11, pp. 1525-1528, Dec. 2012.

[3] J. H. Bang, W. J. Kim, and B. C. Ahn, "Two-element conformal antenna for multi-GNSS reception," *IEEE Antennas Wirel. Propag. Lett*., vol. 16, pp. 796-799, Aug. 2017.

[4] D. Psychoudakis and J. L. Volakis, "Conformal asymmetric meandered flare (AMF) antenna for body-worn applications," *IEEE Antennas Wirel. Propag. Lett*., vol. 8, pp. 931-934, July 2009.

[5] H. Nawaz, X. Liang, M. S. Sadiq, and M. A. B. Abbasi, "Ruggedized surface-mount omnidirectional antenna for supersonic aerial platforms," *IEEE Antennas Wirel. Propag. Lett*., vol. 19, no. 8, pp. 1439-1442, June 2020.

[6] G. Byun, C. Seo, B. J. Jang, and H. Choo, "Design of aircraft on-glass antennas using a coupled feed structure," *IEEE Trans. Antennas Propag*., vol. 60, no. 4, pp. 2088-2093, Jan. 2012.

[7] B. Feng, K. L. Chung, J. Lai, and Q. Zeng, "A conformal magneto-electric dipole antenna with wide H-plane and band-notch radiation characteristics for sub-6-GHz 5G base-station," *IEEE Access*, vol. 7, pp. 17469-17479, Feb. 2019.

[8] W. Lei and Y.-X. Guo, "Design of a dual-polarized wideband conformal loop antenna for capsule endoscopy systems," *IEEE Trans. Antennas Propag*., vol. 66, no. 11, pp. 5706-5715, Nov. 2018.

[9] H. Yang, X. Liu, and Y. Fan, "Design of broadband circularly polarized all-textile antenna and its conformal array for wearable devices," *IEEE Trans. Antennas Propag*., vol. 70, no. 1, pp. 209-220, Jan. 2022.

[10] S. Ahmed, F. A. Tahir, A. Shamim, and H. M. Cheema, "A compact Kapton-based inkjet-printed multiband antenna for flexible wireless devices," *IEEE Antennas Wirel. Propag. Lett*., vol. 14, pp. 1802-1805, Apr. 2015.

[11] Y.-D. Yan, Y.-C. Jiao, C. Zhang, Y.-X. Zhang, and G.-T. Chen, "Hemispheric conformal wide beamwidth circularly polarized antenna based on two pairs of curved orthogonal dipoles in space," *IEEE Trans. Antennas Propag*., vol. 69, no. 11, pp. 7900-7905, Nov. 2021.

[12] F. F. Ismail, M. A. El-Aasser, and N. H. Gad, "A parasitic hat for microstrip antenna design based on defected structures for multiband applications," *The Applied Computational Electromagnetics Society* (*ACES*) *Journal*, vol. 37, no. 5, pp. 568-575, May 2022.

[13] N. H. Gad and M. Vidmar, "Design of a microstrip-fed printed-slot antenna using defected ground structures for multiband applications," *The Applied Computational Electromagnetics Society* (*ACES*) *Journal*, vol. 33, no. 8, pp. 854-860, July 2021.

Zhaoneng Jiang was born in Xuancheng, China. He received the Ph.D. degree from Nanjing University of Science and Technology, Nanjing, China, in 2012. He has been working on numerical methods of computational electromagnetism since 2013. He is currently a Professor at the Hefei University of Technology, Hefei, China. He has authored or coauthored more than 90 papers in refereed international conferences and journals, and has served as Program Committee Member in several international conferences. His current focus is on antenna and microwave devices. (E-mail: jiangzhaoneng@hfut.edu.cn)

Yongxin Sha was born in Anhui, China, in 1996. He is currently working towards the M.E. degree in Electronic Science and Applied Physics at Hefei University of Technology, Hefei, China. He is currently focusing on antenna and microwave device design. (E-mail: 921937992@qq.com)

Xiaofeng Xuan was born in Anhui, China, in 1975. He received the M.S. degree from Nanjing University, China. His current focus is on numerical methods of computational electromagnetism. (E-mail:941067868@qq.com)

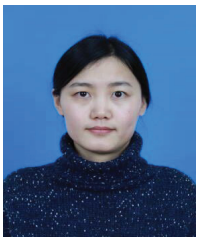

Liying Nie (corresponding author) was born in Shandong, China, in 1990. She received the Ph.D. degree from the University of Electronic Science and Technology of China. Her research focus is on the theory and design of microwave and millimeter wave antennae. (E-mail: liyingnie@sina.com)

A Differential Slot-type Dual-polarization Ultra-wideband Antenna

Zhao Neng Jiang[1,2], Zhi Xin Wang[1], Xiao Feng Xuan[1], Li Ying Nie[1], and Ye Jiang[1]

[1]Department of Information Engineering
Hefei University of Technology, Hefei, 230009, China

[2]National Mobile Communications Research Laboratory
Southeast University, Jiangsu, 210096, China
liyingnie@sina.com

Abstract – A differentially fed dual-polarization slotted antenna with an ultra-wide bandwidth and low cross polarization is presented in this paper. The antenna is composed of a radiation patch and a ground plane, both of which are printed on the top of the dielectric substrate. The ground is extended toward the radiation patch to form a slotted coplanar structure. In order to expand the bandwidth, a cross-shape symmetrical slotted structure is loaded into the radiation patch. Differential feed is adopted to realize 0°/90° linear polarizations and suppress the cross polarization. Simulation and measurement results show that the proposed antenna with dimensions of $0.53\lambda_0 \times 0.53\lambda_0 \times 0.0135\lambda_0$ (λ_0 is the wavelength at 4 GHz) has a differential mode impedance bandwidth of 82.25% (2.27-5.56 GHz), a differential feed port isolation of higher than 28 dB, and a cross polarization level of less than −30 dB, which achieves the characteristics of ultra-wideband, high isolation, and low cross polarization level.

Index Terms – coplanar waveguide, differential feed, dual polarization, low-profile, ultra-wideband.

I. INTRODUCTION

With the development of wireless technology in the fields of personal communication and military applications, people have higher and higher requirements for the design of communication system antennas under the limited spectrum resources [1]. In order to reduce the influence of multipath effect and increase the channel capacity of the system, dual-polarization antenna arises at the right moment [2]. Moreover, dual-polarization antenna can be broadband, compatible with a variety of communication standards or support high-speed data transmission, so as to reduce the demand for the number of antennas in a certain operating frequency band. It can also be miniaturized to reduce the carrier space occupation and easy to integrate with the carrier [3–5].

In the implementation of dual-polarization, two independent ports are usually adopted to feed the cross dipole antenna in order to obtain vertical and horizontal polarization modes [6]. Traditional dual-polarization cross-dipole antennas have narrow operating bandwidth and high profile [7–10]. For example, a dual-polarization cross-slotted antenna with two orthogonal groove radiators was designed in [11]. To reduce the antenna size, a small ground was designed with the same length of the hypotenuse as the slot, and inductors were loaded at both ends of the slot. The common impedance bandwidth of the dual-polarization antenna at port 1 and port 2 is 1.56 - 2.73 GHz (54.5%), the isolation is greater than 26 dB, and the profile height is about $0.27\lambda_0$. In [12], a pair of orthogonally-printed dipoles and a reflective ground were used to obtain two linear polarizations. A slot in the center of the dipoles and short connection between the orthogonally-printed dipoles could improve the isolation and cross polarization. The antenna has a cross-polarization of < -30 dB, a port isolation of $>$ 35 dB, and a profile height of $0.15\lambda_{575\text{MHz}}$ within 575 - 722 MHz (22.7%). The antennas described in [11, 12] have complex structure, relatively small bandwidth and a high profile, which makes them difficult to integrate with microwave circuits. In [13], a reflection plate was designed based on the in-phase reflection principle of artificial magnetic conductor (AMC) structure, so that the height of the dual-polarization antenna was reduced by half, and the antenna worked within 1.67 - 2.98 GHz (56%). Although the antenna profile height is reduced, the loading of AMC also makes the antenna structure more complex.

However, a microstrip antenna can obtain two orthogonal polarization modes by feeding different patches on the same dielectric layer or radiation patches on different dielectric layers. The operating frequency band of microstrip antenna can be expanded by adding parasitic elements, etching slots and so on. A dual-polarization planar slotted antenna is proposed in [14], which adopts

Submitted On: July 21, 2021
Accepted On: October 25, 2021

https://doi.org/10.13052/2023.ACES.J.380305

different feeding mechanisms of high isolation ports to achieve two kinds of orthogonal polarization. Horizontal polarization is excited by a curved line coupling slot and vertical polarization is fed by a stepped monopole. In [15], a compact dual-polarization slotted antenna is presented, which uses triple-mode stepped slotted-line resonator and dual-mode criss-cross monopole. Through feeding two ports symmetrically at the opposite positions of the slot to achieve orthogonal polarization, the antenna can achieve a wide operating frequency band (1.63 - 2.93 GHz) and a high port isolation (> 32 dB). The antenna described in [14, 15] uses microstrip antenna to achieve dual-polarization, which results in a low-profile height, but the cross-polarization level is not high enough, and the operating bandwidth is still not large enough.

Targeting the deficiencies of narrow bandwidth and poor polarization purity of traditional planar microstrip slotted antenna, a compact ultra-wideband dual-polarization slotted antenna with low cross polarization is proposed in this paper. It consists of a symmetrical radiation patch and a ground plane which form a gap in the upper layer of the dielectric plate. The antenna adopts coplanar waveguide (CPW) structure for differential feed. Differential feed is to feed two ports of the antenna at the same time through two signal lines. The signals fed through these two ports have the characteristics of equal amplitude and reverse phase, so it is also called inverting feed technology. The inverting feed technology can suppress the high-order modes generated on the metal radiation patch. It can counteract the coupling between the same pair of feed probes and the radiation leakage between them, so that the antenna cross polarization can be suppressed and the isolation between the ports can be improved [16]. To further expand the antenna bandwidth, a cross-shape slot is loaded in the center of the radiation patch. Simulation and experimental results show that the overall antenna size is 40 mm × 40 mm × 1.016 mm, the impedance bandwidth can reach 82.25% (2.27 - 5.56 GHz), the port isolation is higher than 28 dB, and the cross-polarization level is less than −30 dB. It can meet the requirements of miniaturization, ultra-wide bandwidth, high isolation, and low cross polarization.

II. ANTENNA DESIGN

A. Antenna structure

Figure 1 shows the geometry of the dual-polarization antenna. The radiator and ground are printed on a 1.016 mm-thickness Rogers 5880 substrate with a relative dielectric constant of 2.2 and a loss tangent of 0.009. The radiation patch is a symmetrical structure composed of four semicircles with a radius of R and two rectangles with a width of k and a length of twice j. To expand the impedance matching bandwidth, a cross-shape slot with a width of m and a length of twice l is loaded in the center. The end sides of the semicircle are feeder parts with a width of p. The antenna is fed by coplanar waveguide (CPW). The ground extends toward the radiation patch, and an s-width gap is formed. According to the design principle of microstrip antenna, the patch width L can be expressed as:

$$L = \frac{c}{2f_r}\left(\frac{\varepsilon_r+1}{2}\right)^{-\frac{1}{2}}, \tag{1}$$

where f_r is the resonant frequency, c is the speed of light, and ε_r is the dielectric constant of the substrate. According to equation (1), the width of the patch can be roughly calculated to be at least 30 mm, so $R + j$ should be greater than 15 mm. The design parameters of the final structure are as follows: W = 40 mm, R = 6 mm, k = 4 mm, j = 11 mm, p = 2.4 mm, m = 3 mm, l = 9.5 mm, s = 0.5 mm.

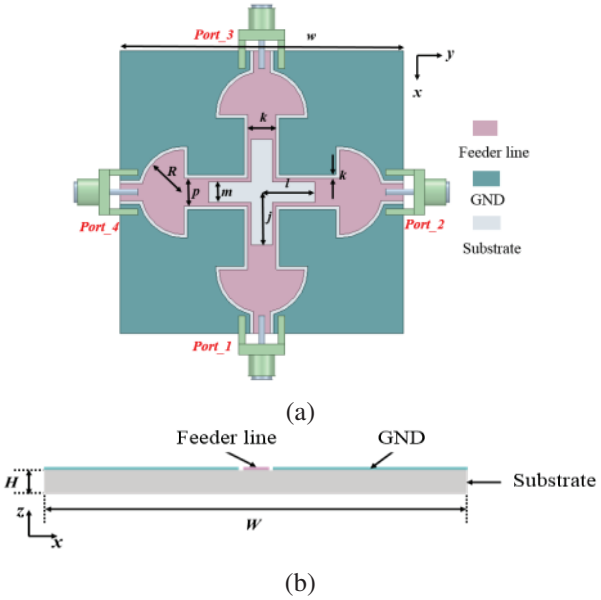

Fig. 1. Geometry of the proposed antenna. (a) Top view. (b) Front view.

The four feed ports of the antenna are shown in Fig. 1. Differential feed port 1 is formed when port_1 and port_3 feed the signal of equal amplitude and reverse phase at the same time, and the antenna will generate vertical polarization mode. When port_2 and port_4 feed equal amplitude and reverse phase signals at the same time, the differential feed port_2 is formed, and the antenna will generate horizontal polarization mode.

B. Design process

The design process of the dual-polarization antenna is shown in Fig. 2. Ant1 is a unipolar CPW differential dual-polarization antenna, Ant2 is a slotted

CPW differential dual-polarization antenna, and Ant3 is a cross-slotted CPW differential dual-polarization antenna. It should be noted that all the three antennas in Fig. 2 have the same dimensions and the same substrate as the antenna in Fig. 1. Compared with Ant1, the ground in Ant2 is extended toward the patch direction so that the current distribution area increases and radiates with the patch, thus widening the antenna bandwidth. To obtain better impedance-matching characteristics, cross-shape slots are loaded in Ant3. Due to the symmetrical structure of these antennas, the horizontal and vertical polarization performances are basically the same. Figure 3 shows the simulation results of the three antennas in the case of vertical polarization.

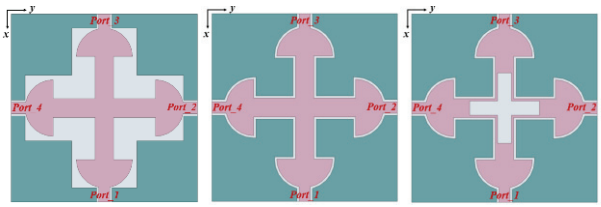

(a) (b) (c)

Fig. 2. Antenna design process. (a) Ant1. (b) Ant2. (c) Ant3.

The bandwidth of a traditional planar microstrip slotted antenna is narrow. By increasing the height of the dielectric plate and reducing the dielectric constant of the dielectric plate to improve the impedance bandwidth of the antenna, it may bring some problems such as stray loss, decrease of antenna efficiency, and distortion of the pattern. Therefore, Ant2 extends the ground towards the direction of the radiation patch on the basis of Ant1. This improvement can increase the current distribution area and generate a certain radiation effect, thus improving the impedance bandwidth and dual-polarization performance. To obtain better impedance matching, a cross-shape structure is etched in the center of the radiation patch to form Ant3. The loading of the cross-shape slot is equivalent to adding a series inductor to the circuit, and a new slot capacitance is created between the ground and the radiation patch. A new resonance is thus formed around the main resonance, promoting the formation of multiple resonances and effectively widening the bandwidth. Due to the cross-shape gap being a symmetrical structure, the interference to radiation pattern is small.

It can be seen from Fig. 3 that the impedance bandwidth of Ant3 is obviously better than that of the other two antennas. All three antennas have good port isolation, which is greater than 22 dB. However, Ant3 has lower port isolation and better performance compared

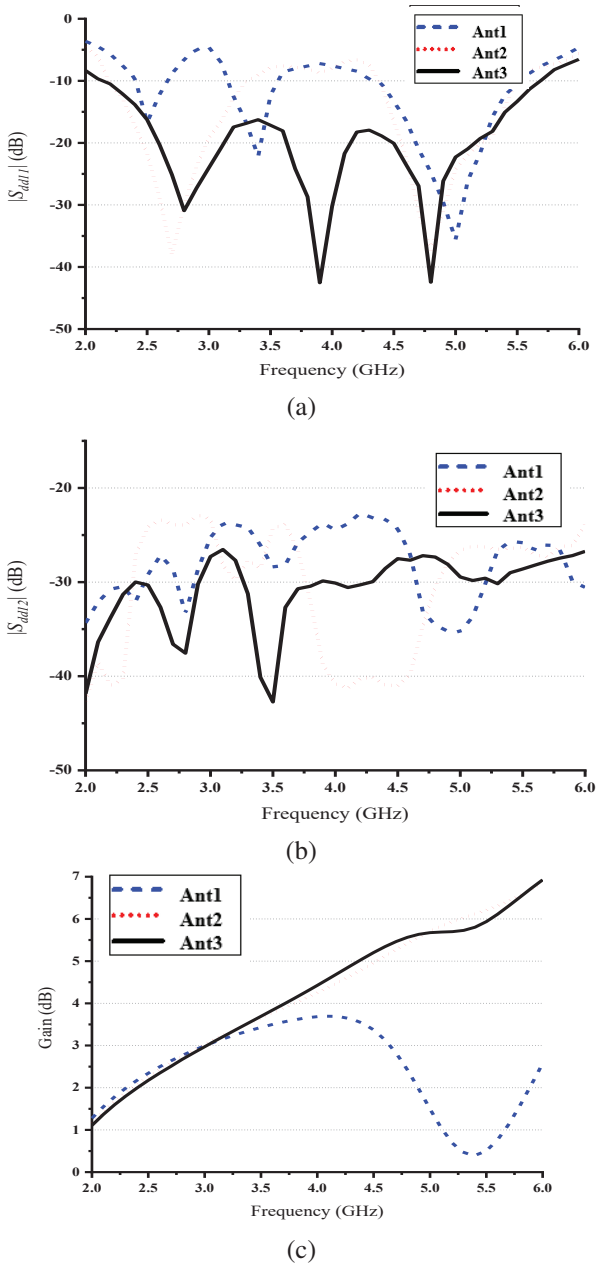

Fig. 3. Simulation results of three kinds of antennas. (a) $|S_{dd11}|$. (b) $|S_{dd12}|$. (c) Gain.

with the other two antennas. In Fig. 3 (c), the gain of Ant2 and Ant3 at high frequency is significantly higher than that of Ant1. Compared with the other two antennas, Ant3 has wider operating bandwidth, relatively higher gain and port isolation, which is the optimal antenna structure. The comparison of impedance bandwidths, isolation and peak gain variations of Ants 1-3 is listed in Table 1.

Figure 4 shows the surface current distribution of Ant3 operating at 2.3 GHz, 4.0 GHz, and 5.4 GHz. When

Table 1: Comparison of Ants 1-3

Antenna	Bandwidth	Isolation (dB)	Peak Gain (dB)
Ant1	4.31 - 5.54 GHz	>22	3.72
Ant2	4.38 - 5.53 GHz	>22	6.77
Ant3	2.27 - 5.56 GHz (82.25%)	>28	6.86

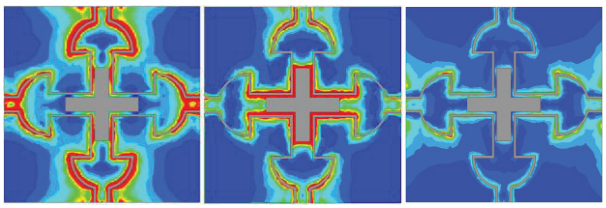

(a) (b) (c)

Fig. 4. Surface current distribution of Ant3 at different frequencies. (a) 2.3 GHz. (b) 4.0 GHz. (c) 5.4 GHz.

the antenna operates at 2.3 GHz, the current mainly concentrates at the edge of the semicircle radiation patch and the ground slot. At 4.0 GHz, the current mainly concentrates at the edge cross-shape slot, resulting in a new resonance point. At 5.4 GHz, the current mainly concentrates at the gap edge between the radiation patch and the ground. The length of the cross-shape slot is 76 mm, and the electric length is about $0.5\lambda_0$ (λ_0 is the wavelength at 4 GHz), which meets the condition of half wave slot, indicating that the slot works in the middle frequency band and can produce effective radiation.

C. Principle of dual-polarization generation

The antenna is excited by two pairs of differential ports through four SMA heads to generate and radiate vertically-polarized and horizontally-polarized waves. In order to verify the generation principle of dual polarization, Fig. 5 shows the vector current distribution of the antenna fed by different ports at 4 GHz. When port_1 and port_3 feed signals with equal amplitude and phase difference of 180°, port_2 and port_4 are connected with 50 Ω load. It can be seen from Fig. 5 (a) that when the electric fields of the patch in the Y direction cancel each other, leaving only the electric field in the X direction, then the antenna will generate and radiate the vertically-polarized wave. Similarly, when port_2 and port_4 feed signals with equal amplitude and phase difference of 180°, port_1 and port_3 are connected with 50 Ω load. It can be seen from Fig. 5 (b) that when the electric fields in the X direction of the patch cancel each other, leaving only the electric field in the Y direction, then the antenna will generate and radiate horizontally-polarized waves.

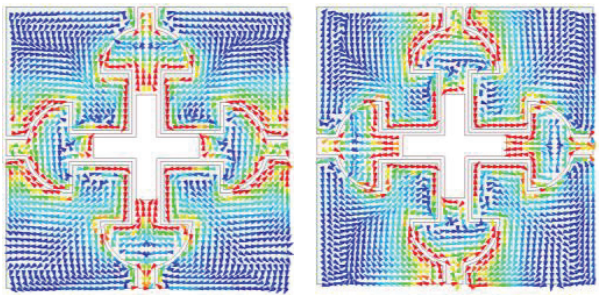

(a) (b)

Fig. 5. Surface vector current distribution of Ant3 at 4.0 GHz. (a) Exciting Port_1 and Port_3. (b) Exciting Port_2 and Port_4.

III. NUMERICAL RESULTS

A. Parameter analysis

According to the structure design, the size of the semicircular and the rectangular patch, the width of the feeder line, and the gap width between the ground and the patch will affect the performance of the antenna. It is therefore helpful to select the optimal size parameters for best performances by analyzing the influences of the key parameters on the performances of the antenna.

The effects of different variables on antenna performance are shown in Fig. 6. Assuming that other parameters remain unchanged, the relationship between radius R and antenna performance is analyzed in Fig. 6 (a). With the increase of R, the impedance bandwidth increases continuously. Due to the limitation of the overall size of the antenna, Rchooses 6 mm as the best size. It can be seen from Fig. 6 (b) that as parameter k decreases continuously, the better the impedance- matching effect of mid-frequency part is, and the better the combination effect of multiple resonant modes is. When p = 1.6 mm, the resonant point of the antenna shifts to the low frequency part, which leads to poor matching of the high frequency part. When p = 3.2 mm, the spacing between the three resonant points becomes smaller, and the bandwidth of differential mode impedance matching becomes narrower. When p = 2.4 mm, the antenna gets the widest impedance-matching bandwidth. As the gap width s increases, multiple resonant points obviously move towards high frequency, which will lead to the poor matching effect of the antenna at low frequency. Considering the frequency band that the antenna needs to work, s = 0.5 mm is finally selected as the optimal value.

B. Simulated and experimental results

Figure 7 shows the fabricated antenna and the comparison of measured and simulated differential mode S parameters in two polarization modes. The vector

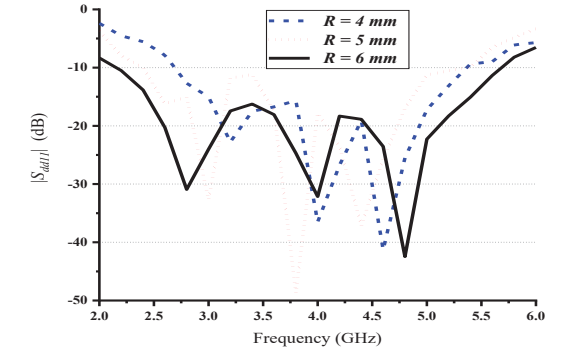

(a)

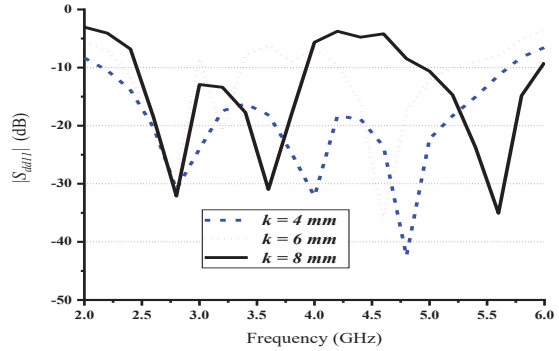

(b)

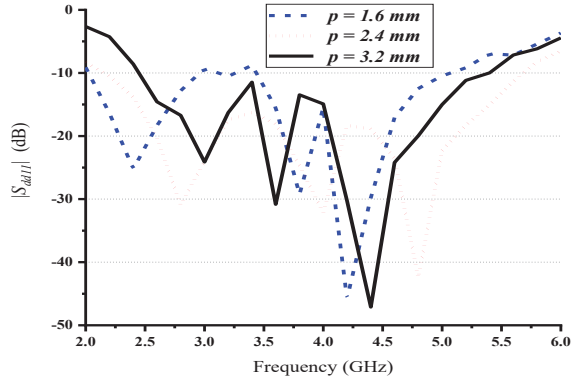

(c)

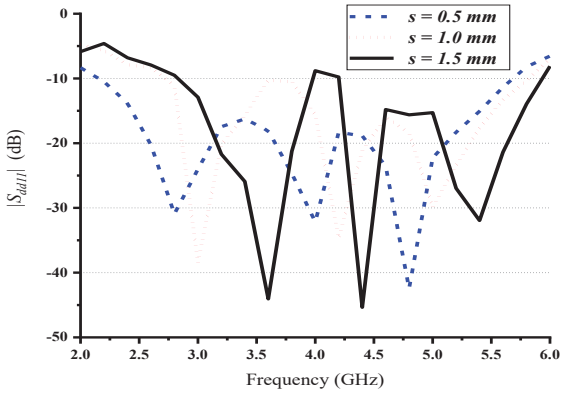

(d)

Fig. 6. Parameter study of $|S_{dd11}|$ with different dimensions as the parameter: (a) *R*. (b) *k*. (c) *p*. (d) *s*.

network analyzer Agilent is employed to measure the S-parameters. It can be seen from Fig. 7 (b) that the differential mode impedance bandwidth of the antenna is 2.27-5.56GHz, and the relative bandwidth is 82.25%. In this frequency band, the isolation of the differential port is higher than 28 dB as shown in Fig. 7 (c). The discrepancies between simulated and measured results may be due to fabrication tolerances, imperfect soldering, and measurement tolerances.

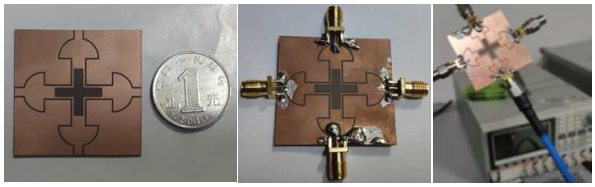

(a)

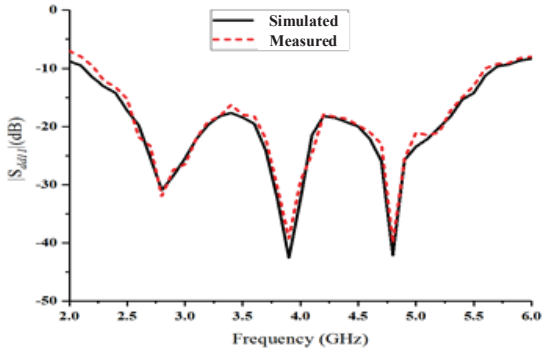

(b)

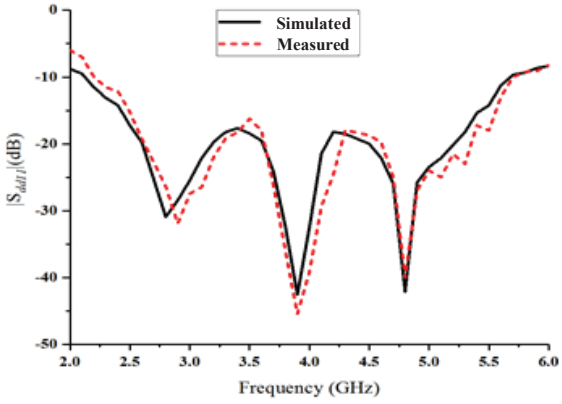

(c)

Fig. 7. Comparison of simulation and measured results. (a) Fabricated antenna. (b) Vertical polarization. (c) Horizontal polarization.

Figures 8 and 9 depict the simulated and measured radiation patterns of the proposed antenna in vertical and horizontal polarization at 2.3 GHz, 4.0 GHz, and 5.4 GHz, showing good agreement with each other. It can be seen that the cross polarization level of the antenna is extremely low within the working bandwidth, which is less than − 30 dB. It has a stable radiation pattern and

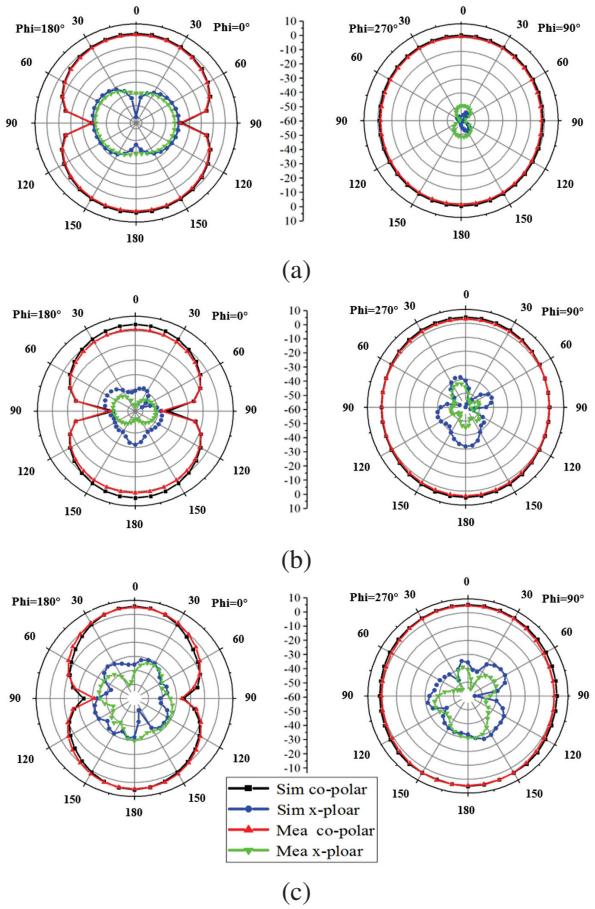

Fig. 8. Simulated and measured radiation patterns in vertical. (a) xoz and yoz plane at 2.3 GHz. (b) xoz and yoz plane at 4.0 GHz. (c) xoz and yoz plane at 5.4 GHz.

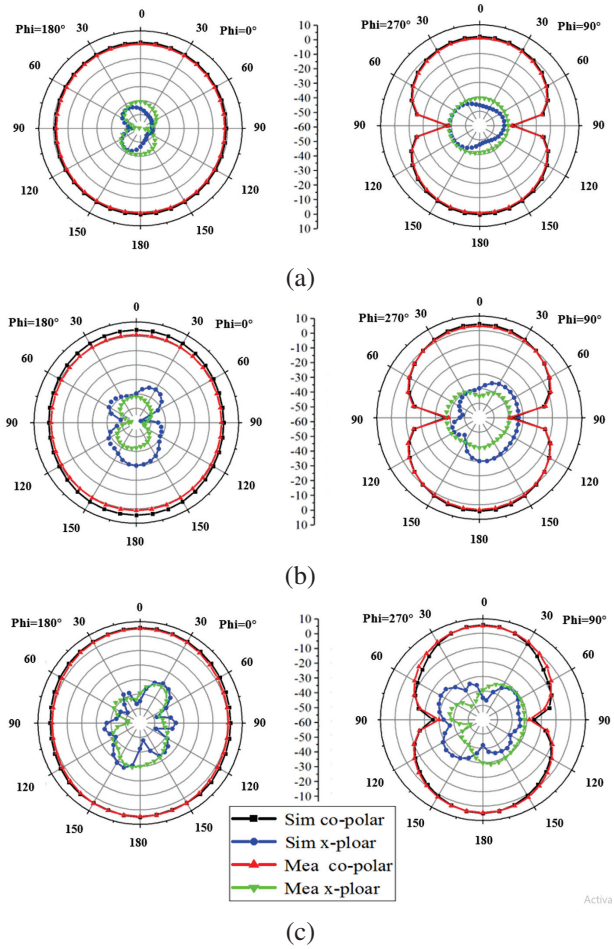

Fig. 9. Simulated and measured radiation patterns in horizontal. (a) xoz and yoz plane at 2.3 GHz. (b) xoz and yoz plane at 4.0 GHz. (c) xoz and yoz plane at 5.4 GHz.

an extremely low cross polarization level. However, with the increase of frequency, the polarization isolation decreases slightly.

As the designed antenna is a dual polarization antenna, the following formula is used to calculate the radiation efficiency.

$$\text{Radiation Efficiency} = \frac{\text{Radiated Power}}{\text{Incident Power}}, \qquad (2)$$

where radiated power and incident power are directly simulated by HFSS software. The simulated radiation efficiency and gain are shown in Fig. 10, where one sees that the radiation efficiency is better than 70% over the working bandwidth. As can be seen from Fig. 10, the gain is linearly increasing over the entire band, the average gain of the antenna in both polarization modes is 4.27 dB, and the maximum gain is 6.86 dB, but the gain of the low-frequency part is slightly lower.

Table 2 shows the performance comparison between the antenna proposed in this paper and the antenna in the cited literature. The results show that the antenna has

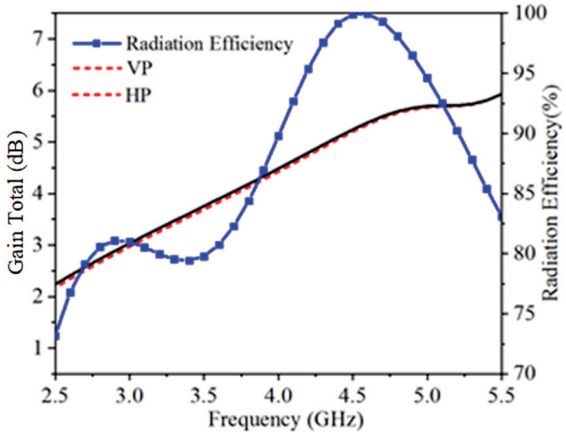

Fig. 10. Simulated radiation efficiency and gain.

a wider impedance bandwidth, a smaller relative size, a higher isolation, and a lower cross-polarization level.

Table 2: Comparison of the proposed antenna with some existing works

Ref.	Dimension	Common Bandwidth	Isolation (dB)	Cross-polarization (dB)
[11]	$0.82\lambda_0 \times 0.82\lambda_0 \times 0.27\lambda_0$		> 26	< -25
[12]	$0.46\lambda_0 \times 0.46\lambda_0 \times 0.17\lambda_0$	$0.575 - 0.722$GHz (22.7%)	> 35	< -30
[13]	$1.1\lambda_0 \times 1.39\lambda_0 \times 0.13\lambda_0$	$1.67 - 2.98$GHz(56%)	> 25	< -20
[14]	$1.23\lambda_0 \times 1.23\lambda_0 \times 0.0075\lambda_0$	$1.70 - 2.71$GHz(45.8%)	> 33	< -20
[15]	$0.49\lambda_0 \times 0.71\lambda_0 \times 0.0034\lambda_0$	$1.63 - 2.93$GHz (57%)	> 32	< -15
This paper	$0.53\lambda_0 \times 0.53\lambda_0 \times 0.0135\lambda_0$	$2.27 - 5.56$GHz (82.25%)	> 28	< -30

IV. CONCLUSION

In this paper, a compact ultra-wideband dual-polarization planar slotted antenna has been designed, optimized and fabricated. It consists of a mushroom-shaped radiation patch and a ground surface, both of which form a gap and are located above the dielectric substrate. Coplanar waveguide structure is used for differential feed to suppress cross polarization. By extending the ground to the patch direction and loading a cross-shape slot in the middle of the radiation patch, the operating frequency band of the antenna is effectively widened. The simulated and measured results show that the relative bandwidth of the proposed antenna is 82.25% (2.27 $\sim$ 5.56 GHz), the cross polarization is less than $-$ 30 dB, and the port isolation is higher than 28 dB. The proposed antenna, with a height of $0.0135\lambda_0$ (where λ_0 is the free-space wavelength at central frequency 4 GHz), has the advantages of easy fabrication, stable radiation, and low cross polarization, so it is suitable for dual polarization communication systems.

ACKNOWLEDGEMENTS

This work was supported in part by Enterprise entrusted project, China (No. W2021JSKF0153, No. W2020JSFW0112), in part by HeFei University of Technology teacher program, China (No. JZ2019HGTB0093), in part by the Natural Science Foundation of Anhui Province (No. JZ2022AKZR0453), in part by the open research fund of National Mobile Communications Research Laboratory, Southeast University (No.2023D05), and in part by Anhui Natural Science Foundation (No. 2208085MF161).

REFERENCES

[1] P. Qin, L. Ji, S. Chen, and Y. J. Guo, "Dual-polarized wideband Fabry–Perot antenna with quad-layer partially reflective surface," *IEEE Antennas Wirel. Propag. Lett.*, vol. 17, no. 4, pp. 551-554, Feb. 2018.

[2] Z. Tang, J. Liu, R. Lian, Y. Li, and Y. Yin, "Wideband differentially fed dual-polarized planar antenna and its array with high common-mode suppression," *IEEE Trans. Antenn. Propag.*, vol. 67, no. 1, pp. 131-139, Oct. 2019.

[3] B. Peng, S. Li, J. Zhu, L. Deng, and Y. Gao, "A compact wideband dual-polarized slot antenna with five resonances," *IEEE Antennas Wirel. Propag. Lett.*, vol. 16, pp. 2366-2369, June 2017.

[4] Y. Chen, W. Lin, S. Li, and A. Raza, "A broadband $\pm 45^\circ$ dual-polarized multidipole antenna fed by capacitive coupling," *IEEE Trans. Antenn. Propag.*, vol. 66, no. 5, pp. 2644-2649, Feb. 2018.

[5] H. Jin, L. Zhu, H. Zou, Y. Luo, S. Xu, and G. Yang, "A wideband dual-polarized antenna and its array with electrically downtilt function for 5G sub-6 GHz communication applications," *IEEE Access*, vol. 8, pp. 7672-7681, Dec. 2020.

[6] Y. Li, C. Wang, and Y. X. Guo, "A Ka-Band wideband dual-polarized magnetoelectric dipole antenna array on LTCC," *IEEE Trans. Antenn. Propag.*, vol. 68, no. 6, pp. 4985-4990, Nov. 2020.

[7] D. Zheng and Q. Chu, "A wideband dual-polarized antenna with two independently controllable resonant modes and its array for base-station applications," *IEEE Antennas Wirel. Propag. Lett.*, vol. 16, pp. 2014-2017, Apr. 2017.

[8] H. Tang, J. Chen, W. Yang, L. Zhou, and W. Li, "Differential dual-band dual-polarized dielectric resonator antenna," *IEEE Trans. Antenn. Propag.*, vol. 65, no. 2, pp. 855-860, Nov. 2017.

[9] Z. Zhang and K. Wu, "A wideband dual-polarized dielectric magnetoelectric dipole antenna," *IEEE Trans. Antenn. Propag.*, vol. 66, no. 10, pp. 5590-5595, July 2018.

[10] L. Wen, S. Gao, Q. Luo, Q. Yang, W. Hu , Y. Yin, X. Ren, and J. Wu, "A compact wideband dual-polarized antenna with enhanced upper out-of-band suppression," *IEEE Trans. Antenn. Propag.*, vol. 67, no. 8, pp. 5194-5202, May 2019.

[11] C. Zhou, H. Wong, and L. K. Yeung, "A wideband dual-polarized inductor-end slot antenna with stable beamwidth," *IEEE Antennas Wirel. Propag. Lett.*, vol. 17, no. 4, pp. 608-612, Feb. 2018.

[12] S. Zhou, P. Tan, and T. Chio, "Low-profile, wideband dual-polarized antenna with high isolation and low cross polarization," *IEEE Antennas Wirel. Propag. Lett.*, vol. 11, pp. 1032-1035, Aug. 2012.
[13] Y. Zhang, "Wideband Low-Profile Dual-Polarized Antenna," Harbin Institute of Technology, June 2019.
[14] S. Jamilan, M. A. Antoniades, J. Nourinia, and M. N. Azarmanesh, "A directivity-band-dependent triple-band and wideband dual-polarized monopole antenna loaded with a via-free CRLH unit cell," *IEEE Antennas Wirel. Propag. Lett.*, vol. 14, pp. 855-858, Dec. 2015.
[15] B. Peng, S. Li, J. Zhu, L. Deng, and Y. Gao, "A compact wideband dual-polarized slot antenna with five resonances," *IEEE Antennas Wirel. Propag. Lett.*, vol. 16, pp. 2366-2369, 2017.
[16] Y. Liu and Z. Tu, "Compact differential band-notched stepped-slot UWB-MIMO antenna with common-mode suppression," *IEEE Antennas Wirel. Propag. Lett*, vol. 16, pp. 593-596, July 2017.
[17] Z. Tang, J. Liu, R. Lian, Y. Li, and Y. Yin, "Wideband differentially fed dual-polarized planar antenna and its array with high common-mode suppression," *IEEE Trans. Antenn. Propag.*, vol. 67, no. 1, pp. 131-139, Oct. 2019.

Zhao Neng Jiang was born in Jiangsu, China. He received the Ph.D. degree from Nanjing University of Science and Technology, Nanjing, China, in 2012. Since 2013 he has worked on numerical methods of computational electromagnetism. His current focus is on antenna and microwave devices. (Email: jiangzhaoneng@hfut.edu.cn)

Zhi Xin Wang was born in Anhui, China, in 1998. She is currently working towards the M.E. degree in Computer and Information Engineering from Hefei University of Technology. Her current focus is on antenna and microwave device design. (Email: 1364665074@qq.com)

Xiao Feng Xuan was born in Anhui, China, in 1975. He received the M.S. degree from Nanjing University, China. His focus is on numerical methods of computational electromagnetism. (Email: 941067868@qq.com)

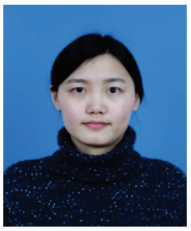

Li Ying Nie (corresponding author) received the Ph.D. degree from the University of Electronic Science and Technology of China. Her focus is on the theory and design of microwave and millimeter wave antenna. (Email: liyingnie@sina.com)

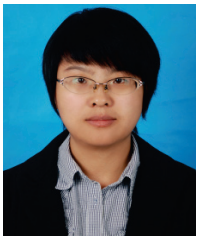

Ye Jiang received the B.Sc. and M.Sc. degrees in Communication Engineering from China University of Mining and Technology, Xuzhou, China, in 2010 and 2013 respectively. And the Ph.D. degree in Communication and Information System from University of Chinese Academy of Science, Shanghai, China, in 2017. She is a lecture with the School of Computer Science and Information Engineering, Hefei University of Technology, Hefei, China. Her current research interests include artificial intelligence technology and intelligence computation. She has published over 10 refereed articles.

Design of a Miniatured, Electromagnetic Quasi-Yagi Antenna with Circularly Polarized Characteristics

YunQi Zhang [1], LiFang Liu [1], Zhao Sun [2], XuPing Li [1], JunLing Che [3], and HaoYu Li[1]

[1]School of Electronic Engineering
Xi'an University of Posts & Telecommunications, Xi'an 710121, China
zhangyunqi@xupt.edu.cn, 1297629327@qq.com, lixuping@163.com, 779464178@qq.com

[2]Xi' an Branch
China Academy of Space Technology, Xi'an 710121, China
1050441091@qq.com

[3]School of Science
Xi'an University of Posts & Telecommunications, Xi'an 710121, China
junling.che@163.com

Abstract – A novel low-profile circularly polarized (CP) quasi-Yagi antenna with a wide 3-dB axial ratio (AR) bandwidth is proposed, which generates the endfire beam by combining magnetic microstrip cavity and folded electric dipoles with a 90° phase difference. The proposed antenna includes two shorting pins, which are employed to attain wider impedance bandwidth. Then, a phase delay line is added to connects two pairs of folded dipoles and a magnetic microstrip cavity to realize righthanded circularly polarized (RHCP). After optimization, a prototype with an overall size of $1.17 \times 0.91 \times 0.0387\lambda_0^3$ is designed. Simulated results demonstrate that the final model has 18.1% (5.01-6.01 GHz) 3-dB AR bandwidth and −10 dB impedance bandwidth of $5.2\%(5.67-5.97\ \text{GHz})$, respectively. In addition, experimental results demonstrate that the designed antenna is very applicable to the RFID system.

Index Terms – circularly polarized, endfire, folded dipoles, quasi-Yagi, RFID.

I. INTRODUCTION

Research on CP antennas can be traced back to the 1940s [1]. It can not only reduce the multipath effect, but also mitigate the polarization mismatch between receivers and transmitters [2–4]. Therefore, CP antennas are widely used in RFID systems [5], wireless communication [6] and satellite navigation receiving systems. Recently, endfire CP antennas have attracted much attention because of their two characteristics: strong directivity and high radiation efficiency. According to the difference in antenna structure, conventional endfire CP antennas can be roughly divided into two categories: helical antenna [7, 8] and Yagi-Uda antenna. However, not all of them can realize the required performance, where the main beam is parallel to the antenna plane and the carrier can be invisible [9]. In [10], a typical planar endfire CP antenna is introduced, which is based on the combination of orthogonal magnetic dipole and the electric dipole. Nevertheless, the designed antenna exhibits exceptionally narrow impedance bandwidth and AR bandwidth (i.e., only 2.4% and 9.24% approximately). Recently, some efforts have been made to change this situation [11–16]. A wide impedance bandwidth has been explored through assembling magnetic dipoles and a V-shaped open loop in [11]. Reference [12] also demonstrates that a wide AR bandwidth can also be acquired by increasing electric dipole width. In [13], by using the concentric annular sector, a low-complexity antenna with wide AR bandwidth has been presented. So far, some novel CP endfire antennas are well-known for obtaining better radiation capacity. However, the gain is still relatively low as studied in [14–16].

Planar endfire CP quasi-Yagi antennas, carrying a parasitic strip in front of driven elements, are adopted to improve the antenna gain [17, 18]. Unsatisfactorily, most of the reported antennas may suffer from a deterioration in AR bandwidth or impedance bandwidth. In [19], a complex vertically polarized structure and horizontally polarized Yagi arrays are introduced to obtain good performance. Therefore, it is challenging and desirable to design a high gain, wide bandwidth planar endfire CP quasi-Yagi antenna.

A new complementary CP quasi-Yagi antenna is discussed in this communication. Two pairs of folded dipoles are used to expand the AR bandwidth, which are printed on the upper and lower layers of the dielectric substrate, respectively. A parasitic strip serves as the

Submitted On: November 8, 2022
Accepted On: March 27, 2023

https://doi.org/10.13052/2023.ACES.J.380306

director to improve the gain. The folded dipole and the magnetic microstrip cavity are connected by the phase delay line, and the 90° phase difference can be introduced by changing the length of the phase delay line. Finally, a CP quasi-Yagi antenna has been achieved, which generates a peak gain of 5.1 dBic. The designed antenna has approximately 4.3% measured impedance bandwidth and 14.1% AR bandwidth with an extremely low profile of 0.0387 λ_0.

II. ANTENNA DESIGN

The configuration of the proposed antenna with endfire CP characteristic is illustrated in Fig. 1, which is designed on a rectangular dielectric substrate F4B ($\tan\delta = 0.001$), a relative permittivity of $\varepsilon_r = 2.65$, and a thickness of $h = 2$ mm. As seen, the proposed antenna mainly comprises a magnetic microstrip cavity, phase delay line, director and two pairs of folded dipoles. The magnetic microstrip cavity, connecting with two pairs of folded dipoles by phase delay line, is composed of three short edges and an open aperture. In addition, two shorting pins are placed in the magnetic microstrip cavity to excite the disturbance field and broaden the impedance bandwidth [20]. The antenna has the same top and bottom layout. A coaxial connector with a characteristic impedance of 50 Ω in which the inner conductor is connected to the upper layer and the outer conductor is welded to the lower layer. The director is added in the endfire direction to enhance the gain and radiation efficiency. All actual dimensions of the proposed antenna are as follows: $L_1 = 60.5$ mm, $W_1 = 47.1$ mm, $L_2 = 14.25$ mm, $W_2 = 8.2$ mm, $L_3 = 5.4$ mm, $W_3 = 0.34$ mm, $L_4 = 9.9$ mm, $W_4 = 3.8$ mm, $L_5 = 7.6$ mm, $L_6 = 4$ mm, $L_7 = 7.6$ mm, $Lx = 12.1$ mm, $Wx = 2.1$ mm, $d = 0.3$ mm, $d_1 = 0.7$ mm, $g = 4.2$ mm, $W_5 = 3.2$ mm, $\alpha = 85°$.

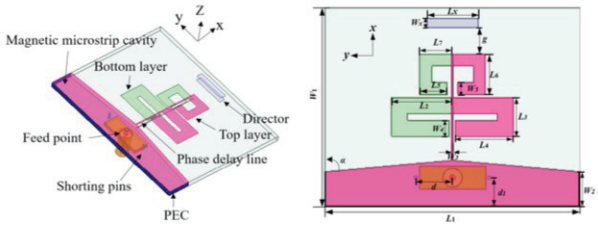

(a) (b)

Fig. 1. Geometry for the proposed antenna. (a) 3-D structure; (b) Top view.

A. Design procedure

The simple model of antenna is mainly composed of a magnetic dipole, electric dipole and phase delay line. The 90° phase difference is mainly provided by the length d of the phase shift line between them, as shown in Fig. 2. Among them, the magnetic dipole produces an "eight" shaped radiation pattern in the azimuth plane (xoy-plane) and an "O" shaped radiation pattern in the elevation plane (xoz-plane). The result proves that the antenna resonates as a vertically polarized electromagnetic wave. The electric dipole has a complementary orthogonal mode with respect to the magnetic dipole.

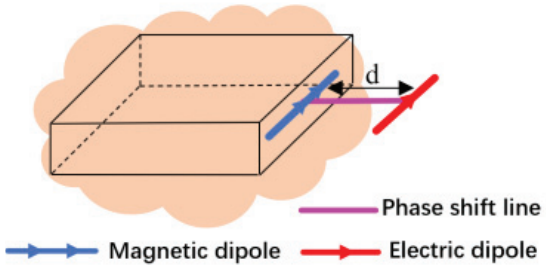

Fig. 2. Schematic diagram of the proposed antenna.

To clarify the design criteria of the proposed antenna, the design processes are present in Fig. 3 from ANT 1 to ANT 4 , and corresponding simulation results are displayed in Fig. 4. ANT 1 has an original printed electric dipole without shorting pins. In ANT 2, electric dipoles have been folded and two shorting pins are added based on ANT 1. As for ANT 3, an additional folded printed electric dipole is introduced compared with ANT 2. The final structure can be obtained by adding a director above ANT 3 .

By properly designing the antenna structure, the simulated $|S_{11}|$, AR and gain results of these antennas are presented in Fig. 4. First, by adding shorting pins and

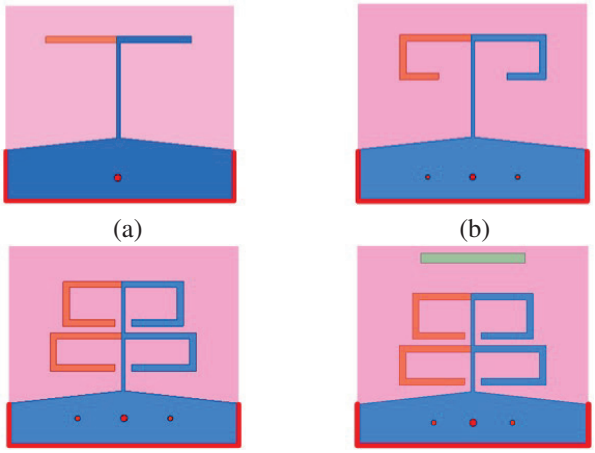

(a) (b) (c) (d)

Fig. 3. Evolution processes for the quasi-Yagi antenna. (a) ANT 1; (b) ANT 2; (c) ANT 3; (d) ANT 4.

folded dipoles, the axial ratio and reflection coefficient are greatly reduced (For ease of comparison, the same resonant frequency is used for each antenna). Second, it can be observed from Fig. 4 (b) that 3 dB AR bandwidth is greatly improved, and two resonance points appear at 5.4 GHz and 6.05 GHz by properly introducing a pair of folded dipoles. Finally, after adding the director, the gain of the designed antenna is up to 4.9 dBic.

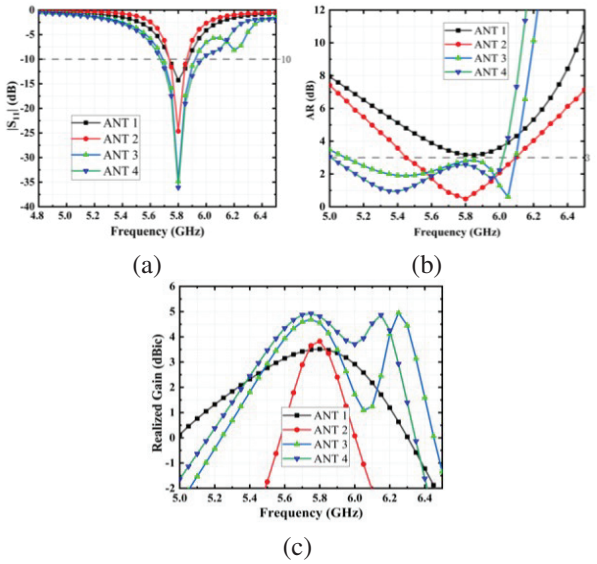

Fig. 4. Results of the process of the cp quasi-Yagi antenna. (a) $|S_{11}|$; (b) AR; (c) Realized gain.

B. Operating mechanism

A circular polarization wave could be generated with two electric field vectors of the same amplitude and 90° phase difference. The working principle of the proposed antenna is shown in Fig. 5, where Fig. 5 (a) refers to the equivalent model of the magnetic microstrip cavity [12]. The equivalent magnetic current source is parallel to the y-axis, the included angle between the x and y-axis is φ, and the included angle between y and z axis is θ. It can be known from the literature that the normalized electric field generated by the aperture at any point in free space in Fig. 5 (a) is:

$$\vec{E}_{\text{aperture}} = \vec{E}_\theta + \vec{E}_\varphi = \hat{\theta}\cos\varphi + \hat{\varphi}\cos\theta\sin\varphi. \quad (1)$$

Figure 5 (b) put forward an equivalent source model of two pairs of folded dipoles. To simplify the analysis and reveal the radiation characteristics of the folded dipole antenna, it is assumed that all equivalent current sources or current sheets are ideal short dipoles [11]. It can be seen from Fig. 5 (b) that the current components in the x-direction cancel each other, while the current components in the y-direction are linearly superposed. Consequently, the main radiation characteristics of the folded dipole should be determined by the y-direction components of the eight current sheets. Therefore, we can get the normalized electric field intensity superimposed by the folded dipole vector as follows:

$$\vec{E}_{\text{dipole}} = \vec{E}_\theta + \vec{E}_\varphi = \hat{\theta}\cos\theta\sin\varphi + \hat{\varphi}\cos\varphi. \quad (2)$$

Figure 5 (c) shows the entire operating mechanism of the proposed antenna. The magnetic microstrip cavity and the folded dipoles are excited with equal amplitudes and 90° phase difference, and no additional time phase difference ($\delta_0 = 0$) is introduced. The total far-field of the combined geometry will be:

$$\vec{E}_{\text{total}} = \vec{E}_{\text{aperture}} + e^{-j(kd\sin\theta\cos\varphi+\delta_0)}\vec{E}_{\text{dipole}}. \quad (3)$$

By substituting equation (2) into equation (3), the normalized electric field in the x-direction ($\theta = 90°, \varphi = 0°$) can be obtained as:

$$\vec{E}_{+x} = \hat{\theta} + \hat{\varphi}j. \quad (4)$$

It can be seen from equation (4) that the amplitude is equal and the phase difference is 90° in the $+x$ direction, and the ideal circular polarization radiation characteristic can be obtained [21].

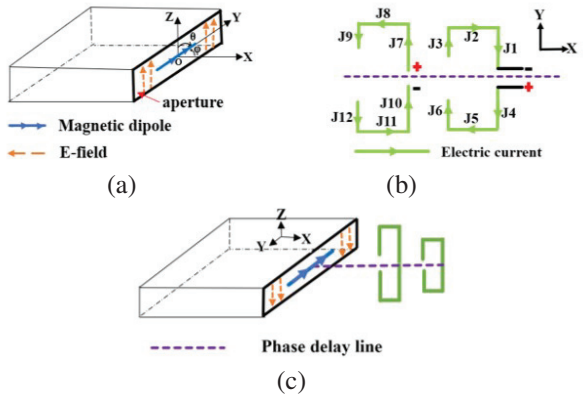

Fig. 5. Operating principle of this antenna. (a) Equivalent model of aperture element; (b) Equivalent source model of two-element folded dipole; (c) Working principle of the proposed antenna.

A 90° phase difference is necessary to generate circularly polarized waves. There are many ways to introduce a 90° phase difference, such as adding EZR-MZR resonances [22], dual-feed and phase delay line. However, it is mainly produced by adjusting the length of the phase delay line in this paper.

To further demonstrate the mechanism of the circular polarization radiation, the simulated vector surface current distributions of the short magnetic wall and director at different times t = 0, T/4, T/2,3 T/4 are exhibited from Figs. 6 (a) to (d) at 5.8 GHz, respectively. The director current can be obtained by coupling the current on the folded dipoles. Note that a solid red thick arrow in the upper right corner of each plot represents the synthetic short magnetic wall current and director current. By analyzing the trajectory of the synthetic current, the polarization mode of the proposed antenna can be clearly understood.

As demonstrated in Fig. 6 (a), the vector current of the short magnetic wall is toward the $+z$-axis, while the vector current of the director is toward the $+y$-axis. Therefore, the total current I_1 can be synthesized at $t =$ 0T. As shown in Fig. 6 (b), the new vector total current (I_2) can be obtained at t = T/4 with the change of director current. According to the analysis, this change is mainly caused by the current change on the longer folded dipole. Regarding Fig. 6 (c), it is clearly shown that the synthetic current I_3 can be acquired due to the transformation of the current direction on the short magnetic wall. Similarly, I_4 can be attained with similar method. From the above description, it can be inferred that a clockwise polarization wave is formed on the *yoz*-plane. Utilizing the right-hand spiral criterion, it can be concluded that the antenna has realized the RHCP radiation in $+x$ direction.

C. Operating mechanism

The performance of the proposed antenna shows greater sensitivity for variation in some parameters, such as the length (L_1) and width (W_2) of the magnetic microstrip cavity. As depicted in Fig. 7 (a), L_1 has a significant impact on the AR of the designed antenna. With the increase of L_1, the magnetic dipole current component is strengthened, and the AR is well improved. However, when L_1 increases to a certain extent, the AR performance deteriorates because the vertical electric field component is larger than the horizontal electric field component and the amplitude is not equal. It can be seen that when L_1 is equal to 60.5 mm, the optimal results of AR performance can be obtained.

It can be seen from Fig. 7 (b) that W_2 has a significant effect on the resonant frequency of the designed antenna. With the change of W_2, the resonant frequency of the antenna is constant change. The change of W_2 is equivalent to the movement of the position of the coaxial feed point. When W_2 is selected as 8.2 mm, the resonant frequency works exactly at 5.8 GHz.

Thereby, the designed antenna can be used in the RFID system.

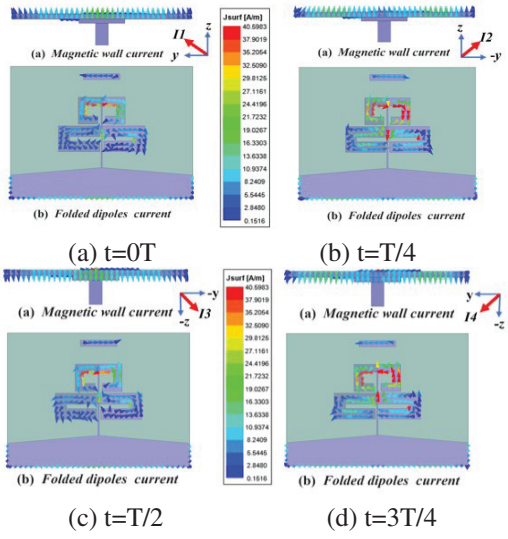

Fig. 6. The current distribution diagram is at 5.8 GHz. (a) t = 0 T; (b) t = 1/4 T; (c) t = 1/2 T; (d) t = 3/4T.

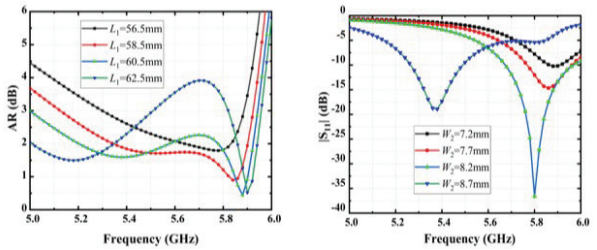

(a) L_1 (b) W_2

Fig. 7. Parameter study of L_1 and W_2. (a) L_1. (b) W_2.

III. EXPERIMENTAL RESULTS

A prototype, as shown in Fig. 8, was made to verify the characteristic of the proposed antenna. The measured results of reflection coefficient are obtained with the Agilent network analyzer, while the radiation and AR results are obtained in the anechoic chamber, as depicted in Fig. 8 (a).

Following Fig. 9 (a), the curves of simulated and measured reflection coefficients present similar variation trends. However, some discrepancies and fluctuations exist between the measured and simulation results, mainly owing to the unavoidable test errors. Finally, the measured -10 dB bandwidth is from 5.7 to 5.95 GHz, a reduction of about 50 MHz concerning the simulation results $(5.67 - 5.97$ GHz$)$.

The results of AR, gain are shown in Fig. 9 (b) and Fig. 9 (c), respectively. The simulation results with the measurement results of AR and realized gain are reasonably inconsistent, which may occur due to coaxial connector connection and fabrication errors. The

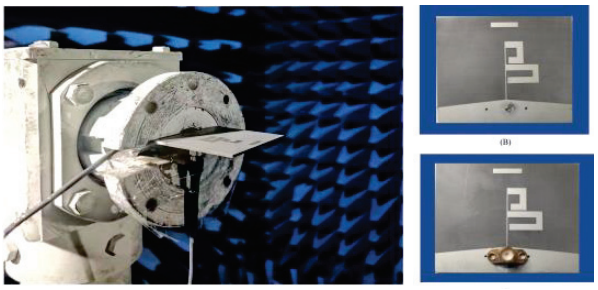

Fig. 8. (a) Measurement setup in the anechoic chamber. (b) The top view; (c) The back view.

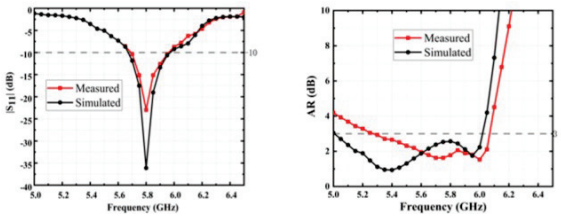

(a) $|S_{11}|$ (b) AR

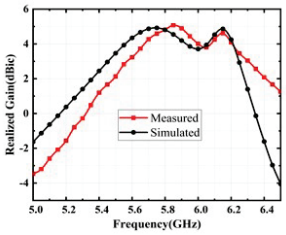

(c) Realized Gain

Fig. 9. Simulated and measured result for the proposed antenna. (a) $|S_{11}|$; (b) AR; (c) Realized gain.

experimental results illustrate that the proposed antenna achieves bandwidths of $14.1\%(5.27-6.07$ GHz) for AR < 3 dB and the gain can reach 5.1 dBic in the operating range. Although the experimental results of AR bandwidth and impedance bandwidth are narrow, they can still be used in RFID systems.

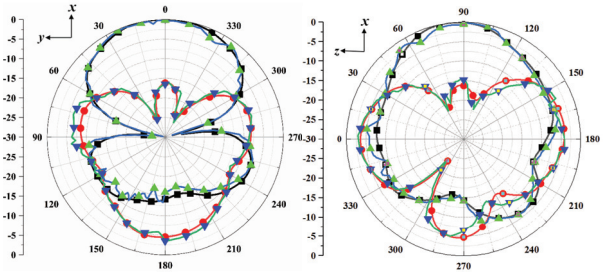

(a) xoy-plane (b) xoz-plane

Fig. 10. Simulated and measured normalized radiation patterns at 5.8 GHz for the quasi-Yagi antenna.

The normalized radiation patterns of the two main radiation planes at 5.8 GHz are shown in Fig. 10. Obviously, this antenna has a unidirectional RHCP mode in the desired operating frequency band. In addition, Table 1 gives a comparison of this antenna with other endfire CP antennas to highlight its advantages. It can be seen that the designed antenna has an appropriate size, wider AR bandwidth and higher gain. Based on its planar structure and easy integration, it is suitable for some terminal devices.

Table 1: Comparison of various endfire *CP* antennas

Ref	**BW**/%	**AR**/%	**Peck Gain (dBic)**	**Size** $/\lambda_0^3$
10	2.4	9.2	2.6	$0.59\times0.73\times0.053$
12	1.9	14.5	2.3	$0.99\times0.87\times0.053$
15	4.3	4.3	3.3	$1.74\times0.72\times0.0387$
17	1	1.5	7.2	$1.05\times0.65\times0.026$
18	5.2	5	7.8	$1.74\times0.97\times0.0387$
Pro	4.3	14.1	5.1	$1.17\times0.911\times0.0387$

IV. CONCLUSION

In this letter, A circularly polarized quasi-Yagi antenna with wide AR bandwidth and high gain is designed. A circularly polarized beam is formed by a combination of two pairs of folded electric dipoles and magnetic dipoles. The folded dipoles are used as driving elements in this antenna to improve the AR bandwidth. Two shorting pins are used to improve antenna impedance matching. The simulation and actual measurement of the antenna proved that the center frequency of the antenna was 5.8 GHz, which covers the frequency range of the RFID systems well.

ACKNOWLEDGMENT

This work is supported in part by Key Research and Development Program of Shaanxi (Program No. 2021GY-049 and 2022ZDLGY05-10) Science and Technology on Underwater Information and Control Laboratory (Program No. 6142218200312), and Xi'an Science and Technology Plan Project under Grant 21XJZZ0071.

REFERENCES

[1] J. D. Kraus, "Helical beam antennas for wide-band applications," *Proc. IRE*, vol. 36 , no. 10 , pp. 1236-1242, 1948.

[2] Y. Cheng and Y. Dong, "Wideband circularly polarized split patch antenna loaded with suspended rods," *IEEE Antennas Wirel. Propag. Lett.*, vol. 20, no. 2, pp. 229-233, 2021.

[3] Q. Chen, H. Zhang, L.-C. Yang, B. Xue, and Y.-C. Zeng, "Compact microstrip-via-fed wideband circularly polarized antenna with monofilar, spiral

stub for C-band applications," *Int. J. RF Microwav. Comput-Aided Eng.*, vol. 27, no. 7, e21118, 2017.

[4] Y.-H. Yang, B.-H. Sun, and J.-L. Guo, "A singlelayer wideband circularly polarized antenna for millimeter-wave applications," *IEEE Trans. Antennas Propag.*, vol. 68 , no. 6 , pp. 4925-4929, 2019.

[5] Y. Pan and Y. Dong, "Circularly polarized stack Yagi RFID reader antenna," *IEEE Antennas Wirel. Propag. Lett.*, vol. 19, no. 7, pp. 1053-1057, 2020.

[6] T.-V. Hoang, T.-T. Le, Q.-Y. Li, and H.-C. Park, "Quad-band circularly polarized antenna for 2.4/5.3/5.8-GHz WLAN and 3.5-GHz WiMAX applications," *IEEE Antennas Wirel. Propag. Lett.*, vol. 15, pp. 1032-1035, 2016.

[7] X.-D. Bai, J. J. Tang, X.-L. Liang, J.-P. Geng, and R.-H. Jin. "Compact design of triple-band circularly polarized quadrifular helix antennas," *IEEE Antennas Wirel. Propag. Lett.*, vol. 13, pp. 380-383, 2014.

[8] C.-R. Liu, Y.-X. Guo, and S.-Q. Xiao, "Circularly polarized helical antenna for ISM-band ingestible-capeule endoscope systems," *IEEE Trans. Antennas Propag.*, vol. 62, no. 12 , pp. 6027-6039, 2014.

[9] J. Huang and A.-C. Densmore, "Microstrip Yagi array antenna for mobile satellite vehicle application," *IEEE Trans. Antennas Propag.*, vol. 39 , no. 7, pp. 1024-1030, 1991.

[10] W.-J. Lu, J.-W. Shi, K.-F. Tong, and H.-B. Zhu, "Planar endifre circularly polarized antenna using combined magnetic dipoles," *IEEE Antennas WJol Propag. Lett.*, vol. 14, pp. 1263-1266, 2015.

[11] M. You, W.-J. Lu, B. Xue, L. Zhu, and H.-B. Zhu, "A novel planar endfire circularly polarized antenna with wide axial-ratio beamwidth and wide impedance bandwidth," *IEEE Trans. Antennas Propag.*, vol. 64 , no. 10 , pp. 4554-4559, 2016.

[12] W.-H. Zhang, W.-J. Lu, and K. W. Tam, "A planar end-fire circularly polarized complementary antenna with beam in parallel with its plane," *IEEE Trans. Antennas Propag.*, vol. 64, no. 3, pp. 1146-1152, 2016.

[13] B. Xue, M. You, W.-J. Lu, and L. Zhu, "Planar end-fire circularly polarized antenna using concentric amnular sector complementary dipoles," *Int. J. RF Microwa. Comput.-aid. Eng*. vol. 26, no. 9, pp. 829-838, 2016.

[14] H.-Q. Yang, M. You, W.-J. Lu, L. Zhu, and H. Zhu, "Envisioning an endfire circularly polarized antenna: presenting a planar antenna with a wide beamwidth and enhanced front-to-back ratio," *IEEE Antennas Propag. Mag.*, vol. 60, no. 4, pp. 70-79, 2018.

[15] J.-H. Liu, Y.-X. Li, Z.-X. Liang, and Y.-L. Long, "A planar quasi-magnetic-electric circularly polarized antenna," *IEEE Trans. Antennas Propag.*, vol. 64, no. 6, pp. 2108-2114, 2016.

[16] J. Zhang, W.-J. Lu, H. Zhu, L. Zhu, and L. Li, "Wideband dual-mode planar endfire antenna with circular polarisation," *Electron. Lett*, vol. 52, no. 12, pp. 1000-1001, 2016.

[17] M. Ye, X.-R. Li and Q.-X. Chu, "Planar end-fire circularly polarized antenna with unidirectional radiation," *in IEEE International Symposium on Antennas and Propagation & USVC/URSI National Radio Science Meeting*, San Diego, CA. USA, pp. 2313-2314, 2017.

[18] Y. Cheng and Y. D. Dong, "A directive circularly polarized planar Yagi array antenna," *in IEEE International Symposium on Antennas and Propagation and USNC-URSI Radio Science Meting, Atlanta*, GA, USA, pp. 1351-1352, 2019.

[19] W.-L. Zhou, J.-X. Liu, and Y. L. Long, "A broadband and high-gain planar complementary Yagi array antenna with circular polarization," *IEEE Trans. Antennas Propag. Lett.*, vol. 65, no. 3, pp. 1446-1451, 2017.

[20] Y. Gao, Z.-H. Xue, W.-M. Li, and W. Ren, "Widebeam planar end-fire circularly polarized antenna based on SIW," *International Conference on Microwave and Millimeter Wave Technology (ICMM)*, Guangzhou, China, pp. 1-3, 2019.

[21] C. A Balanis, *Antenna Theory: Analysis and Design*, 3rd ed, Wiley, Hoboken, NJ, USA, 2005.

[22] L. Peng, K. Sun, X. Jiang, S.-M. Li, and C.-L. Buan, "EZR-MZR resonators for compact low-profile omni-directional circular-polarized antenna design," *IEEE Photonics J.*, vol. 9, no. 4, pp. 1-15, 2017.

YunQi Zhang was born in Baglow Inner Mongolia, China in 1986. He received the PhD. degree from Xidjag, University, Xi'an, China in 2015. He is currently working in the Xi'an University of Posts & Telecommunications. His research interests include GPS antenna, CP antenna, omnidirectional antenna and antenna array designs.

LiFang Liu was born in Gansu, China, in 1994. She received the BEng degree from Lanzhou University of Technology, Gansu, China in 2017. Currently, she is pursuing an MS degree in Electronic Information from Xi'an University of Posts & Telecommunications. Her current interests include electromagnetic fields and microwave technology.

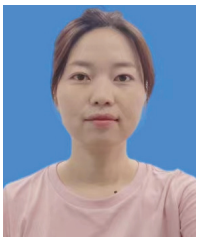

Zhao Sun was born in Shanxi, China, in 1988. She is currently working in Xi'an Branch of China Academy of Space Technology. Her current interests include low-orbit constellation and data link research.

XuPing Li was born in Xi'an, Shanxi, China in 1981. He received the PhD. degree in Electromagnetic Field and Microwave from Xi'an University, Xi'an, China in 2015. In January 2019, he was transferred to Xi'an University of Posts and Telecommunications as the leader of the phased array antenna technology research team. The principal focus of his research program is the development of phased array antennas.

JunLing Che is received the PhD degree in Electronic Science and Technology from Xi'an Jizgtong University, Xi'an, China in 2017. He is currently working in the Xi'an University of Posts & Telecommunications.

HaoYu Li was born in Anhui, China, in 1998. He received the BEng degree from Chyzhgu. University, Anhui, China in 2019. Currently, he is pursuing an MS degree in Electronic Information from Xi'an University of Posts & Telecommunications. His current interests include electromagnetic fields and microwave technology.

Design and Implementation of a Wilkinson Power Divider with Integrated Band Stop Filters Based on Parallel-coupled Lines

Ravee Phromloungsri[1] and Somchat Sonasang[2]

Department of Computer and Communication Engineering
Faculty of Technology UdonThani Rajabhat University, Udon Thani 41000, Thailand
phravee@gmail.com

Department of Electronic Technology
Faculty of Industrial Technology Nakhon Phanom University, Nakhon Phanom 48000, Thailand
somchat.s@npu.ac.th

Abstract – This paper presents a technique to improve the spurious suppression performance at the second harmonic ($2f_0$) of a Wilkinson power divider. The technique is achieved by the insertion of bandstop filters realizing with parallel-coupled lines with the characteristic impedance of $2\sqrt{Z_0}\Omega$ and the electrical length of $\lambda/8$ in a conventional structure. The simulated and measured results of the conventional and the proposed divider are compared at 0.9 GHz. The insertion losses (S_{21}, S_{31}) are less than 3.1 dB, while the return losses (S_{11}) are less than 34.6 dB across 100% fractional bandwidth. Moreover, the proposed Wilkinson power divider achieves more than 25.5 dB suppression at $2f_0$.

Index Terms – band stop filter, harmonics suppression, parallel-coupled lines, Wilkinson power divider.

I. INTRODUCTION

The Wilkinson power divider, first introduced by Wilkinson [1], is an essential component for microwave and millimeter-wave applications. It is widely used because of its useful property of being perfectly matched at all ports, high isolation between the output ports [2] and power divider with harmonics suppression [3–5]. The Wilkinson power divider consists of two quarter-wavelength branches of transmission lines with a characteristic impedance $2\sqrt{Z_0}$ and a parallel resistor $2Z_0$ connecting two output ports as shown in Fig. 1 (a). A conventional Wilkinson power divider is designed based on the electrical length of a desired fundamental frequency. However, high-order harmonic signals appear at the output ports due to the periodic characteristics of a transmission line. In addition, using the quarter-wavelength transmission lines will unavoidably lead to poor selectivity in each transmission path. The selectivity can be improved by adding bandpass filters at the input or at each output port of the Wilkinson power divider. However, this approach is not suitable for a compact design [6–8].

Several researchers presented a Wilkinson power divider for reducing high-order harmonic frequency, such as a band pass filter using the open/shot stub [9], third order bandpass filter high order [10], lowpass filter [11–12], and all mentioned above techniques can reduce the harmonics frequency suppression perfectly. Most techniques are limited due to their fabrication com-

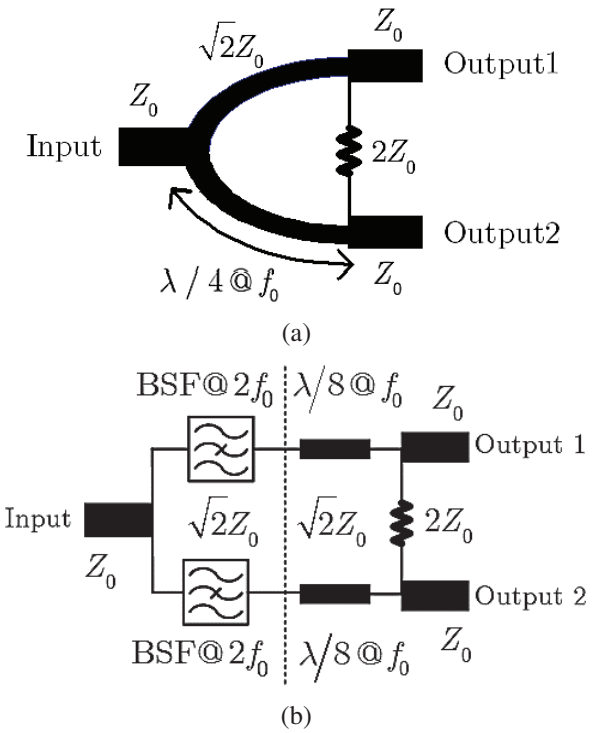

Fig. 1. Schematics of (a) conventional and (b) the proposed Wilkinson power divider with integrated band stop filter.

Submitted On: October 20, 2022
Accepted On: March 16, 2023

https://doi.org/10.13052/2023.ACES.J.380307

plexities. Employing a transmission line with inherent bandstop filter functionality, we propose a replacement of ordinary quarter-wavelength branches of transmission lines with the parallel-coupled lines bandstop filters as shown in Fig. 1 (b).

Section II presents the basic theory of the proposed bandstop filter based on parallel-coupled lines to suppress the harmonic signals. The proposed method also results in the suppression of $2f_0$ frequency response, as presented in Section III. The paper is finally concluded in Section IV.

II. THEORY

A. Band stop filter based on parallel-coupled lines

Band stop filters (BSF) are important components in microwave and modern wireless communications systems. Their potential applications are rejecting higher harmonics and spurious passband responses in transmission line circuits. A conventional band stop circuit with either a shunt stub or stepped-impedance transmission line is not suitable due to its large circuit size [9, 13–16]. Recently, some periodic materials such as photonic bandgap (PBG), electromagnetic bandgap (EBG), and defected ground structure (DGS) [17–19], have been shown to exhibit good band stop filter characteristics and are popularly applied in band stop filter designs. Their stopband bandwidth and sharp cutoff frequency response are enhanced by increasing the periodic cells, which leads to a larger size and more transmission loss in the stopband. Moreover, PBG, EBG, and DGS require an etching process on the backside ground plane, and additional position calibration increases time consumption and helps overcome some machining difficulties [9].

We proposed a simple design of a compact band stop filter using parallel-coupled lines as shown in Fig. 2. To suppress the second harmonic frequency response, the proposed band stop filter is designed and implemented by using a section of $\lambda/8$ parallel-coupled lines and cascaded with an ordinary $\lambda/8$ at the operating frequency f_0 as shown in Fig. 1 (b). The function of the integrated band stop filter is to suppress spurious response in the transmission coefficient (S_{21}) at the second harmonic. The equations of the input reflection coefficient (S_{11}) and forward transmission coefficient (S_{21}) of the proposed

Fig. 2. Schematic of the proposed 2-port band stop filter based on parallel-coupled lines.

circuit are obtained from the relationship of voltage, current, and impedance of a 4-port parallel-coupled lines network [10] as shown in Fig. 2. These relationships can be expressed in Equations (1)-(4) as shown [20–21]:

$$V_1 = Z_{11}I_1 + Z_{13}I_3 + Z_{14}I_4, \tag{1}$$

$$V_2 = Z_{21}I_1 + Z_{23}I_3 + Z_{24}I_4, \tag{2}$$

$$0 = Z_{31}I_1 + Z_{33}I_3 + Z_{34}I_4, \tag{3}$$

$$V_4 = Z_{41}I_1 + Z_{43}I_3 + Z_{44}I_4. \tag{4}$$

From Fig. 2, the 4-port network of parallel-coupled lines is transformed into a 2-port band stop filter, where port 1 and port 4 are the input and output ports, respectively. The initial conditions are $V_3 = 0$ and $I_2 = 0$ to obtain the relationship between voltage, current and impedance parameters of the 2-port band stop filter. We eliminate I_3 from Equation (1) and (4). Therefore, the current I_3, which is a function of I_1 and I_4 as shown in Equation (5), is substituted into Equations (1) and (4), then the 2-port impedance matrix of the band stop filter is obtained as shown in Equation (6):

$$I_3 = -\frac{Z_{13}}{Z_{11}}I_1 - \frac{Z_{12}}{Z_{11}}I_4, \tag{5}$$

$$Z_{BSF} = \begin{bmatrix} \left(Z_{11} - Z_{13}^2/Z_{11}\right) & \left(Z_{14} - Z_{12}Z_{13}/Z_{11}\right) \\ \left(Z_{14} - Z_{12}Z_{13}/Z_{11}\right) & \left(Z_{11} - Z_{12}^2/Z_{11}\right) \end{bmatrix}, \tag{6}$$

where [21]:

$$Z_{11} = \frac{1}{2}\left(Z_{Oe}\coth\left(\theta_e\right) + Z_{00}\coth\left(\theta_0\right)\right)$$

$$Z_{12} = \frac{1}{2}\left(Z_{0e}\coth\left(\theta_e\right) - Z_{00}\coth\left(\theta_0\right)\right)$$

$$Z_{13} = \frac{1}{2}\left(Z_{0e}\operatorname{csch}\left(\theta_e\right) - Z_{00}\operatorname{csch}\left(\theta_0\right)\right)$$

$$Z_{14} = \frac{1}{2}\left(Z_{0e}\operatorname{csch}\left(\theta_e\right) + Z_{00}\operatorname{csch}\left(\theta_0\right)\right).$$

From Equation (6) $Z_{12T} = Z_{21T}$ and $Z_{11T}{}^1Z_{22T}$, the 2-port impedance matrix of the bandstop filter is shown in Equation (7):

$$\begin{bmatrix} V_1 \\ V_2 \end{bmatrix} = \begin{bmatrix} Z_{11T} & Z_{12T} \\ Z_{21T} & Z_{22T} \end{bmatrix} \begin{bmatrix} I_1 \\ I_2 \end{bmatrix}. \tag{7}$$

The 2-port matrix in Equation (6) was used to calculate the input impedance (Z_{in}), the input port reflection coefficient (S_{11}) and the forward transmission coefficient (S_{21}) of the proposed band stop filter as in Equations (8), (9) and (10) [21, 22]:

$$Z_{\text{in}} = Z_{11T} - \frac{Z_{12T}^2}{\left(Z_{22T} + Z_0\right)}, \tag{8}$$

$$S_{11} = \frac{\left(Z_{11T}^2 - Z_0^2\right) - Z_{12T}^2}{\left(Z_{11T} + Z_0\right)\left(Z_{22T} + Z_0\right) - Z_{12T}^2}, \tag{9}$$

$$S_{21} = \frac{2Z_0Z_{12T}}{\left(Z_{11T} + Z_0\right)^2 - Z_{12T}^2}. \tag{10}$$

Figure 3 shows the simulated results of the proposed band stop resonator in terms of S_{11} and S_{21}, where

the proposed bandpass filter is synthesized from a coupling factor of −10 dB parallel-coupled lines. Considering the inset figure shown in Fig. 3, the relevant voltage coupling factors of parallel-coupled lines for synthesizing the band stop filter are between −9 dB and −10 dB, which provides the best performance to suppress the spurious response at a frequency of $2f_0$. Therefore, in the proposed power divider, the band stop filters were synthesized from −10 dB coupling factor with characteristic impedance $Z_0 = 70.7\Omega$, the even and odd-mode impedances of coupled lines were $Z_{0e} = 98.09\Omega$ and $Z_{0o} = 50.95\Omega$, on Arlon AD-260A printed circuit boards with the following design parameters: $\varepsilon_r = 2.60$, $h = 1.0$ mm, $\tan\delta = 0.0017$ at the operating frequency of 1.8 GHz.

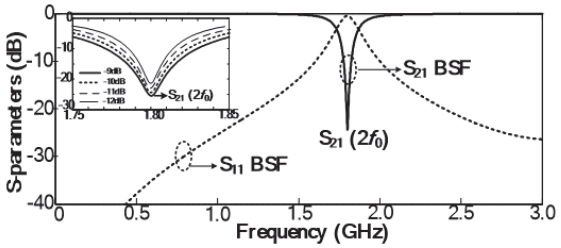

Fig. 3. Frequency response (S_{21}) and (S_{11}) of band stop filter based parallel-coupled lines.

B. The modified transmission line with integrated $2f_0$ band stop filter

The conventional Wilkinson power divider consists of two quarter-wavelength transmission lines with the characteristic impedance $\sqrt{2}Z_0$ connected between the input port and the two output ports. A resistor of $2Z_0$ connected between the output ports as shown in Fig. 1 (a). In this research, we insert the proposed band stop filter into each branch of a $\lambda/4$ transmission lines. Each transmission line is divided into two sections, as shown in Fig. 4. The first section is a $\lambda/8$ parallel-coupled-lines band stop filter, while the second part is an ordinary $\lambda/8$ transmission line. Both sections have characteristic impedances $\sqrt{2}Z_0$. These modified transmission lines have the same electrical length and characteristic impedance as the original design. However, it's particularly capable of suppressing the signal at the harmonic frequency $2f_0$ of the fundamental frequency of the Wilkinson power divider operating frequency due to the stop band network.

C. The proposed Wilkinson power divider with integrated $2f_0$ band stop filter

Based on the theories and concepts described in the previous section, a Wilkinson power divider capable of suppressing the second harmonic without adding a band

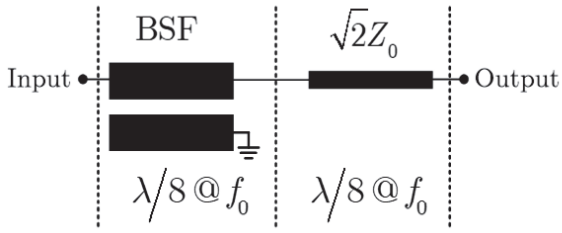

Fig. 4. The proposed synthetic transmission line with the integrated $2f_0$ spurious suppression band stop filter.

stop filter at the input port or the output ports is proposed. The band stop filter is integrated into the original design, as shown in Fig. 5. The replaced modified transmission lines maintain the original electrical properties of the conventional design. The size of the circuit is increased from the conventional circuit by 10% in the y-axis and increased by 10% when considering the overall area. The circuit design is simple, with minimal adjustments to the length of the transmission line to meet the desired operating frequency f_0. The proposed Wilkinson power divider was designed and simulated on Arlon AD-260A printed circuit board. The integrated band stop filters were synthesized using a −10 dB coupling coefficient parallel-coupled lines with the following design parameters: $\varepsilon_r = 2.60$, $h = 1.0$ mm, and $\tan\delta = 0.0017$ at the operating frequency of 0.9 GHz.

The insertion losses (S_{21}, S_{31}) and the input return loss (S_{11}), are not different from those of the conventional circuit. A significant change in the input return loss is achieved by the the coupled lines via holes. The simulated results in Fig. 6 show that, S_{11} of the proposed circuit (—) increases when compared to the conventional circuit (——) at the frequencies 0.9 GHz (f_0) and 1.8 GHz ($2f_0$), while, the S_{21} and S_{31} are preserved with −3 dB values in the range of the circuit bandwidth. The proposed circuit has the S_{21}, S_{31} suppression performance to less than −20 dB at the $2f_0$ or 1.8 GHz. However, parasitic inductance of the coupled

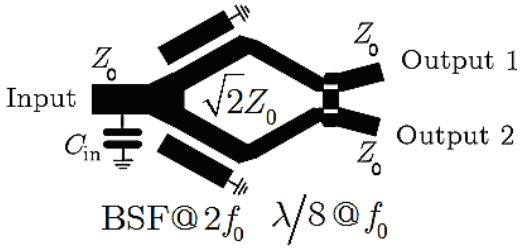

Fig. 5. Schematic of the proposed Wilkinson power divider with integrated BSF-based parallel-coupled lines and the shunted capacitance (C_{in}).

lines via holes significantly affects the return loss of the circuit. There are two approaches to tackle this. These are: 1) choose a printed circuit board with a thin substrate to reduce the inductance caused by the length of via ground and 2) add shunted capacitance (C_{in}) [13] at the input port as shown in Fig. 5 to improve the input matching.

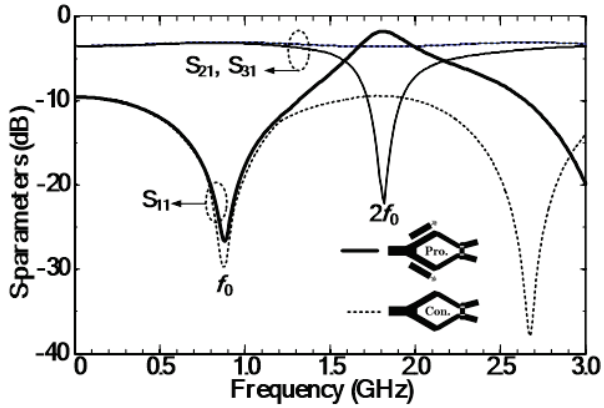

Fig. 6. Simulated frequency response of conventional and the proposed Wilkinson power divider.

III. DESIGN AND EXPERIMENTAL RESULTS

The proposed technique's performance is proven with a design of a 0.9 GHz operating frequency f_0 Wilkinson power divider. The circuit prototype is designed and fabricated on AD260A substrate (ε_r = 2.60, h = 1.0 mm, tan δ = 0.0017). The band stop filters were synthesized in the proposed circuit from −10 dB coupling coefficient parallel-coupled lines with electrical parameters Z_0 = 70.7Ω, Z_{0e} = 98.09 Ω, and Z_{0o} = 50.95Ω. Table 1 shows the dimensions of the proposed Wilkinson power divider. The conventional Wilkinson power divider employs ordinary transmission lines with W=1.50 mm and L =58.00 mm at the electrical length of 0.5π. While the proposed Wilkinson power divider consists of two subcircuits, the first subcircuit used 0.25π at 0.9 GHz parallel-coupled-lines with W =1.2 mm, S = 0.30 mm, and L = 19.00 mm. For the second subcircuit, a 0.25π transmission line with W = 1.50 mm, and L = 29.00 mm is employed. In the proposed circuit, the modified transmission line consists of a band stop filter based on $\lambda/8$ parallel-coupled lines operating at the frequency $2f_0$ of the Wilkinson power divider circuit cascaded with an ordinary $\lambda/8$ transmission line. This research used Sonnet-Lite and Matlab for simulation, data processing, and display. The simulated results of both circuits are shown in Fig. 6. The experiment was performed with an S5065 Vector Network Analyzer from Copper Mountain calibrated the frequencies from 0.1 to 3 GHz.

Table 1: The Wilkinson power divider circuits' physical dimensions

Wilkinson Power Divider	W,S,L (mm)	Electrical Length (rad)
Conventional	Ordinary lines W=1.50, L= 58.00	0.5π
Wilkinson with BSF	Ordinary Lines W=1.50, L= 29.00 BSF Coupled Lines W= 1.20, S=0.30, L=19.00	0.25π 0.25π

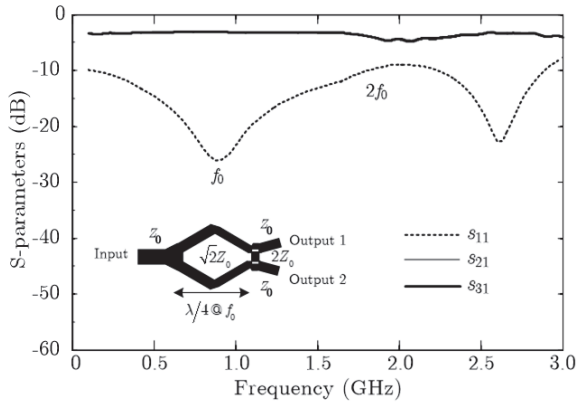

(a)

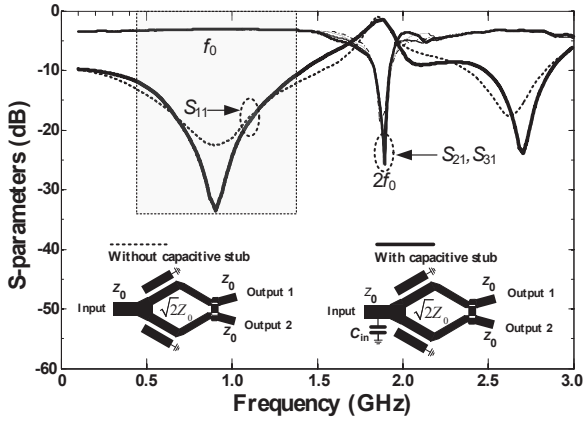

(b)

Fig. 7. Measured results of (a) conventional and (b) the proposed Wilkinson power divider with integrated band stop filters.

The measured results of the conventional power divider are shown in Fig. 7 (a). The values of the insertion loss S_{21} and S_{31} are approximately −3.00 dB, at frequencies from 0.1 to 3.0 GHz, while the S_{11} is less than −25.00 dB at 0.9 GHz and −10.10 dB at 1.8 GHz. In Fig. 7 (b), the insertion losses S_{21}, S_{31}, and return loss S_{11} of the proposed Wilkinson power divider

Table 2: The measurement S-Parameters of the circuits

Wilkinson Power Divider	Frequency (MHz)	% BW
Conventional	1,066	118
Wilkinson with BSF	1,255	136

Table 3: The comparison of Wilkinson power dividers

Ref.	Frequency (GHz)	Techniques	Implementation
[3]	1.65	Open stubs	Complicated
[4]	3.00	Parallel-coupled Line	Complicated
[5]	1.80	Open ended stubs	Complicated
[10]	2.45	Microstrip bandpass	Complicated
[20]	0.90	STIL compensated	Simple
This work	0.90	BSF coupled lines	Simple

around the operating frequency of 0.9 GHz are -3.10 dB and less than -34.60 dB with the input capacitive stub employed.

More than 100% fractional bandwidth is obtained, and the insertion loss' suppression performance at $2f_0$ is approximately more than -25 dB. Comparing the abilities of the proposed Wilkinson power divider and the conventional designs, the fractional bandwidths are 136 % and 118%, as shown in Table 2. Photographs of the conventional and the proposed Wilkinson power divider printed circuit boards with integrated band stop filter-based parallel-coupled lines are shown in Figs. 8 (a) and 8 (b). The circuit sizes, excluding the input and output connectors, of conventional and the proposed Wilkinson power divider, are approximately 24.5 cm^2 and 18.24 cm^2. The proposed circuit is 25% smaller than the conventional circuit.

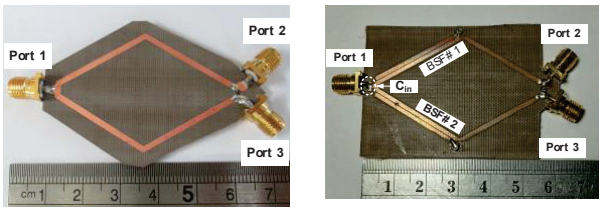

(a) (b)

Fig. 8. PCB photograph of (a) conventional and (b) the proposed Wilkinson power divider with integrated BSF-based coupled lines and the shunted capacitance (C_{in}) at the input port.

Table 3 summarizes previous works and the proposed circuit. Our design is based on band stop filter coupled lines, which is simple, while the other designs are more complicated. Therefore, the proposed Wilkinson power divider is more suitable in terms of implementation.

IV. CONCLUSION

A simple technique to improve the spurious response suppression at the second harmonic of a Wilkinson power divider by inserting a compact band stop parallel-coupled lines in the original circuit has been presented. The proposed technique has several distinct features, such as low insertion and returns losses, good selectivity in each output signal path, excellent spurious suppression, and simple design and implementation. Based on the experiment, the spurious response of the proposed Wilkinson power divider is more than 28 dB at the second harmonic. Therefore, the technique has potential for modern microwave and wireless communications.

ACKNOWLEDGMENT

The authors would like to demonstrate gratitude toward the Faculty of Industrial Technology of the Nakhon Phanom University for research time and the Department of Computer and Communication Engineering (CCE), Faculty of Technology, Udon Thani Rajabhat University (UDRU) for research grant, instrumentation and materials support.

REFERENCES

[1] E. J. Wilkinson, "An n-way hybrid power divider," *IRE Trans. Microw. Theory Tech.*, vol. 8, no. 1, pp. 116-118, Jan. 1960.

[2] D. M. Pozar, *Microwave Engineering*, John Wiley & Sons, New York, 2011.

[3] M. Hayati and S. Roshani, "A novel Wilkinson power divider using open stubs for the suppression of harmonics," *Applied Computational Electromagnetics Society (ACES) Journal*, vol. 28, no. 6, pp. 501-506, June 2013.

[4] X. Yu, S. Sheng, and L. Yun, "Design of wideband filtering power dividers with harmonic suppression based on the parallel-coupled line structures," *Applied Computational Electromagnetics Society (ACES) Journal*, vol. 33, no. 5, pp. 468-475, May 2018.

[5] S. Roshani, S. Koziel, S. Roshani, M. B. Jamshidi, F. Parandin, and S. Szczepanski, "Design of a patch power divider with simple structure and ultra-broadband harmonics suppression," *IEEE Access*, vol. 9, pp. 165734-165744, Dec. 2021.

[6] W. Tang, J. H. Ryu, and H. Kim, "Compact, tunable Wilkinson power divider ssing tunable synthetic transmission line," *Microw. Opt. Technol. Lett.*, vol. 52 no. 6, pp. 1434-1436, Mar. 2010.

[7] L. Wu, Z. Sun, H. Yilmaz, and M. Berroth, "A dual-frequency Wilkinson power divider," *IEEE Trans. Microw. Theory Tech.*, vol. 54, no. 1, pp. 278-284, Jan. 2006.

[8] Y. Sun and A. P. Freundorfer, "Broadband folded Wilkinson power combiner/splitter," *IEEE Microw. Wirel. Compon. Lett.*, vol. 14, no. 6, pp. 295-297, June 2004.

[9] S. Lotfi, S. Roshani, S. Roshani, and M. S. Gilan, "Wilkinson power divider with band-pass filtering response and harmonics suppression using open and short stubs," *Frequenz.,* vol. 74, no. 5-6, pp. 169-176, May 2020.

[10] H. S. Vaziri, S. Zarghami, F. Shama, and A. H. Kazemi, "Compact bandpass Wilkinson power divider with harmonics suppression," *AEU - Int. J. Electron. Commun*., vol. 117, Art. no. 153107, Apr. 2020.

[11] G. Moloudian, S. R. Miri Rostami, and T. Björninen, "Modified Wilkinson power divider with harmonics suppression and compact size for GSM applications," *Int. J. RF Microw. Comput.-Aided. Eng.*, vol. 30, no. 7, Art. no. e22209, July 2020.

[12] S. Karimi-khorrami and G. Moloudian, "Design and fabrication of a microstrip lowpass filter with wide tuning range as harmonic suppression with application in Wilkinson power divider," *Analog Integr. Circuits Signal Process.*, vol. 107, no. 1, pp. 155-163, Apr. 2021.

[13] M. Chongcheawchamnan, N. Siripon, and I. D. Robertson, "Designed and performance of improved lumped-distributed Wilkinson divider topology," *Electron. Lett*., vol. 37, no.8, pp. 1-2, Apr. 2001.

[14] P. H. Deng, L. C. Dai, and Y. D. Chen, "Integrating equal-split Wilkinson power dividers and coupled-line bandpass filters," *PIERS Proceedings*, Moscow, Russia, pp. 1249-1253, Aug. 2012.

[15] S. C. Lin, P. H. Deng, Y. S. Lin, C. H. Wang, and C. H. Chen, "Wide-stopband microstrip bandpass filters using dissimilar quarter-wavelength stepped-impedance resonators," *IEEE Trans. Microw. Theory Tech*., vol. 54, no. 3, pp. 1011-1018, Mar. 2006.

[16] M. C. Scardelletti, G. E. Ponchak, and T. M. Weller, "Miniaturized Wilkinson power dividers utilizing capacitive loading," *IEEE Microw. Wirel. Compon. Lett.*, vol. 12, no. 1, pp. 6-8, Jan. 2002.

[17] M. Kazerooni and A. Cheldavi, "Simulation, analysis, design and applications of array defected microstrip structure (ADMS) filters using rigorously coupled multi-strip (RCMS) method," *Prog. Electromagn. Res.*, vol. 63, pp. 193-207, Jan. 2006.

[18] C. J. Wang and C. S. Lin, "Compact DGS resonator with improvement of Q-factor," *Electron. Lett.*, vol. 44, no. 15, pp. 908-910, July 2008.

[19] D. W. Kim, "Small-sized high-power PIN diode switch with defected ground structure for wireless broadband internet," *ETRI J.*, vol. 28, no. 1, pp. 84-86, Feb. 2006.

[20] R. Phromloungsri, "An improvement of Wilkinson power divider with SITLs compensated microstrip band stop filter," *International Electrical Engineering Congress (iEECON)*, Chonburi, Thailand, pp. 450-453, Oct. 2014.

[21] J. G. Hong and M. J. Lancaster, *Microstrip Filters for RF/Microwave Applications*, K. Chang, Ed. New York, Wiley, 2001.

[22] L. Zhu, S. Sun, and R. Li, *Microwave Bandpass Filters for Wideband Communications*, John Wiley & Sons, Inc., New York, 2012.

Ravee Phromloungsri was born in Khon Kaen, Thailand. He received the B.Sc. (Applied Physics in Solid State Electronics) from King Mongkut Institute of Technology, Ladkrabang (KMITL) in 1992, M.Eng. in Electrical Engineering (Telecommunication) from Mahanakorn University of Technology (MUT) in 2000 and he is currently working toward the D. Eng. in Electrical Engineering in MUT. From 1992 to 2009, he joined MUT as a lecturer in the telecommunication engineering department. Currently, he is an assistant professor in the Department of Computer and Communication Engineering at Udon Thani Rajabhat University. His research interests include IoT/Automation system, and RF/Microwave circuits design.

Somchat Sonasang received the Ph.D. degree in Electrical and Computer Engineering from Mahasarakham University, Maha Sarakham, Thailand, in 2021. He is currently working in the Department of Electronic Technology, Faculty of Industrial Technology, Nakhon Phanom University, Thailand. His current research interests are microwave circuits, electromagnetic material characterization, non-destructive tests, Rabi oscillation and antenna.

Design and Simulation of a Slice-rail and Cylindrical for Multi-Projectile Electromagnetic Launchers

Shahab Mozafari and Mohammad Sajjad Bayati

Electrical Engineering Department
Razi University, Kermanshah, Iran
s.bayati@razi.ac.ir

Abstract – In Electromagnetic launcher (EML) research, beside reasonable $L\prime$ and high muzzle velocities, there are several key features including multi-turn launching, low field intensity in payload position, high frequency shooting, less unwanted radiation, and so on. Attaining a solution might be feasible by a different structure. In this paper we have studied unequal curved electromagnetic rail launchers (EMRLs) as slice and cylindrical multi-projectile electromagnetic launchers, and the inductance gradient ($L\prime$) of these structures has been calculated. Making multi-projectile EMRLs using a slice-rail structure is much easier than other plane methods. With a cylindrical multi-projectile EMRL, higher shooting frequency is more feasibly attained and there is no limit on the number of launchers at the same time. High temperature spots which are the result of high velocity and high current density distributions end in intense destructive erosion. Decreasing intense erosion in electromagnetic launcher structures will be more economical and provide greater reliability, therefore resulting in more applications for EMLs especially commercial ones. In parallel electromagnetic launchers, these points and areas are not omissible. In cylindrical EMRLs the problem of high current density distributions and its consequent erosion is significantly decreased because of the uniform distribution of current in its symmetric structure.

Index Terms – current density, electromagnetic launcher, inductance gradient, magnetic force, velocity.

I. INTRODUCTION

Electromagnetic launcher technology is a relatively recent development. Accelerating objects to very high velocities only using electrical energy can have many industrial applications [1–4]. As we know from basic physics, a current- carrying closed loop senses an expanding force in order to decrease changes in magnetic flow. An electromagnetic launcher works on this basic principle of physics, and in its simplest form is made up of two parallel long conductors, the rails, and a conductor between them, the armature. The exerted magnetic force on the armature, the Lorentz force, can be calculated by the integral of the $\mathbf{J}\times\mathbf{B}$ over the armature volume. $\mathbf{B}$ and $\mathbf{J}$ are the magnetic flux density and current density, respectively. Numerical simulation of an electromagnetic launcher is an interesting challenge that requires the computation of the inductance gradient, current density distribution, joule heat created in conductors and forces in the structure. Numerical methods such as finite element, boundary element and method of moment are reported in [5–8] and hybrid methods in [9–11]. Shape and material of the rails and armature determine current density distribution in an electromagnetic launcher. In a conventional rectangular electromagnetic launcher, maximum values of current density occur at inner corners of both rails [5], [12–14]. Inductance gradient is calculated by gradient of magnetic flux for two parallel rectangular conductors [5] which conforms for very long structures so a difference between 2D and 3D simulations is expected. A rectangular electromagnetic launcher with C-shaped armature has been simulated by finite element method in [12] where inductance gradient and current distribution are computed for various root ratios of C-shaped armature and rail overhang [12]. In [13], for various width (h), thickness (w) and the separation (s) between two parallel rails the inductance gradient has been computed [13]. Also, a closed formula for $L\prime$ is derived by using an intelligent estimation method [15]. Applied current to the electromagnetic launcher is a capacitor discharge, which is a very short pulse with a time duration of less than a few milliseconds, thus current distributes on the surface of the rails because of skin effects. By using this phenomenon, the solution based on the Schwartz–Christoffel map is presented for calculating the inductance gradient [16] and there is a negligible difference with results in [5, 13, 15]. Using finite element electromagnetic code, rectangular and circular electromagnetic launchers with one and two parallel augmented rails have been simulated to calculate self and mutual inductance gradient where the results showed that the rectangular rail shape with one pair of augmenting

Submitted On: September 3, 2021
Accepted On: March 18, 2022

https://doi.org/10.13052/2023.ACES.J.380308

rails is better than other shapes [17]. In [18], various rectangular and curved-bore electromagnetic launchers have been simulated to calculate $L\prime$ in which the cross-section of rails was equal to 1/10th of the electromagnetic launcher bore size. Multi-turn railguns are suitable options for applications in which a massive load should be accelerated to high velocities [19, 20].

Critical erosion in rails created by the launching process could result in flaws, especially with the next launch. Very hot spots at edges and corners because of high current densities, great tensions and stresses applied on rails because of repulsive forces, and very high velocity of armature, are major agents of erosion [21, 22]. Replacing the many parts of an electromagnetic launcher's structure after each launch is not desirable for reasons of time and cost. Additionally, replacing parts, especially rails, is impossible in proposed applications like asteroid mining and deflection [23]. Because of less erosion, field applications prefer circular EMLs despite experimental applications which recommend rectangular bores for its higher $L\prime$. Circular electromagnetic launchers have been studied [24] and it is obvious that there is no distinct advantage; not only does $L\prime$ decrease but the areas with high current densities also remain. Due to the shape of its armature that includes solid shapes like bullets, most research thus far has been done in the field of parallel electromagnetic launchers. More recently, ring arrangements of conventional railguns such as as quadrupoles and sextupoles have been considered in order to solve the problems of magnetic shielding without shielding coils or materials [25, 26]. By reducing the field magnitude in front of the armature especially in the center of the structure because of symmetrical designs, thrust/current ratios increase and magnetic shielding effects have improved. On the other hand, the inductance gradient has reduced by more than 60%.

The inductance gradient for a cylindrical electromagnetic launcher is comparable with a parallel electromagnetic launcher with proper geometrical values of its structure [27]. Also, experiments have shown a noticeable decrease in the field intensity in front of the armature [28] and 2D simulated in [29]. Early military applications of electromagnetic launchers, which involved launching a solid armature like a bullet, led researchers to parallel electromagnetic launchers, thereby neglecting the cylindrical structure. By using unequal circular rails, we moved to cylindrical structures that have no sharp edges and corners. A multi-projectile structure is achievable when several slice-rails are arranged circularly. It is also possible to unite their inner rails. By arranging the curved rails in a cylindrical structure, the magnetic field distributions have been changed to circles inbounded in the bore of launcher. Because of field concentration between the rails, obtaining higher $L\prime$s is respected. In this paper, slice-rail, multi-projectile and cylindrical electromagnetic rail launchers are presented and simulated by 3D-FEM. For each one, inductance gradient has been calculated and compared together. Also, force and current density distributions in rails and in armature have been shown and discussed.

II. GOVERNING EQUATIONS

The behavior of the electromagnetic field in an EML obeys basic Maxwell's equations. In the absence of free magnetic poles, $\boldsymbol{B}$ must be the curl of magnetic vector potential ($\boldsymbol{A}$) as the following:

$$\nabla \bullet B = 0 \ \rightarrow B = \nabla \times A, \tag{1}$$

$$\nabla \times H = \sigma E + J_s \ \rightarrow \nabla \times \left(\frac{\nabla \times A}{\mu} \right) + \sigma \frac{\partial A}{\partial t} = J_s, \tag{2}$$

where $\boldsymbol{J}_s$ is impressed current density and σ is conductivity, μ is permeability and equals to μ_o. The equation of magnetic force ($\boldsymbol{F}_m$) is described as the following:

$$F_m = \int J \times B \, dv = \frac{L\prime I^2}{2}, \tag{3}$$

where $\boldsymbol{J}$ and $\boldsymbol{B}$ are current density and magnetic flux density on the armature volume, respectively. Inductance gradient can be obtained by the following:

$$L' = \frac{2F_m}{I^2}, \tag{4}$$

I is applied current and $L\prime$ is inductance gradient and depends on the geometrical shape and physical arrangement of the rails.

III. SLICE-RAIL ELECTROMAGNETIC LAUNCHER

Electromagnetic launchers with equal rails have been studied considerably while desired geometries for rails is rectangular, concave, convex, and circular. An electromagnetic rail launcher (EMRL) with unequal rails is unusual in EML technology but, as we will see in this paper, it is a viable and useful design especially for a multi-projectile advancement. A concave-convex pair of rails has been considered in which the convex rail is smaller, especially when both rails are concentric. It looks like a parallel rectangular electromagnetic launcher which has overhead in only one rail. The geometry and cross-section of the electromagnetic slice-rail launcher (EMSRL) is shown in Fig. 1 where L_R, L_{arm}, R_i, R_o and θ are EMSRL length, armature length, inner rail radii, outer rail radii, and the total angle of curved rails, correspondingly.

A. Inductance gradient and force distribution

If both rails of a conventional parallel EMRL are curved in the same direction, it can be considered a slice-rail. Thus, the role of height in conventional parallel EMRLs is the same role of θ in EMSRLs. By increasing the angle θ, there are two parallel currents

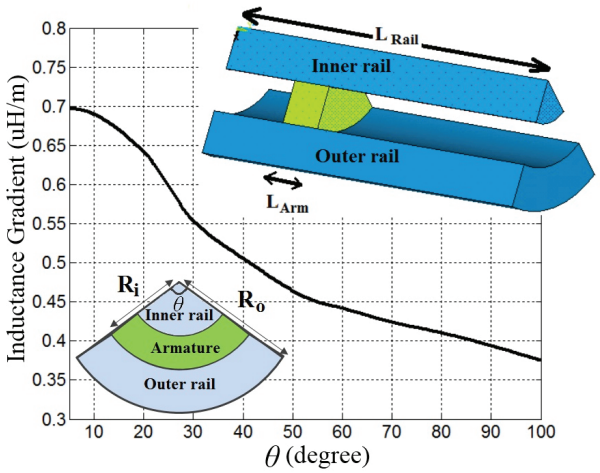

Fig. 1. The geometry and cross-section of the EMSRL and L′ for versus θ with $R_1 = 10$ mm, $R_0 = 30$ mm and $L_{arm} = 10$ mm.

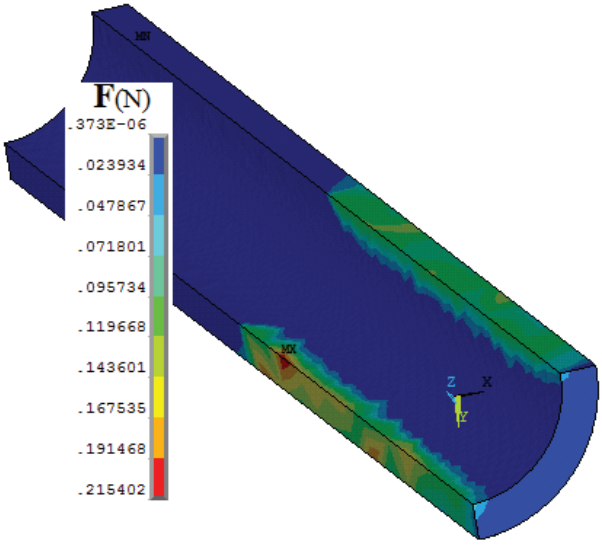

Fig. 2. Force distribution in outer rail for 10 kA input current.

in the same direction on the outer rail, which means a severe decrement in the magnetic field intensity in the barrel; therefore, a decreasing $L\prime$ versus angle θ is reasonable. It looks like the effects of height increasing in the parallel EMRLs. Here we have somewhat rail overhead which more decreases $L\prime$. The $L\prime$ versus angle θ for a EMSRL with R_i=10 mm, R_o=30 mm, L_R=500 mm and L_{arm}=10 mm is shown in Fig. 1. Looking like a conventional EMRL, force distribution on the rails is repulsive. In the inner rail, the magnetic force is compressive and cannot make a major defect in launch process but the force upon the outer rail is expanding and wants to decrease its curve. Because of this force, the minimum pressure to hold a proper contact between armature and outer rail must be provided by containments.

By decreasing the contact area, the current should flow through less area, which results in higher density distributions and consequently higher temperature spots. The possibility of arc creation during the launch process is increased too. Force distribution on outer rail is shown in Fig. 2.

By using thicker outer rail or a rigid containment, the negative effects of repulsing force upon the outer rail could be neglected. Because of highly concentrated current density in root region of armature, the magnetic force in this region is maximum and its distribution is very similar to its current distribution. As most of the force is applied on the armature rear, there is no need to have a long armature.

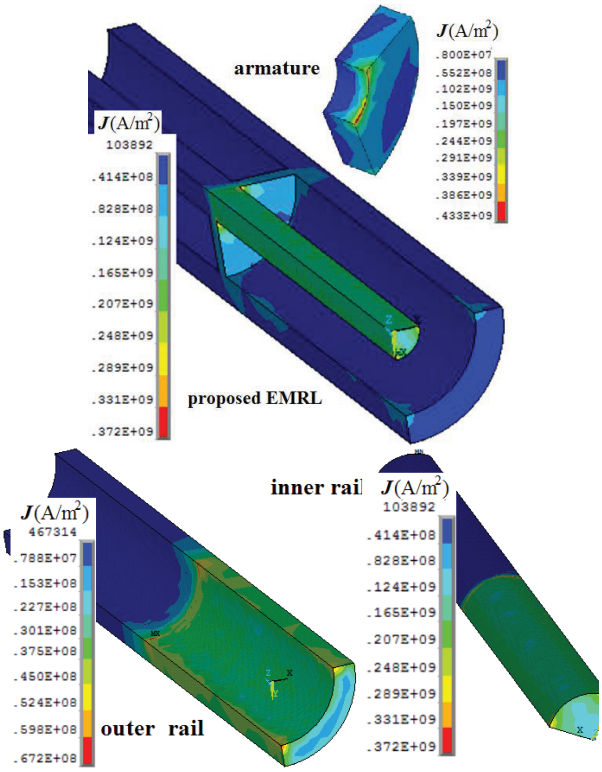

Fig. 3. The current density distribution on the EMRL for a single slice-projectile with $L_R = 500$ mm, $R_t = 10$ mm, $R_0 = 30$ mm, $L_{2\ mm} = 10$ mm and $\theta = 90^\circ$ and input current is 10kA.

B. Current density distribution

As with a parallel electromagnetic launcher, current density in an EMSRL is very highly concentrated at the inside edge and corners of the rails, especially in the inner rail, and because of its lesser cross-section, it is very limiting (see Fig. 3). The problem of high current density spots still exists, and not only there is not a

considerable improvement over conventional rectangular rail EMLs, it would be worse in the inner rail especially for higher R_o/R_i ratios. The root region of the armature has the highest current density distribution similar to a conventional EML, and the concentration of current in this region would be higher if the R_o/R_i ratio were increased because of radial distribution of current in the armature. Thus, the joule heating process can be destructive in this region, especially in the area close to the inner rail.

IV. MULTI-PROJECTILE EMSRL

In an EML system there are several desired goals such as high muzzle velocity, uniform current distribution and low corrosion rate. In some applications having a high frequency of launching is more desirable in which lower muzzle velocities can be neglected. It is possible to make a multi-projectile structure by using an EMSRL. If we arrange several slice-rail structures beside one another as their inner rails make slices of a cylinder, a multi-projectile EMSRL can be made. All the inner rails can be replaced with a complete cylinder to lessen problems with the current density distribution on the inner rails and to obviate the requirement of containment. The geometry of a dual-projectile and a quad-projectile EMSRL are shown in Fig. 4, where R_i, R_o, L_R, L_{arm} and θ are, respectively, inner rail radii, outer rail radii, rail length, armature length and the total angle of curved rails, as in a single EMSRL structure.

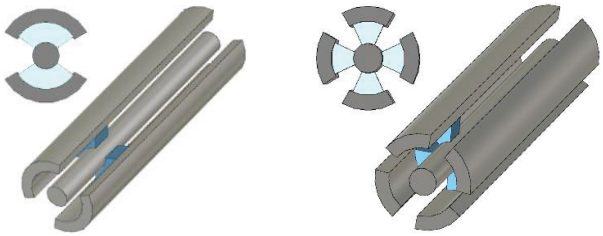

(a) (b)

Fig. 4. 3D view and cross-section of the EMSRL: (a) dual-projectile and (b) quad-projectile.

A. Current density distribution

The current density distribution on the structure of three dual-projectiles for θ =45°, 90° and 135° is shown in Fig. 5. The rail material is considered to be copper. The current density distribution for larger θ is more uniform and its maximum value in each rail has decreased subsequently. Looking like a conventional electromagnetic launcher, the high current density spots are located at edges and corners. Also, the current density distribution on the quad-projectile EMSRLs for θ =20°, 45° and 65° is shown in Fig. 6. In order to

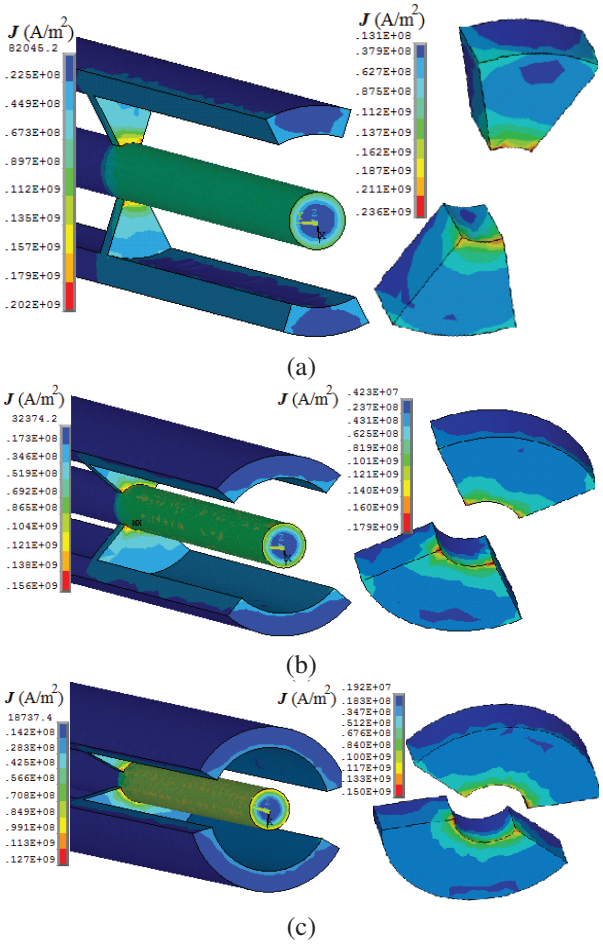

Fig. 5. The current density distribution on dual-projectile EMSRL, R_f = 10 mm, R_0 = 30 mm, $L_{2\ mm}$ = 10 mm, L_R = 500 mm and input current is 10kA. (a) θ = 45°, (b) θ = 90°, and (c) θ = 135°.

investigate the effect of a higher order of projectiles on current density, its maximum values in armatures were compared and it was seen that there is a decrement in its maximum for higher order projectiles, especially in larger θ. The current density distributions on armatures of quad-projectile EMSRL with R_i=10 mm, R_o=30 mm, L_{arm}=10 mm, L_R=500 mm and θ_{total}=180° are shown in Fig. 6. The maximum value of current density for a quad-projectile EMSRL with θ=45° will be 9% lower than a dual-projectile with θ=90°.

B. Inductance gradient

As expected, the net force on the inner rail is negligible because of symmetry especially for higher order projectiles. The net force on the outer rail is repulsive and cylindrical containment can easily hold them. Making a multi-projectile using equal slice-rail structure is a much easier method in comparison with other plane methods. Here, repulsing forces between rails are not limited as

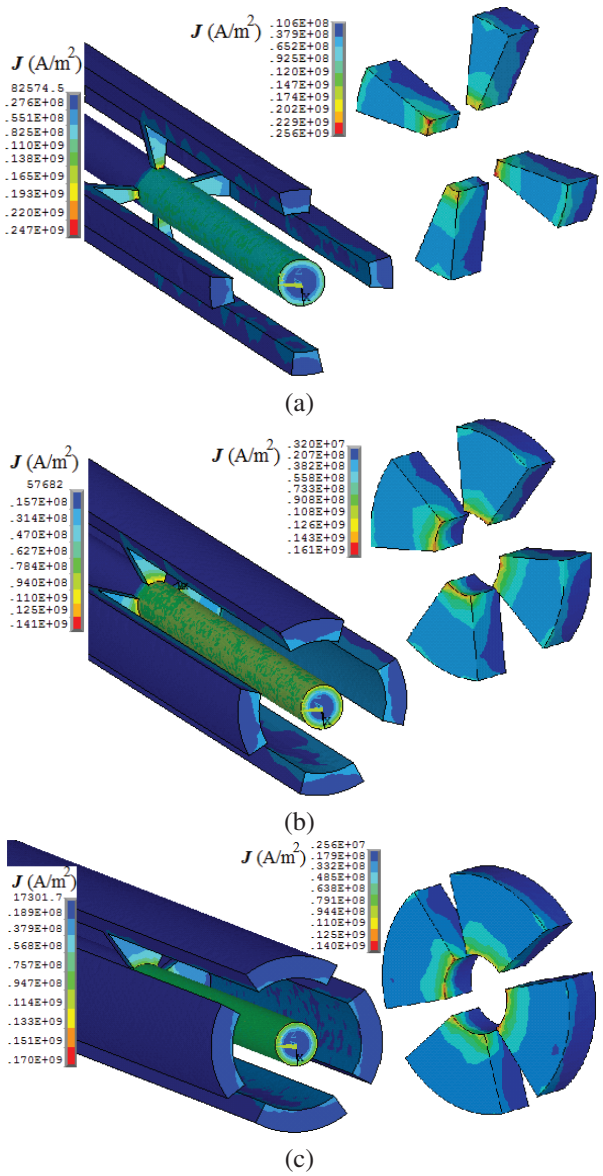

Fig. 6. The current density distribution on quad-projectile EMSRL, R = 10 mm, R_0 = 30 mm, $L_{2\ mm}$ = 10 mm, L_R = 500 mm and input current is 10kA. (a) $\theta = 20°$, (b) $\theta = 45°$, and (c) $\theta = 65°$.

in others. In plane methods, holding rails needs more consideration, especially the rails which must be inside the structure, and design of a multi-projectile electromagnetic launcher with more armatures is not as easy as here. To make an N-projectile EMSRL, N slice-rail structure with θ=360°/N should be held alongside each other in a concentric ring position. It would appear that we must use N slice-rail structures with less θ in order to apply containment packing. By knowing the applied force on each armature in moving direction, self and mutual inductance gradients in an N-projectile launcher can be calculated using the following equations:

$$F_1 = \frac{1}{2}L'_{11}I_1^2 + M'_{12}I_1 l_2 + M'_{13}I_1 I_3 + \ldots + M'_{1n}I_1 I_n,$$
$$F_2 = \frac{1}{2}L'_{22}I_2^2 + M'_{21}I_2 I_1 + M'_{23}I_2 I_3 + \ldots + M'_{2n}I_2 I_n,$$
$$\vdots$$
$$F_n = \frac{1}{2}L'_{nn}I_n^2 + M'_{n1}I_n I_1 + M'_{n2}I_n I_2 + \cdots + M'_{n,n-1}I_n I_{n-1}, \quad (5)$$

where $F_1, F_2, \ldots, F_n$ are the electromagnetic propulsive forces acting on the armatures in moving direction and $I_1, I_2, \ldots, I_n$ are the excitation current flowing through each rail respectively. In this symmetric design, the rails currents are equal and $I_1 = I_2 = \ldots = I_n$=I and M_{ij}=M_{ji} for i, j=1, 2, …, n.

In order to study the effects of neighboring launchers on each other, the values of $M\prime$ and $L\prime_{eff}$ have been determined using 2D-FEM simulations for these three launchers (see Fig. 7): a dual-projectile, a triple-projectile and a quad-projectile, all with R_i=4 mm, R_o=35 mm. The mutual inductance gradient is a negative value in all cases, which means a decrement in effective inductance gradient in a single shot. By increasing the number of projectiles, the decrement value in $L\prime_{eff}$ would be larger. It is usual to define the effective inductance gradient for each armature, after which a total inductance gradient for the launcher can be defined as the sum of the effective inductance gradients, $L'_{\text{total}} = \sum_n L'_{\text{eff}}$.

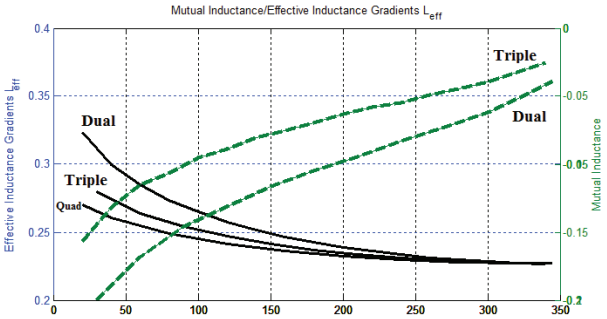

Fig. 7. L'sc and M as function of θ for dual-projectile, tripleprojectile and quad-projectile with R_i = 4 mm, R_a = 35 mm.

As we saw in Fig. 1, the inductance gradient of an EMSRL decreases as its angle increases, and a similar behavior in multi-projectile EMSRLs is reasonably expected. By increasing the number of projectiles in this symmetric method, $L\prime$ reduction is reasonable. Thus, $L\prime$ of a quad-projectile is smaller than the $L\prime$ of a dual-projectile, and both of them are smaller than the $L\prime$ of single-projectile EMSRL when all of them have the same

angle of θ. The $L\prime$ versus θ for single slice-projectile, dual-projectile and quad-projectile EMSRLs is shown in Fig. 8. The reduction in $L\prime$ values become smaller when the total angle of the structure is increased.

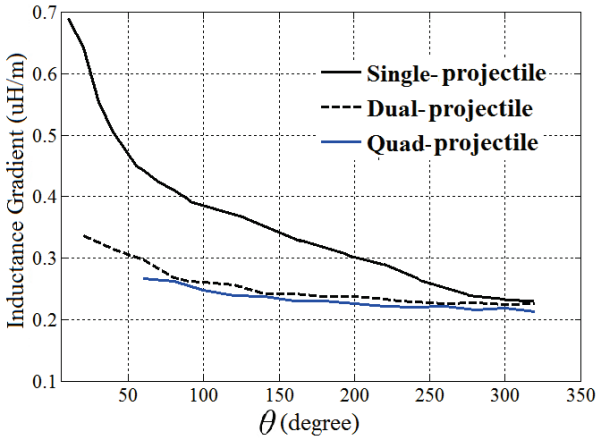

Fig. 8. L' as a function of θ for Single slice-projectile, dual-projectile and quad-projectile with R_i = 10 mm, R_0 = 30 mm, $L_{a\ \mathrm{mm}}$ = 10 mm, L_R = 500 mm.

A structure with minimal hot-spots and tolerable $L\prime$ is very desirable especially in applications where substitution of components is expensive or even impossible. As previously discussed, an EMSRL can be expanded to a multi-projectile EML by using more pairs, when the number of slices increases or when its angle increases, even though $L\prime$ would be decreased. Decreasing of the $L\prime$ is not interesting but current density distribution in rails would be more uniform and the maximum value should be decreased. Thus, a complete structure which is a cylindrical EMRL would be a good candidate to have a tolerable $L\prime$ and a more uniform current density distribution in its rails. In the case of θ=360°, which is a complete cylindrical structure, the current density distribution is ideally uniform at the surface of each rail at the very least. In next section a cylindrical EMRL will be considered.

V. CYLINDRICAL ELECTROMAGNETIC RAIL LAUNCHER

A cylindrical EMRL is a structure with two concentric cylindrical conductors in which the ring armature. a ring armature closes the path of current between two cylinders. Because of symmetry, there is no consideration about imposed forces upon rails. The force upon rails is radial and the net value is insignificant. In terms of force distribution on rails, current density distributions and consequent thermal effects, the cylindrical EMRL is the best among slice-rail structures because of its symmetry, the reduced risk of hot spots and because no containment is required, unlike parallel electromagnetic launchers. The geometry of a cylindrical-rail EMRL is shown in Fig. 9, where R_i and R_o are inner rail radii and outer rail radii, respectively.

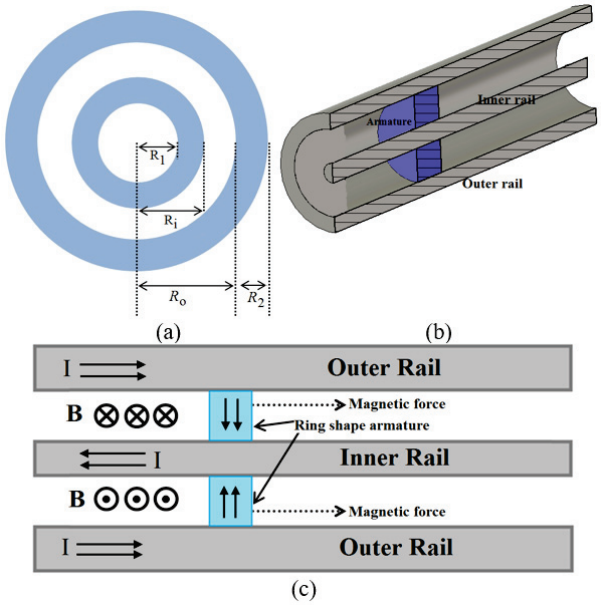

Fig. 9. Cylindrical EMRL. (a) cross section of the EMRL, (b) half-view of the 3D model, and (c) diagram of the current, magnetic flux density and force.

A. Current density and force distributions

A symmetrical structure such as a cylindrical electromagnetic launcher is expected to have more uniform current distribution on the rails. Figure 10 shows the current density distribution on the armature and both inner and outer rails for a cylindrical EMRL, with R_i=10 mm, R_o=30 mm, L_{arm}=10 mm and L_R=500 mm. Because there is no high current spot on the inner rail, the possibility of hot spot creation and corrosion is decreased. Current density distribution in the outer rail is not as high as in the inner rail, although its distribution is uniform. To determine the effect of rail width on current density distribution in rails, we considered the maximum value of current density in each rail. The reduction of the maximum value of current density in a thicker rail is insignificant. Because of symmetry, net forces on rails do not create a big quantity of the force. To avoid deformation from tensions and possible fluctuation, it is better to have rails with a minimum thickness of 10 mm. Particular consideration should be given to the armature because of its highly non-uniform current distribution; consequently, temperature and forces distributions will be non-uniform.

The distribution of Joule heat and force on the armature of an EMRL, with R_i=10 mm, R_o=30 mm,

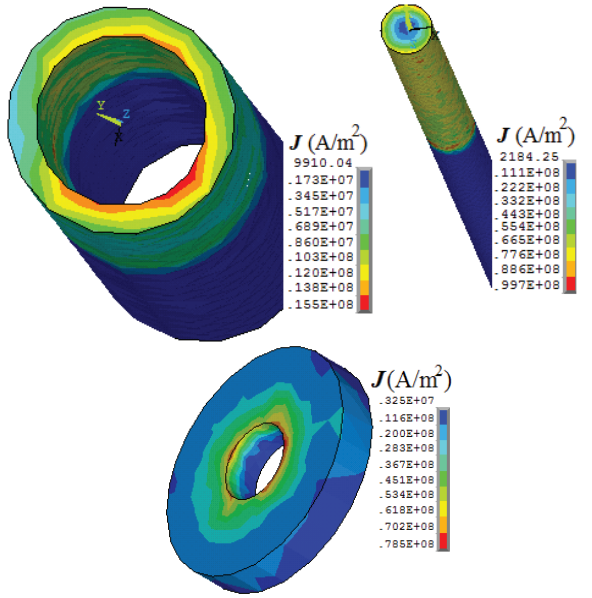

Fig. 10. Cylindrical EMRL. Current density distribution on rails when input current is 10 kA.

L_{arm}=10mm, and L_R=500 mm, is shown in Fig. 11. Due to a high concentration of current density in the inner part of the armature, the risk of melting is increased and at the same time, because of bigger applied Lorentz forces in this region, the possibility of deformation is increased too.

B. Inductance gradient and velocity

It is obvious that a cylindrical EMRL is a slice-rail one with θ=360° or any complete version of any multi-projectile EMSRL. Figure 8 shows that the inductance gradient decreases when the angle increases, so its minimum value will be obtained for a cylindrical state. The effect of cross-sectional parameters was studied in a prior work, so here only the effects of armature length and position on $L\prime$ will be discussed.

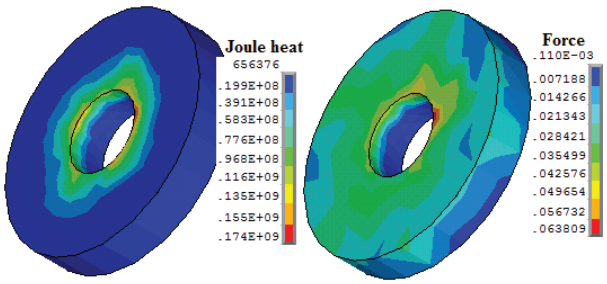

Fig. 11. The distribution of the: (a) Joule heat and (b) Lorenz force in the armature in a cylindrical EMRL with $R_1 = 10$ mm, $R_0 = 30$ mm, $L_{2\ mm} = 10$ mm, $L_R = 500$ mm and input current is 10kA.

As expected from conventional EMRLs, armature width has no significant effects on the inductance gradient of the structure and even current density distribution. For very thin armatures, thermal considerations must be considered and defect plausibility is increased. With thicker armatures, not only are there no advantages but the total mass of the launch package is increased, resulting in lower muzzle velocity.

Thus, the only consideration is that the armature width should be thick enough, at least 4 or 5 mm. The effect of armature width on $L\prime$ is shown in Fig. 12. To determine the inductance gradient of a structure across the rail, the total rail length should be divided into several small parts, then for a specified input current the propelling force on armature can be calculated, after which $L\prime$ will be determined.

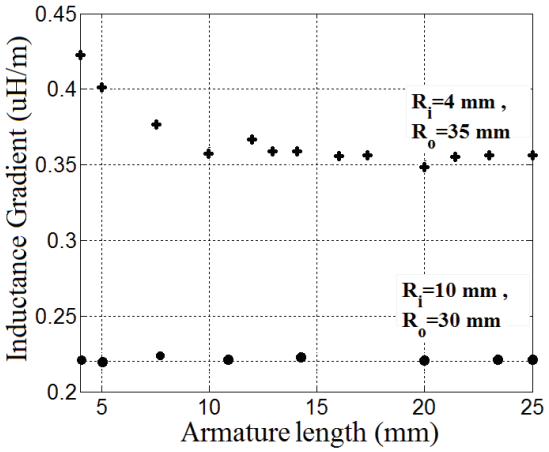

Fig. 12. Cylindrical EMRL: the inductance gradient versus armature length.

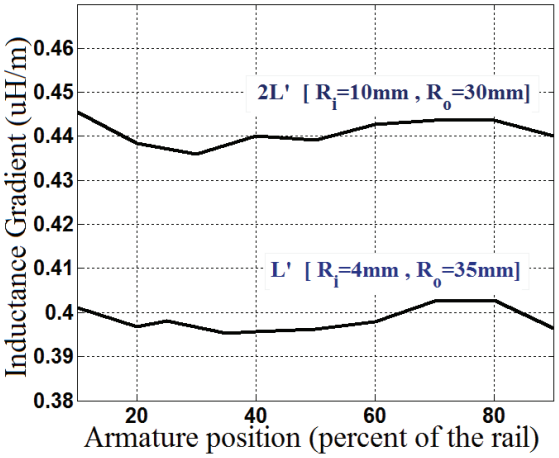

Fig. 13. Cylindrical EMRL: the inductance gradient versus armature position.

For each point on rail, that process should be done so a new design and a new meshing for each step. The inductance gradient versus rail length is shown in Fig. 13. Because two different rail lengths were considered, we have shown both of them versus percentage of rail length. In regions far from breech or muzzle, there is a slight increment in L′ value toward the muzzle. A similar behavior was observed for conventional electromagnetic launchers.

Finally, muzzle velocity has been computed by motion equations. The position and velocity of the armature are updated throughout the analysis shown in Chart 1. Figure 14 shows the current profile and velocity history of the muzzle for R_i= 4 mm, R_o=35 mm, R_i= 10 mm, and R_o=30 mm.

Chart 1: Calculation of the velocity

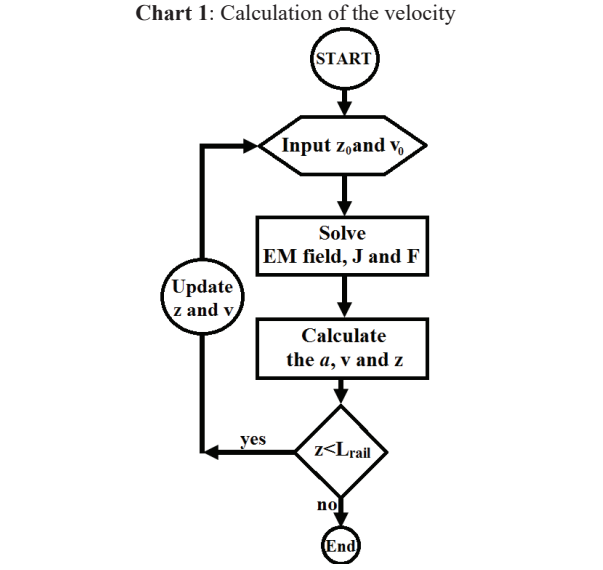

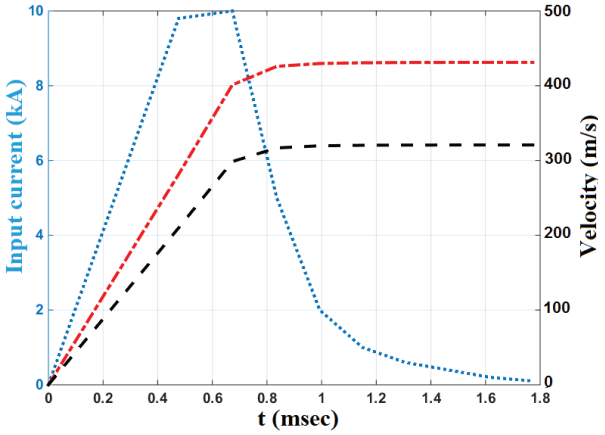

Fig. 14. Cylindrical EMRL: current profile (blue dot line) and velocity history for Ri = 4 mm and Ro^2 = 35 mm (red dot dash line) and Ri = 10 mm and Ro = 30 mm (black dash line).

VI. CONCLUSION

In this paper the slice-rail structure as an unequal-rail parallel electromagnetic launcher and cylindrical EMRL has been studied. The possibility of building a multi-projectile EMSRL using pairs of slice-rail structures was shown. This is a much easier method for making a multi-projectile in comparison with other plane methods, especially because here repulsing forces between rails are not limited as with others methods. The inductance gradient of an EMSRL structure will be decreased if its angle is increased. This is also valid for the maximum value of current density in both rails. Similar behavior is observed in a multi-projectile electromagnetic launcher. *L′* of a quad-projectile is smaller than the *L′* of a dual-projectile, and both of them are smaller than the *L′* of a single-projectile EMSRL for a certain angle. Rail width has no significant effects on the inductance gradient of the structure and even on the maximum value of current densities. Additionally, armature width has no significant effects on the inductance gradient of the structure and even current density distribution. In regions far from breech or muzzle, there is a slight increment in *L′* value toward the muzzle.

REFERENCES

[1] S. R. N. Praneeth, B. Singh, and J. P. Khatait, "Study on effect of rail filet radius in electromagnetic railgun," *IEEE Transactions on Plasma Science*, vol. 49, no. 9, doi: 10.1109/TPS.2021.3102054, 2021.

[2] I. R. McNab, "Progress on hypervelocity railgun research for launch to space," *IEEE Transactions on Magnetics*, vol. 45, no. 1, pp. 381-388, Jan. 2009.

[3] B. V. Jayawant, J. D. Edwards, L. S. Wickramaratne, W. R. C. Dawson, and T. C. Yang, "Electromagnetic launch assistance for space vehicles," *IET Science, Measurement & Technology*, vol. 2, no. 1, pp. 42-52, Jan. 2008.

[4] A. Rabiei, A. Keshtkar, and L. Gharib, "Study of current pulse form for optimization of railguns forces," *IEEE Transactions on Plasma Science,* vol. 46, no. 4, pp. 1047-1053, doi: 10.1109/TPS.2018.2805329, Apr. 2018.

[5] J. F. Kerrisk, "Current distribution and inductance calculation for railgun conductors," *Los Alamos National Laboratory Report LA-9092-MS*, pp. 1-18, Nov. 1981.

[6] J. H. Chang, E. B. Becker, and M. D. Driga, "Numerical simulation for induction coil launcher using FE-BE method with hybrid potentials," *IEEE Proceedings A - Science, Measurement and Technology*, vol. 140, no. 6, pp. 501-508, Nov. 1993.

[7] V. Thiagarajan, "Computation and scaling of inductance gradients in electromagnetic launch systems," *IET Science, Measurement & Technology*, vol. 2, no. 5, pp. 337-348, Sep. 2008.

[8] N. Sengil, "Implementation of Monte Carlo Method on electromagnetic launcher simulator," *IEEE Transactions on Plasma Science*, vol. 45, no. 5, pp. 1156-1160, May 2013.

[9] V. Thiagarajan and K. Hsieh, "Investigation of a 3-D hybrid finite-element/boundary-element method for electromagnetic launch applications and validation using semi-analytical solutions," *IEEE Transactions on Magnetics*, vol. 41, no. 1, pp. 398-403, Jan. 2005.

[10] G. Wang, L. Xie, Y. He, S. Song, and J. Gao, "Moving mesh FE/BE hybrid simulation of electromagnetic field evolution for railgun," *IEEE Transactions on Plasma Science*, vol. 44, no. 8, pp. 1424-1428, Aug. 2016.

[11] A. Musolino, "Finite-element method/method of moments formulation for the analysis of current distribution in rail launchers," *IEEE Transactions on Magnetics*, vol. 41, no. 1, pp. 387-392, Jan. 2005.

[12] B. Kim and K. Hsieh, "Effect of rail/armature geometry on current density distribution and inductance gradient," *IEEE Transactions on Magnetics,* vol. 35, no.1, pp. 413-416, Jan. 1999.

[13] A. Keshtkar, "Effect of rail dimension on current distribution and inductance gradient," *IEEE Transactions on Magnetics*, vol. 41, no. 1, pp. 383-386, Jan. 2005.

[14] M. S. Bayati and A. Keshtkar, "Study of the current distribution, magnetic field, and inductance gradient of rectangular and circular railguns," *IEEE Transactions on Plasma Science*, vol. 45, no. 5, pp. 1376-1381, May 2013.

[15] A. Keshtkar, S. Bayati, and A. Keshtkar, "Derivation of a formula for inductance gradient using IEM," *IEEE Transactions on Magnetics*, vol. 45, no. 1, pp. 305-308, Jan. 2009.

[16] M. A. Huerta and J. C. Nearing, "Conformal mapping calculation of railgun skin inductance," *IEEE Transaction on Magnetics*, vol. 27, no. 1, pp. 112-115, Jan. 1991.

[17] M. S. Bayati and K. Amiri, "Study of various C-shaped armatures in electromagnetic launcher," *Applied Computational Electromagnetics Society (ACES) Journal*, vol. 30, no. 9, pp. 1029-1034, Sep. 2015.

[18] R. A. Marshall, "Railgun bore geometry round or square?", *IEEE Transactions on Magnetics,* vol. 35, no. 1, pp. 427-431, Jan. 1999.

[19] Y. He, Y. Guan, and S. Song, "Design of a multi-turn railgun for accelerating massive load to high speed," *IEEE Transactions on Plasma Science*, vol. 47, no. 8, pp. 4181-4183, Aug. 2019.

[20] Y. Xing, B. Lei, Q. Lv, H. Xiang, J. Chen, and R. Zhu, "Simulations, experiments, and launch characteristics of a multiturn series–parallel rail launcher," *IEEE Transactions on Plasma Science*, vol. 47, no. 1, pp. 603-610, Jan. 2019.

[21] Y. Geng, J. Yuan, and J. Li, "Main cause of groove formation on rails might be local electro-explosion phenomenon," *IEEE Transactions on Plasma Science*, vol. 45, no. 7, pp. 1629-1634, May 2017.

[22] Y. A. Kareev, V. P. Bazilevski, Y. G. Gendel, I. S. Glushkov, and A. T. Kuharenko, "A cylindrical railgun as a prototype of a new generation railgun," *IEEE Transactions on Magnetics*, vol. 37, no. 1, pp. 421-424, Jan. 2001.

[23] T. G. Engel and M. A. Prelas, "Asteroid mining and deflection using electromagnetic launchers," *IEEE Transactions on Plasma Science*, vol. 45, no. 7, pp. 1327-1332, May 2017.

[24] M. S. Bayati and A. Keshtkar, "Novel study of the rails geometry in the electromagnetic launcher," *IEEE Transactions on Plasma Science*, vol. 43, no. 5, pp. 1652-1656, May 2015.

[25] X. Xue, T. Shu, Z. Yang, and G. Feng, "A new electromagnetic launcher by sextupole rails: Electromagnetic propulsion and shielding numerical validation," *IEEE Transactions on Plasma Science*, vol. 45, no. 9, pp. 2541-2545, Sep. 2017.

[26] Z. Yang, G. Feng, X. Xue, and T. Shu, "An electromagnetic rail launcher by quadrupole magnetic field for heavy intelligent projectiles," *IEEE Transactions on Plasma Science*, vol. 45, no. 7, pp. 1095-1100, July 2017.

[27] J. C. Schaaf and N. F. Audeh, "Electromagnetic coaxial railgun," *IEEE Transactions on Magnetics*, vol. 25, pp. 3263-3265, Sep. 1989.

[28] J. C. Schaaf and N. F. Audeh, "Solid armature coaxial railgun experiment results," *IEEE Transactions on Magnetics*, vol. 29, no. 1, pp. 711-715, Jan. 1993.

[29] S. Mozafari and M. S. Bayati, "Design and simulation of a slice-rail with multi-projectile and coaxial railguns using 2D-FEM," *Tabriz Journal of Electrical Engineering* (*TJEE*), vol. 51, no. 1, pp. 121-127, 2021.

Shahab Mozafari was born in Ravansar, Kermanshah, Iran, in 1985. He received the B.Sc. degree in Electronic Engineering from Shahid Rajaei Teacher Training University, Tehran, Iran, in 2006, the M.Sc. degree in Telecommunication fields and Waves Engineering from the University of Tabriz, Tabriz, Iran, in 2008, and the Ph.D. degree in Electrical Engineering from Razi University in 2023. His research interests include programing, antenna, and neural networks.

Mohammad S. Bayati was born in Sonqor, Iran, in 1979. He received the B.Sc. degree in Electrical Engineering from the University of Tabriz, Tabriz, Iran, in 2002, the M.Sc. degree in Telecommunication fields and Waves Engineering from the Sahand University of Technology, Sahand, Iran, and the Ph.D. degree in Electrical Engineering from the University of Tabriz in 2011. He is an Assistant Professor with the Department of Electrical Engineering, Razi University, Kermanshah, Iran. His current research interests include antenna, electromagnetic launchers, and wireless power transfer.